

# GLOBULAR CLUSTER SYSTEMS IN GIANT ELLIPTICALS: THE MASS/METALLICITY RELATION\*

WILLIAM E. HARRIS

Department of Physics & Astronomy, McMaster University, Hamilton ON L8S 4M1

*Draft version November 6, 2018*

## ABSTRACT

Data from the Hubble Space Telescope taken with the ACS/WFC camera have been used to investigate the globular cluster (GC) populations around six giant elliptical galaxies that are  $\sim 40$  Mpc distant. From these six fields, imaged in  $B$  and  $I$ , a total of more than 15000 candidate GCs have been measured, of which 8000 or more are high-probability globular clusters. The data reach a limiting magnitude near  $M_I \simeq -8$ , about 0.4 mag fainter than the GC luminosity function turnover point, and thus thoroughly cover the bright half of the GC population. Most of the individual GCs on these images are marginally resolved nonstellar objects, so King-model profiles convolved with the stellar point-spread functions are used to measure their individual total magnitudes, colors, and linear effective radii. The classic bimodal form of the GC color-magnitude distribution shows up unambiguously in all the galaxies, allowing an accurate definition of the mean colors along each of the two sequences as a function of magnitude (the *mass/metallicity relation* or MMR). The blue, metal-poor cluster sequence shows a clearly defined but nonlinear MMR: in this particular photometric dataset the mean GC color changes smoothly from a near-vertical sequence at low luminosity ( $M_I \gtrsim -9.5$ ) to an increasingly redward slope at higher luminosity. By contrast, the red, metal-rich sequence shows little trace of a MMR and is nearly vertical at all luminosities. The form and slope of the MMR along either sequence do not depend strongly on either cluster size  $r_h$  or galactocentric distance  $R_{gc}$ .

All the observed features of the present data agree with the interpretation that the MMR is created primarily by GC *self-enrichment*, along the lines of the quantitative model of Bailin & Harris (2009). During the protocluster formation stage, the more massive GCs are better able to hold back the enriched products of the earliest supernovae and to seed the lower-mass stars still in formation. The “threshold” mass at which this effect should become noticeable is near 1 million Solar masses, which is closely consistent with the transition region that is seen in the data. More generally, the data favor models in which the star formation efficiency in a protocluster is roughly independent of mass, and in which the gas retention efficiency is a strong function of mass.

Correlation of the median scale sizes  $r_h$  of the GCs with other parameters shows that the metal-poor clusters are consistently 17% larger than those of the metal-rich clusters, and that this difference holds at all galactocentric distances and luminosities. At the same time, cluster size scales with halo location as  $r_h \sim R_{gc}^{0.11}$ , indicating that *both* metallicity and the external tidal environment play roles in determining the scale size of a given cluster. Lastly, both the red and blue GC components show *metallicity gradients* with galactocentric distance that are shallow but real: heavy-element abundance scales as  $Z \sim R_{gc}^{-0.1}$  for both types.

*Subject headings:* galaxies: elliptical and lenticular, cD — galaxies: star clusters — globular clusters: general

## 1. INTRODUCTION

Much of the recent observational work on the populations of globular clusters (GCs) in other galaxies has concentrated on their metallicity distribution function (MDF). A near-universal result, confirmed from both photometric and spectroscopic samples of GCs in many galaxies of all types, is that the MDF is bimodal, strongly suggestive of two major epochs of cluster formation (see, e.g. Zepf & Ashman 1993; Larsen et al. 2001; Harris et al. 2006; Peng et al. 2006; Kundu & Zepf 2007; Strader et al. 2007; Wehner et al. 2008; Peng et al. 2008; Waters et al. 2009, for an extensive range of results and

discussions). This bimodality paradigm has steadily been reinforced as the quality and size of the databases have increased.

A more recent discovery is the existence of intriguing second-order structure in the MDF. In some large galaxies a correlation between color and luminosity has been found along the bluer, more metal-poor GC sequence (Harris et al. 2006; Strader et al. 2006; Mieske et al. 2006). Since the integrated color of old star clusters depends predominantly on their metallicity, this correlation represents a *mass/metallicity relation* or MMR (the trend is also referred to colloquially as a blue tilt, but “MMR” is more accurate and more general). The essence of the trend is that the more massive blue GCs are progressively more heavy-element enriched. Just as intriguingly, the redder and more metal-rich GC sequence has not shown any definite evidence for a MMR even in galaxies where the blue-sequence MMR is strongly present.

\*BASED ON OBSERVATIONS WITH THE NASA/ESA HUBBLE SPACE TELESCOPE, OBTAINED AT THE SPACE TELESCOPE SCIENCE INSTITUTE, WHICH IS OPERATED BY THE ASSOCIATION OF UNIVERSITIES FOR RESEARCH IN ASTRONOMY, INC., UNDER NASA CONTRACT NAS 5-26555. Electronic address: harris@physics.mcmaster.ca

Early hints of this effect were, in fact, clearly noticed by Ostrov et al. (1998) and Dirsch et al. (2003) from wide-field photometric surveys of the GC system in the Fornax cD NGC 1399. There, they pointed out that the highest-luminosity GCs showed a broad unimodal color distribution, as if the blue and red components had merged together at the top end.

To make the effect more challenging to understand, some large galaxies such as NGC 4472 may not show the blue-sequence MMR (Strader et al. 2006; Mieske et al. 2006) even though the measured sample of GCs seems large enough to reveal it, if present. M87, at first claimed to have a MMR (Strader et al. 2006), does not show it according to a larger set of data analyzed by Waters et al. (2009). As will be discussed more extensively below, a critical factor in deciding the presence of an MMR is not just the total measured population of GCs, but also the highest luminosity (mass) to which the sample reaches. These factors are also crucial in deciding whether or not the MMR might be *linear* in color versus magnitude (as is assumed in most previous papers), or *nonlinear*, which in turn is a central issue for the model interpretations that are now starting to appear.

Early descriptive interpretations for the physical cause of the MMR have been suggested in the discovery papers (Harris et al. 2006; Strader et al. 2006; Mieske et al. 2006), but the most promising direction at present for producing the effect is organized around the idea of GC self-enrichment (Strader & Smith 2008; Bailin & Harris 2009). The basic approach is that clusters forming within massive protocluster gas clouds can hold on to some portion of their SNe ejecta during the first round of star formation and thus enrich the still-forming lower-mass stars in the cluster. The higher the proto-GC mass, the higher the gas retention, thus leading to a MMR. The quantitative model of Bailin & Harris (2009) shows that the amount of self-enrichment should be negligible for protoclusters with  $M \lesssim 10^6 M_\odot$ , which are small enough that SN ejecta easily escape their potential well. Thus for clusters smaller than this threshold, the cluster metallicity should be uncorrelated with mass; that is, *the GC sequences should be vertical below this transition-mass point.*

In addition, the Bailin/Harris model predicts that a *red-sequence* MMR should exist, though this should become noticeable only at still higher GC mass and with a smaller amplitude because the effects of internal self-enrichment will be a smaller fraction of the initial (pre-enriched) cluster metallicity at any mass. There is even a hint that this red-sequence MMR has already been observed in the extremely populous cluster systems in NGC 3311 and NGC 4874 (Wehner et al. 2008; Harris et al. 2009; Bailin & Harris 2009).

At the same time as the interpretive models have advanced, the state of the observations is still somewhat confused. The initial claim of Harris et al. (2006) was that, at masses less than  $\sim 10^6 M_\odot$ , the blue sequence is vertical (i.e., color is uncorrelated with luminosity) and that only the higher-mass range showed the correlation. Other papers discuss the MMR in terms of a linear relation between color and metallicity extending continuously downward (Strader et al. 2006; Spitler et al. 2006; Cantiello et al. 2007; DeGraaff et al. 2007; Wehner et al.

2008; Spitler et al. 2008; Cockcroft et al. 2009).

Another, and extremely important, source of confusion is understanding why various individual galaxies do not show an obvious MMR; for example, comments have been raised that the Milky Way does not have the effect. However, the Milky Way does not have enough clusters to reveal a MMR with any statistical confidence *whether or not* it is present. The effect of small-number statistics is especially important if the MMR affects only the higher-mass GCs, which are the rarest.

With the benefit of hindsight, it is easy to understand why these correlations were not noticed earlier: the MMR slope is relatively modest, so big statistical samples of clusters *and* precise, metallicity-sensitive photometry are both needed to see it. Few such samples existed till quite recent years. One way to put this into perspective is to note that the basic phenomenon of bimodality is a *first-order* feature of the GC metallicity distribution that becomes obvious even with samples as small as  $\sim 10^2$  clusters (the prime example is the Milky Way itself, which was the first galaxy in which the bimodality paradigm became clear (Zinn 1985)). By contrast, the MMR is a *second-order* feature and thus in rough terms can be expected to require samples of  $\sim 10^3$  clusters to become clearly detectable.

In giant ellipticals it is possible to measure hundreds of GCs well above the million-Solar-mass level where the MMR is agreed to be most visible; for example, the GC sample to be described in this paper (see below) has 750 clusters brighter than  $M_I = -10.5$ , whereas in the Milky Way there is only one such cluster,  $\omega$  Centauri. The same comparison is true of dwarf galaxies and most disk galaxies, where any attempts to search for the MMR are severely hampered by small-number statistics even with high-quality photometry or spectroscopy. In other words, *for most galaxies on an individual basis, the existence of a MMR is not decidable.* Mieske et al. (2006), in their study of GCs in 76 Virgo galaxies, worked around this issue by combining their galaxies into four luminosity groups (dwarfs through supergiants) to gain increased statistical weight. Even so, the dwarf sample contains too few GCs in the critical high-luminosity regime to clearly reveal a color/luminosity slope there.

A challenge to the existence of the effect itself has been presented by Kundu (2008). His claim is that the MMR is spurious, an artifact of the combination of aperture photometry, low signal-to-noise, and a mass/radius relation for GCs. These concerns will be dealt with in this paper in the sections below. It is, however, already worth emphasizing that the three discovery papers (Harris et al. 2006; Strader et al. 2006; Mieske et al. 2006) employed three different photometric measurement procedures over a wide variety of galaxies, yielding similar MMR slopes. In addition, *ground-based* photometric studies of the GCSs in distant galaxies, in which the individual GCs are completely unresolved and any differential-size issues become moot, also show the MMR (Dirsch et al. 2003; Wehner et al. 2008). Nevertheless, given particularly the growing state of the theoretical modelling, the data need to be put onto a better foundation.

The largest GCS populations of all, and in principle the best for a clear measurement of the MMR, are found in giant and supergiant ellipticals, many of which are cD's

or Brightest Cluster Galaxies (BCGs) at the centers of rich clusters (Harris 2001; Harris et al. 1995; Blakeslee 1999; Harris et al. 2006). In this paper, I present new and homogeneous photometry for six gE's with globular cluster systems that are among the largest known.

Throughout this paper, a distance scale  $H_0 = 70 \text{ km s}^{-1} \text{ Mpc}^{-1}$  is used to convert redshifts and angular diameters to true distances and linear radii.

The plan for this rather long paper is as follows: Section 2 introduces the set of galaxies being studied and the goals for the measurement, while Section 3 steps through the complete process of measurement of the cluster magnitudes, colors, and linear sizes, and Section 4 presents an overview of the final color-magnitude data. Section 5 describes the complete analysis of the GC effective radii (scale sizes) and traces their correlations with external parameters such as metallicity, galactocentric distance, and metallicity. Section 6 presents the full results for the mass/metallicity relation along both the blue and red GC sequences, and its implications for the theoretical models. Lastly, Section 7 presents new results for the spatial metallicity gradients in the red and blue GC subsystems. The discussion concludes with a summary of the findings in Section 8, and some concerns in Section 9 that may affect both the basic nature of the observations and its links with theory.

## 2. THE DATA SAMPLE

The raw data are for six galaxies drawn from the giant ellipticals observed in HST program GO 9427 (Harris, PI). These six, listed in Table 1, are all imaged with the ACS/WFC in the two broadband filters  $F435W$  ( $B$ ) and  $F814W$  ( $I$ ), and are the ones in this particular program that turned out to have the largest GC populations. As noted in Table 1, most are at distances  $\sim 40$  Mpc. The data from this program also contained three other giant E targets, NGC 5322, 5557, and 7049: these three had distinctly smaller GC populations, and as will be described below, they were used instead to help define the level of field contamination.<sup>1</sup>

In the original data paper for this program (Harris et al. 2006), both PSF-fitting and fixed-aperture photometry were used to measure the GCs. However, neither approach is strictly correct, because many of the GCs are not quite small enough in linear size to appear starlike on the images, and furthermore their intrinsic sizes are not identical from cluster to cluster. Various tests in the literature (e.g. Larsen 1999; Jordán et al. 2005; Mieske et al. 2006; Harris et al. 2009) demonstrate that when the FWHM of the star cluster is smaller than about 10% of the FWHM of the stellar point-spread function (PSF), its size can no longer be determined from these conventional imaging techniques and it can be treated as starlike. But if it is bigger, its size needs to be individually accounted for to determine a correct total magnitude. For purposes of comparative discussion, we can usefully distinguish four different regimes of resolution:

<sup>1</sup> NGC 7626 was not included in the 2006 paper but is added here since the raw images are completely homogeneous with the other five. The full data analysis for NGC 7626 will be described in Harris et al. (2009, in preparation) along with four other giant ellipticals that have  $B$ -band images from ACS/WFC and  $I$ -band images from archival WFPC2 exposures.

- *Well resolved:* The FWHM or effective diameter of the GC is much larger than the PSF,  $FWHM(GC) \gg FWHM(PSF)$ . This is the case, for example, for HST imaging of clusters in M31 and other Local Group galaxies (e.g. Barmby et al. 2007).
- *Partially resolved:* The GC and stellar profiles have comparable widths,  $FWHM(GC) \sim FWHM(PSF)$ . This is the case for HST imaging of many of the GCs in the Virgo galaxies (Jordán et al. 2005; Mieske et al. 2006) at  $d = 16$  Mpc and for NGC 5128 (Gómez & Woodley 2007; McLaughlin et al. 2008) at  $d = 4$  Mpc, for example.
- *Marginally resolved:* The GC is barely large enough to be measured relative to the PSF,  $FWHM(GC) \sim 0.1 - 0.3 FWHM(PSF)$ . The GCs analyzed in the present paper fall into this category.
- *Unresolved:*  $FWHM(GC) < 0.1 FWHM(PSF)$ , for all practical purposes making it starlike and allowing normal PSF-fitting photometry. GCs in much more distant galaxies such as Coma (Harris et al. 2009), even with HST resolution, fall into this category.

The mean half-light radius of classic GCs is typically about 3 pc, and 90% of them have  $r_h \lesssim 6$  parsecs (Figure 1). Thus at  $d \simeq 40$  Mpc, they will subtend a typical angular diameter  $\simeq 0.03''$ , which equals about 30% of the  $0.1''$  FWHM of stars on the HST ACS camera. This comparison means that we should expect the GCs in these target galaxies to fall in the *marginally resolved* or (for the smallest ones) *unresolved* regime. Although the differential aperture-size corrections to their photometry can be expected to be small, the purpose of the present paper is to determine these corrections and to construct a new database of photometry within which any MMR can be more securely determined.

## 3. PHOTOMETRIC TECHNIQUES

### 3.1. Defining the PSF

Each target galaxy discussed in this paper is surrounded by some thousands of barely-nonstellar globular clusters plus a variety of 'field' contaminants (a relatively few foreground stars plus numerous faint, small background galaxies). As will be seen below, the GC populations clearly outnumber all other types of objects. The first task for the photometry is to derive individual profile-size measurements of each detected object. PSF-convolved model GC profiles must be matched to each individual object and the optimum fit selected. Several codes have been developed and used in the literature to do this, including the ISHAPE code of Larsen (1999) and Larsen et al. (2001) which has been used for young and old star clusters in a wide range of distant galaxies; the KINGPHOT code of Jordán et al. (2005) used principally for the GCs in Virgo galaxies; and the code of McLaughlin et al. (2008) which can fit any one of five standard GC models and has been used for clusters in M31 and NGC 5128.

The fitting code adopted for this work is ISHAPE. This code gives a fast, well tested, effective procedure for fitting *marginally* resolved GCs like these, where we are primarily interested in determining the cluster size  $r_{eff}$  and cannot expect to obtain precise solutions for more subtle structural parameters such as ellipticity, orientation, or core radius. These latter quantities become dramatically easier to measure for star clusters in nearby galaxies, such as for Virgo, NGC 5128, or the Local Group members where the degree of resolution is much higher. ISHAPE and its parent package BAOLAB also contain highly effective tools for testing the results, including profile-subtracted images, and the ability to generate simulated populations of PSF-convolved objects of arbitrary size and ellipticity.

It is possible to construct PSFs for HST images through TinyTim modelling, but difficulties arise for appropriate choices of a diffusion kernel (see, e.g. Spitler et al. 2006; Georgiev et al. 2008, for recent extensive discussions in similar studies). To avoid any such uncertainties in the modelling chain I have employed purely empirical PSFs constructed for each individual frame. Fortunately, the true FWHM of the stellar PSF on the ACS/WFC frames is known beforehand to fall in the range  $0.09'' - 0.10''$  on series of images that have been properly coadded. This *a priori* constraint helps to select out candidate starlike objects.

All exposures for each target field and in each filter were registered and combined through *multidrizze*, as described in more detail in Harris et al. (2006). To build a preliminary catalog of detected objects, the SExtractor code (Bertin & Arnouts 1996) was used with a generously low threshold, and from this, a diagnostic graph of object half-light radius  $r_{1/2}$  versus total magnitude was plotted. An example for the NGC 4696 field is shown in Figure 2. The next stage was an iterative process of identifying genuine starlike, isolated objects across the image from which the PSF could be defined. Objects selected as candidate PSF stars were those within the region marked out in the Figure, falling along the lower envelope of the  $r_{1/2}$  distribution. Moderately bright, unsaturated stars fall within this region, whereas saturated stars fall along the upturn region at the bright end of the distribution. The candidates were then inspected through IRAF/imexamine, their radial profiles and FWHMs measured, and ones with FWHM falling in the range  $1.8 - 2.0$  px (that is,  $0.09'' - 0.10''$ ) were selected. This subsample was put into the IRAF/daophot/psf routine, inspected at finer detail, and any with remaining excess nonstellar wings or faint neighbors rejected. The final numbers of objects used in each field, along with the final FWHM of the adopted point-spread function, are listed in Table 2. In all cases, the stars used to define the final PSF were widely distributed in location, and thus the PSF represents an average across the field (though no differences in the PSF shape or width at the level of  $\pm 0.1$  px as a function of position were found; see Harris et al. 2006 for additional discussion).

Other characteristics of the raw image data including the internal photometric precision and completeness are described in much more detail in Harris et al. (2006). Briefly, the exposures for each galaxy were originally designed to reach an intrinsic limiting magnitude  $M_I \simeq -8$  at 50% detection completeness, so that the turnover

point (peak frequency) of the globular cluster luminosity function (GCLF) at  $M_I \simeq -8.4$  would be reached at almost 100% completeness. The data then thoroughly sample about 4 magnitudes of the GCLF, essentially its entire bright half. The internal photometric measurement uncertainty is smaller than  $\sigma(B - I) = \pm 0.10$  mag for  $M_I < -8.5$  as well. This color spread is approximately the intrinsic Gaussian width of the blue sequence and is smaller than the width of the red sequence, allowing the bimodal sequences to be well resolved over the full magnitude range of interest here.

### 3.2. Measuring Effective Radius and Aperture Corrections

As mentioned above, the single most important structural parameter we are after is the effective or half-light radius of the GCs around these giant ellipticals. This quantity is what determines the amount of “aperture correction” to apply to the measured magnitudes. In addition, the cluster scale sizes are interesting in their own right as possible functions of galactocentric position and GC metallicity and will be discussed separately below.

Within ISHAPE,  $r_{eff}$  is found by fitting the PSF-convolved cluster profile to each object in the image, then varying the assumed  $r_{eff}$  till a best fit is achieved. The code also returns a  $(S/N)$  ratio, which depends mainly on object brightness and can be used to assess the quality of the result. For any objects judged to be starlike, a value  $r_{eff} = 0$  is returned. There are other structural parameters that can be solved for in principle, including the ellipticity  $e$ , orientation angle  $\theta$ , and central concentration ratio, but these are easy to determine only for much more well resolved objects than we work with here.

ISHAPE uses a  $10\times$ -subsampled version of the IRAF/daophot PSF as a basis for its image convolution. For the intrinsic GC profile, it can use a variety of analytic functions; I adopt the King (1962) model since that model was defined originally to match real GCs and has been thoroughly tested in other star-cluster programs of this type (e.g. Larsen 1999; Larsen et al. 2001; Spitler et al. 2006; Georgiev et al. 2008). The GCs in the target galaxies here are not nearly well enough resolved to allow ISHAPE to solve independently for the cluster concentration ratio  $c \equiv \log(r_t/r_c)$  where  $r_t, r_c$  are the tidal and core radii, so a fiducial  $c = 1.5$  (“King30” in the internal notation of ISHAPE) was adopted for all the solutions, following Larsen (1999) and Larsen et al. (2001). This  $c$ -value matches the mean King-model concentration for the Milky Way, M31, and NGC 5128 globular clusters, among others (Harris 1996; Barmby et al. 2007; McLaughlin et al. 2008). In Fig. 1, the  $c$ -distribution for the Milky Way clusters is shown; 83% of the non-core-collapsed clusters are in the range  $1 < c < 2$ . In addition, ISHAPE was run with the assumption  $e = 0$ , because the vast majority of known globular clusters have quite modest projected ellipticities, mostly  $e < 0.1$  (e.g. Harris et al. 2002; Barmby et al. 2007). Through a set of simulations to be described below, the sensitivity and accuracy of the  $r_{eff}$  solution to the object’s brightness and assumed  $c, e$  were tested. In practice, ISHAPE returns the best-fit FWHM for the GC model profile, which must then be converted to an actual effective or half-light radius through a multiplicative factor that depends on  $c$ ; for the specific case of the King30 model,

$$r_{eff} \equiv r_h = 1.48FWHM.$$

In all cases except the few objects that happened to be affected by extreme crowding (neighbors within about 3 px), the residual maps plainly showed good fits to the PSF-convolved model. Some sample ISHAPE fits to three different objects are shown in Figure 3.

Knowing the value of  $r_h$ , a self-consistent procedure for defining the total magnitude of the object must be constructed. The procedure adopted here was to start with a *fixed-aperture* magnitude for the object using  $r_{ap} = 2.5$  px, with the standard tools in daophot (Stetson 1987). This fiducial 2.5-px radius is slightly larger than the stellar FWHM of  $\simeq 2$  pc but yet small enough to avoid crowding issues. This magnitude was then corrected to “large” aperture with a curve of growth (COG) of enclosed light versus aperture size; for the purposes of this paper, I adopt  $r_{max} = 20$  px =  $1''$ , at which the curves-of-growth for starlike and marginally resolved objects have accurately converged. The key point is that each value of effective radius has its own curve of growth, with more extended objects having relatively more of their light at larger radius.

A complete grid of COGs generated through the ISHAPE simulation tools, for values of FWHM ranging from 0 to 3 pixels, is shown in Figure 4. This range corresponds to  $r_{eff} \simeq 0 - 30$  pc linear radius, a generous coverage of the sizes of known GCs and even UCDs. More realistically, we would expect the GCs in these galaxies to have radii  $\lesssim 6$  pc =  $0.6$  px if they at all resemble known GCs. As can be seen from the Figure, this primary range of interest is marked by the solid vertical bar in each panel. The figure shows that the COGs converge extremely well to the same total magnitude at the large (20-px) radius and the aperture corrections are small. It can readily be seen that this procedure is equivalent to making the 2.5-px aperture magnitude brighter *by the amount needed to shift it onto the starlike curve* ( $r_{eff} = 0$ ); then, the correction from 2.5 px to 20 px aperture radius is made along the starlike curve, which is the upper envelope of the grid of tracks in the Figure.

Figure 5 shows the magnitude correction  $\Delta m(2.5px - 20px)$  as a function of object FWHM for the two filters. Again, the regime of interest here is almost entirely at the lower end ( $r_{eff} \lesssim 0.6px$ ) where the aperture corrections are quite small. In practice, for about a third of the objects in the measured sample, the sizes turn out to be indistinguishable from stars, though most of these starlike objects are also very faint and of no interest in the following discussion. In addition, the correction curves in *B* and *I* are nearly parallel, so that the net aperture correction to the *color* ( $B - I$ ) is very small.

The images in the *I*-band go slightly deeper than in the *B*-band for objects with GC-like intermediate colors, so that the  $S/N$  of the ISHAPE solutions is higher in *I*. This comparison is illustrated in Figure 6 for the NGC 4696 field, in which  $(S/N)_B \simeq 0.4(S/N)_I$ . The results for all the other fields are quite similar. The COG appropriate for each filter was used to define the total *B* and *I* magnitudes for each object. Finally, the  $S/N$ -weighted mean of  $r_{eff}(I)$  and  $r_{eff}(B)$  was adopted as the fiducial effective radius. The color index of each GC follows directly from  $(B - I) = B_{tot} - I_{tot}$ .

### 3.3. Tests of the GC Size Measurement

#### 3.3.1. Sensitivity to Central Concentration

Although the King30 model accurately represents the mean for real GCs, the individual  $r_i/r_c$  ratios can differ between GCs by factors of 3 or more in either direction, or  $\pm 0.5$  in  $c$  (see Fig. 1). To test the sensitivity of the solutions to the adopted  $c$ , I repeated the solutions on several of the galaxy fields adopting much higher and lower  $c$ -values: in the ISHAPE notation, these were King10 ( $c = 1.0$ ), King15 ( $c = 1.2$ ), and King100 ( $c = 2.0$ ). Sample differences for two of the fields are shown in Figure 7. These tests show that for clusters with intrinsically large radii  $r_h \gtrsim 0.05'' = 1$  px, the choice of  $c$  is important and systematic differences in the deduced cluster size occur that grow with  $r_h$ . However, for these rare big objects  $c$  can be allowed to be a free parameter within ISHAPE and explicitly solved for. At smaller radii ( $r_h \lesssim 0.05''$ ) the systematic differences are less than  $0.01''$ . Said differently, for these tiny objects  $c$  cannot be solved for as a free parameter, but making the wrong assumption for  $c$  leads to only very small systematic errors in the deduced size relative to the correct value: if the assumed  $c$  is too small,  $r_h$  is very slightly overestimated, and if  $c$  is too large,  $r_h$  is slightly underestimated (see also Georgiev et al. 2008, for similar tests and conclusions). The numerical reason why  $r_h$  is rather insensitive to  $c$  in this small-object regime is simply that the conversion factor  $f(c) = (FWHM/r_h)$  depends on  $c$  itself, and so an initial overestimate of the FWHM is mostly compensated for by an opposite change in  $f(c)$  to reach an equally good fit. In this “marginally resolved” regime, the object-to-object rms scatter and systematic shift together add up to an uncertainty  $\sigma(r_h) = \pm 0.003''$  due solely to the intrinsic uncertainty in  $c$ .

#### 3.3.2. Sensitivity to Cluster Ellipticity

The assumption  $e \equiv 0$  is clearly an idealized case. If a cluster is actually elliptical, how much of an effect will that assumption have on the deduced  $r_h$ ? Figure 8 shows the results of an extensive set of simulations. Here, artificial clusters of intrinsic shape  $e = (1 - b/a) = 0.2$  over a wide range of brightness *and* a wide range of sizes were convolved with the PSF, put onto an image with realistic background noise, then remeasured with ISHAPE. It should be noted that the adopted value  $e = 0.2$ , though modest, is already much larger than the ellipticities of most real GCs, so that any bias that shows up in these tests will be an upper limit to the average for real clusters.

In Figure 8, the *measured* FWHM from ISHAPE is plotted as a function of  $S/N$  (essentially the brightness of the object). In the left panel, ISHAPE is allowed to solve for  $e = 1 - (b/a)$  as a free parameter, and in the right panel, the code is required to assume  $e = 0$ . The four different rows show input objects from big to small, with semimajor axis from 1.0 down to 0.1 px (that is, from 50% down to 5% of the PSF width). In both cases, the true value of the FWHM is accurately returned for  $S/N \gtrsim 50$  and for intrinsic sizes bigger than about 10% of the PSF FWHM. For fainter and smaller objects than these limits, the solution for the object size becomes indeterminate.

Additional tests of the accuracy of the solutions are

shown in Figure 9. Here, the results from the same simulations are shown for the measured axial ratio  $b/a$  and for the orientation angle  $\theta$ . For these simulations the “right” answers (the input values) are ( $b/a = 0.8, \theta = 45^\circ$ ). The results of these tests show once again that for the brighter objects with  $S/N > 50$  and intrinsic sizes  $\text{FWHM} \gtrsim 0.2$  px (about 10% of the PSF size), accurate answers are returned. For the faintest objects, however, the spread of solutions for  $\text{FWHM}, (b/a)$ , and especially  $\theta$  rapidly blows up. For the smallest objects as well ( $\text{FWHM}$  less than 10% of the PSF width), the solutions for object shape and orientation are unreliable.

The random measurement uncertainty for  $r_h = 1.48 \text{ FWHM}$  in the regime  $S/N > 50$  and  $r_h < 0.5$  px is, from the simulations,  $\sigma(r_h) = 0.0025''$ . No systematic errors in the solutions for the object size, shape, and orientation occur until  $\text{FWHM} < 0.1$  px, at which stage the object can be treated as virtually starlike.

### 3.3.3. Intrinsic Scatter and Total Uncertainty in Size Measurements

A convenient summary of the range of object sizes that ISHAPE can be expected to solve for is shown in Figure 10. This is the result of a separate set of simulations where the input objects all have  $(S/N) > 50$  and a range of sizes extending from “starlike” ( $\text{FWHM}=0$ ) up to  $\text{FWHM}=5$  px. Just as in the previous tests, the model cluster has a King30 profile and it is convolved with a PSF with width 2.0 px. Each point shows the average of many dozens of simulated objects, with the error bar representing the standard deviation of the individual scatters around the means. The graph shows that for these relatively bright objects, the measured sizes are *systematically* accurate down to 10% of the PSF size, in agreement with the findings of Larsen (1999).

The consistent message from all these tests is that we can accurately recover the true size and shape of the object if it is reasonably bright and large enough to satisfy  $\text{FWHM} \gtrsim 0.1 \text{ FWHM(PSF)}$ . For objects in this “well conditioned” range, the total uncertainty in our size measurements can be summarized as follows.

- (a) The random uncertainty in the object size due only to the ISHAPE fitting procedure, as noted above and shown from the scatter in Figs. 8 and 10, translates to a mean of  $\pm 0.0025''$ .
- (b) The additional uncertainty due to the possible range of  $c$ -values (Fig. 7) averages  $\pm 0.003''$ .
- (c) Finally, there is an external uncertainty due to the PSF size itself. The numbers listed in Table 2 show that for each galaxy field and filter, the actual PSF width is internally uncertain by typically  $\pm 0.0033''$  in  $B$  and  $\pm 0.0018''$  in  $I$ . These translate to an ISHAPE fitting uncertainty in  $r_h$  of about  $\pm 0.005''$ .

Summing these three independent effects in quadrature, we obtain a net random uncertainty per object of  $\sigma(r_h) = \pm 0.006''$  or  $\pm 0.12$  pixel. For a galaxy at  $d \sim 40$  Mpc, this converts to a true uncertainty in scale size of typically  $\sigma(r_h) = \pm 1.1$  parsecs due solely to the GC profile-fitting procedure.

A comparison of the measured object sizes, done independently on the  $B$  and  $I$  images, is shown in Figure 11 for each of the six galaxy fields. In most cases, the mutual agreement between the two filters is good and well within the expected differences due to PSF-size uncer-

tainty. The one exception is for NGC 1407, where  $r_h(B)$  is systematically bigger than  $r_h(I)$  by  $\sim 0.2$  px, an offset almost twice as large as the expected uncertainty due to the PSF sizes mentioned above. The first source of this anomaly to suspect would be that the PSF size in this particular field is too big in  $I$ , or too small in  $B$ , or some combination of these; however, the PSFs in both filters have very much the same intrinsic widths as in the other five fields (Table 2) and were derived with exactly the same careful iterative procedure. Further tests have not revealed any clear solution and I have chosen to leave the results as they are, at very least to ensure that the final procedures for all the fields are homogeneous. The net effect on the mean cluster sizes for NGC 1407 is not as large as this comparison might indicate, because the final  $r_h$  value is the weighted average from the two filters and the  $I$  filter carries most of the weight (see Fig. 6).

Fig. 11 also allows us to make one last test of the internal measurement uncertainties. The FWHM measurements are done separately for the same objects on the  $B$  and  $I$  frames, with independently determined point-spread functions, so the scatter in the  $B, I$  size measurements provides a reasonable estimate of the measurement uncertainty. The rms scatter is closely similar over all six fields, and averages  $\sigma(r_h) = 0.16$  px, equivalent to  $\pm 0.008''$ . Accounting for the fact that the final  $r_h$  values are the average of  $B$  and  $I$  then reduces the uncertainty to  $\pm 0.006''$ , in close agreement with the estimate given above.

## 4. THE COLOR-MAGNITUDE DISTRIBUTION

With the object size measurement and aperture photometry complete, we now have a database of  $(B, I)$  photometry where the magnitudes of each individual object were determined starting from small-aperture photometry and then fully size-corrected to total magnitudes. The resulting distributions in the raw color-magnitude plane ( $I, B - I$ ) are shown in Figure 12.

In each galaxy the bimodal GC sequences are evident, but the first question to deal with is to ask how these new, recalibrated data match up with the previous photometry based primarily on PSF-fitting (Harris et al. 2006). A graphical comparison is shown in Figure 13. The huge statistical weight of the combined data, compared with any other GCS study, can be realized by noting that this diagram contains 15000 objects that were measured by *both* psf and corrected-aperture methods, most of them globular clusters.

Partially anticipating the results of the later discussion, we use the mean lines for the blue and red GC sequences in Fig. 13 (calculated as described later in Section 6.1) to note that both the old and new datasets define closely similar bimodal sequences. In other words, completely reworking the data according to a technically improved procedure has yielded no first-order change. The major reason for this similarity is that the cluster sizes are small enough that the individual aperture-size corrections relative to the fiducial starlike curve (Fig. 4) are modest. When they are differenced between  $B$  and  $I$ , the aperture-size corrections to the *color indices* are even less.

To a finer level of detail, comparison of the two datasets shows that the final colors in the present size-corrected data are a few hundredths of a magnitude bluer than

in the older data, particularly in the bright range  $M_I \lesssim -10$ . As will be seen in the next sections, this offset is *not* due to some particularly strong size/luminosity relation, because the characteristic sizes of the GCs have large scatter at any luminosity, and they are all individually accounted for. The net result is that the deduced MMR on the blue sequence (the slope of the correlation between luminosity and color) is still present but at slightly lower amplitude than in the earlier data. These outcomes will be discussed in more detail below. First, however, we look more thoroughly at the distribution of sizes of the clusters themselves, which have several points of interest in their own right and are an important preamble to the features of the MMR.

## 5. ANALYSIS OF THE CLUSTER SIZES

The characteristic (half-light) radius of a GC is an astrophysically valuable and frequently used quantity because it is expected to stay nearly invariant with internal dynamical evolution well after the initial cluster formation period (e.g. Spitzer & Thuan 1972; Aarseth & Heggie 1998; Baumgardt et al. 2002; Trenti et al. 2007), and so the measured  $r_h$  should represent an intrinsic structural property built in at an early time. It has long been realized that  $r_h$  shows large cluster-to-cluster differences but on the average it increases systematically with (three-dimensional) Galactocentric distance  $r_{gc}$  in the Milky Way (van den Bergh et al. 1991) following a rough scaling rule  $r_h \sim r_{gc}^{0.5}$ . This trend is generally interpreted as meaning that proto-GCs in the process of formation will take up systematically larger scale sizes if forming within shallower surrounding potentials. Similar, though weak, correlations in the observed  $r_h$  over a large range in *projected* (two-dimensional) galactocentric distance  $R_{gc}$  have been found in other galaxies such as the edge-on disk galaxies NGC 5866 (Cantiello et al. 2007) and NGC 4594 (Spitler et al. 2006), and the nearby gE NGC 5128 (Gómez & Woodley 2007), typically scaling as  $r_h \sim R_{gc}^{0.2 \pm 0.1}$ . A similar trend can also be found within the composite data for the Virgo galaxies (Jordán et al. 2005), though the data in this case cover a much smaller range in  $R_{gc}$ .

In addition, differences in the mean  $r_h$  between red (metal-rich) clusters and blue (metal-poor) clusters *at the same galactocentric distance* have been noted (see Kundu et al. 1998, 1999; Larsen et al. 2001; Jordán et al. 2005; Spitler et al. 2006; Gómez & Woodley 2007, for a sampling of the key results). The effect claimed in these papers is for the metal-richer clusters to be about 20% smaller than the blue ones. Although considerable scatter in  $r_h$  is found in each subgroup, this mean difference has persisted as the size and quality of the available measurements have increased. This size difference has been suggested to be the result of a geometric projection effect (Larsen & Brodie 2003) whereby the metal-richer clusters lie in a more centrally concentrated distribution within the galaxy, so that a higher proportion of them are at smaller  $R_{gc}$  and thus physically smaller because of the  $r_h/R_{gc}$  correlation. Alternately, Jordán (2004) suggests that the difference is an intrinsic function of metallicity and the result of metallicity-dependent stellar evolution times.

Data that cover a large range in  $R_{GC}$  and that are based on large statistical samples of clusters are needed to sort out the interpretations. If the difference is due to a projection effect along the lines suggested by Larsen & Brodie (2003), then it should become much smaller at larger distances outward into the halo.

### 5.1. The GC Size Distribution

The database of  $r_h$  values from the six giant ellipticals in this paper clearly does not have highly reliable *individual* measurements of cluster size. But it has the compensating advantages of *large sample size* and coverage of a *large range in galactocentric distance* ( $R_{gc}/R_{eff}$ ). The measurements for our six fields are displayed individually in Figure 14. Here, the half-light sizes are shown for all objects with  $r_h > 1$  pc regardless of their internal quality (that is, not selected by  $(S/N)$ ; the particular cutoff of 1 pc will be justified below). In every graph, the bimodal nature of the color distribution is evident, as well as a consistent pattern for the blue GCs to extend up to larger sizes than do the red GCs.<sup>2</sup>

If the GCs in these giant ellipticals are basically the same kind of star cluster as the classic Milky Way clusters, then we would expect their size distribution as a whole to resemble the Milky Way's. In Figure 15, the combined results for all six fields are shown in histogram form. Here, the database is sampled in a different way than in the preceding Figure: objects of all colors are included regardless of their  $r_h$  value, but only the highest-quality measurements ( $S/N > 50$ ) are included. This selection leaves 3330 objects over all half-light radii. For  $r_h \lesssim 2$  pc (the shaded region, equivalent to  $0.01''$  at a distance of 40 Mpc), we approach the limit of measurement of the profile fitting code and any smaller values for the intrinsic size returned by ISHAPE become very uncertain. The typical internal uncertainty *per object*, from the arguments in the previous section, is  $\pm 1$  pc, shown as the error bar at upper right. In other words, for the extreme case  $r_h < 1$  pc, GCs cannot be distinguished from stars even under the most optimistic reading of the data. However, it should be noted that GCs this compact physically appear to be quite rare (there are only two this small in the Milky Way).

While keeping in mind the measurement limits mentioned above, the total histogram shown in Fig. 15 clearly has two major components: the dominant GC population peaking at  $r_h \simeq 2$  pc; then a dip near  $r_h = 1$  pc and a secondary peak at  $r_h = 0$  which should consist of all the starlike or near-starlike field contaminants plus the most compact GCs. As a further test, ISHAPE was run on a simulated population of 5300 *starlike* objects ( $r_h \equiv 0$ ) over a wide range of brightnesses mimicking the range of the real data. The size measurements of these stars are shown in Fig. 15 as the green histogram. The width of this histogram should give a reasonable estimate of the internal precision of the profile-fitting results. The vast majority of these simulated stars fall within  $r_h < 1$  pc and confirm the empirical internal error estimate of  $\pm 1$  pc deduced above.

<sup>2</sup> The mean  $r_h$  values for NGC 1407 are noticeably smaller, a likely result of the discrepancy between the PSF sizes in *B* and *I* as discussed above. However, this galaxy provides less than 10% of the total GC population in the study, and whether or not it is excluded has no important effect on the subsequent discussion.

These various tests of the data show that the total spread of the major GC component that continues on upward past  $r_h \sim 2$  pc is too large to be explained simply by measurement scatter. It is completely consistent with the interpretation that we have genuinely resolved the intrinsic size distribution of the globular clusters around these galaxies. A final key test is to compare it with the Milky Way GC sizes. In Fig. 15 the Milky Way data from Harris (1996) are shown in the dotted histogram for the 66 clusters with luminosities  $M_V < -7.3$  (i.e., brighter than the turnover point of the GC luminosity function), and no further from the Galactic center than 20 kpc. Selecting the Milky Way sample this way makes it closely comparable to the GC sample that we have in the giant elliptical data. The overall shapes of the two datasets resemble each other remarkably well, particularly their extension to large radii.

A second-order difference is that the Milky Way  $r_h$  distribution peaks at a point about 0.5 pc bigger than the peak for the giant elliptical data. This offset corresponds to an angular size difference of  $\Delta r_h \simeq 0.0025''$  at  $d \sim 40$  Mpc and is entirely within the internal uncertainties of the measurements in this paper. *If* the offset is physically real, however, it is likely to be because the gE's have a much higher proportion of red (metal-rich) GCs than does the Milky Way, and as will be seen below, the red GCs are systematically smaller than the blue GCs by  $\sim 0.5$  pc (see Table 3 for the median values in the Milky Way).

### 5.2. Correlations of GC Size with Other Factors

Having presented the overall size distribution, we now investigate correlations with the three properties that have been suggested in the previous literature to influence GC scale size: luminosity, metallicity, and galactocentric distance. Differences in GC scale size with *metallicity* have drawn the most attention in recent work, primarily from the HST-based photometry of GCs in nearby galaxies (Kundu et al. 1999; Larsen et al. 2001; Jordán et al. 2005, among several others). These same studies have not, however, been used to track size correlations with either luminosity or spatial location very effectively, because (a) as will be seen below, the size difference with cluster luminosity becomes obvious only at the top end of the luminosity range where GCs are rare; and (b) these previous studies were almost entirely restricted to the inner-halo clusters within about 1.5 effective radii of the galaxy spheroid light, so that only a very limited run of spatial location could be traced. The database in this study has the advantage that all three factors can be traced at least to some degree.

In Figure 16, the  $r_h$  distributions are shown now for the 2454 GCs bigger than 1 pc and with  $(S/N) > 50$ . The right panel shows the histograms separately for the metal-poor GCs (those with  $(B - I)_0 < 1.8$ ) and the metal-rich ones ( $(B - I)_0 > 1.8$ ). The expectations from the previous literature are borne out here, that the lower-metallicity GCs are systematically bigger on average by  $\sim 0.5 - 1$  pc, or roughly 15 - 20%. It is highly unlikely that this difference is just an artifact of measurement, because all the objects in the database, red and blue alike, were measured through both  $B$  and  $I$  filters and appropriately  $S/N$ -weighted. Both types of clusters also appear at all galactocentric distances and over the full

range of GC luminosities allowed by the magnitude limits of the photometry.

One *caveat* in these kinds of comparisons is that the sample has been deliberately truncated for  $r_h < 1$  pc. This should, however, have only a small effect on such diagnostic quantities as the median size of a subsample, because at least in the Milky Way virtually no clusters have such ultra-compact structures (Fig. 15).

The distribution of sizes versus cluster *luminosity*, shown separately for the blue and red GCs, is in Figure 17 and the median sizes in half-magnitude bins are listed in Table 3. As in the previous figure, the 2454 objects with  $(S/N) > 50$  and  $r_h > 1$  pc are shown. For luminosities higher than  $M_I \simeq -11$  (corresponding to about  $10^6 L_\odot$ ) the clusters show a weak trend to become larger with increasing luminosity. For the lower-luminosity range  $M_I \gtrsim -11$ , any trend of median cluster size with luminosity is modest at best and perhaps not significant. Both of these results agree with what has been found in the Local Group galaxies (e.g. Barmby et al. 2007).

On average, the median GC size of the blue clusters is 15-20% bigger than the red clusters, at any luminosity. A standard Kolmogorov-Smirnov two-sample test also shows that their size distributions are different at  $> 99\%$  significance.

In the previous literature, correlations of size with galactocentric distance have also been suggested. Even within the Milky Way, which is the only galaxy for which we can explore that correlation in three dimensions, the trend is relatively modest, and when it is projected onto two dimensions for any other galaxy it can be expected to be even shallower. Nevertheless, the data in this paper can be used to gain some idea of any such correlation because the range of  $R_{gc}$  is quite large for each of the six galaxies. To normalize all the data to a common system and allow treatment of all the galaxies together, we express the projected  $R_{gc}$  value for each cluster in units of  $R_{eff}$ , the effective radius of the galaxy's spheroid as determined from its surface brightness profile (see Table 1 and the NED).

A schematic representation of the combined effects of spatial location and metallicity together is shown in Figure 18, where size versus color is plotted in three different spatial zones: the inner halo ( $R_{gc} < R_{eff}$ ), the mid-halo ( $R_{eff} < R_{gc} < 2R_{eff}$ ), and the outer halo ( $R_{gc} > 2R_{eff}$ , extending out as far as  $5R_{eff}$ ). A more quantitative comparison is shown in Figure 19 and Table 4. Here, the median values in bins of  $\Delta R = 0.5$  are plotted separately for the two metallicity subgroups. These show a weak trend for both types of clusters to have systematically larger scale sizes farther from their galactic center. Furthermore, the slopes of both relations are quite similar: least-squares solutions for the medians give

$$r_{h,med} (pc) = (2.236 \pm 0.079) + (0.203 \pm 0.030)(R_{gc}/R_{eff}) \quad (1)$$

for the blue clusters, and

$$r_{h,med} (pc) = (1.881 \pm 0.043) + (0.181 \pm 0.016)(R_{gc}/R_{eff}) \quad (2)$$

for the red clusters. Consistent with what was found earlier, the blue GCs are larger by 17% than the red GCs, and this difference does not change significantly



with  $R_{gc}$  bin.

A power-law formulation of the same trend (van den Bergh et al. 1991; Spitler et al. 2006; Gómez & Woodley 2007) has perhaps a stronger physical motivation and yields an equally good representation of the data. The best-fit equations in this form (for the blue and red clusters respectively) are also shown in Fig. 19 and are given by

$$r_{h,med}(pc) = 2.53(R_{gc}/R_{eff})^{0.11}, \quad (3)$$

$$r_{h,med}(pc) = 2.15(R_{gc}/R_{eff})^{0.11}. \quad (4)$$

There are only two other galaxies beyond the Local Group for which GC-size measurements cover a similarly large run in spatial location: NGC 5128 (Gómez & Woodley 2007), with data extending out to  $\sim 8R_{eff}$ ; and NGC 4594 (Spitler et al. 2006), with data out to  $\sim 6R_{eff}$ . Both of these galaxies are relatively nearby and thus their GCs are better resolved, but the sample sizes are about one order of magnitude smaller than the one used here. Nevertheless, these two studies find power-law dependencies for  $r_h(R_{gc})$  with very much the same power-law slopes  $\sim 0.1 - 0.2$  as found here. In short, all the current data suggest a consistent pattern for a shallow but steady outward increase in cluster scale size regardless of metallicity.

### 5.3. Interpretation

A brief summary of the findings for the cluster scale sizes in these six giant ellipticals can be made as follows:

- The characteristic half-light radius depends weakly and nonlinearly on total luminosity: for the lower-luminosity range that contains the vast majority of the clusters, i.e. the range  $M_I \gtrsim -11$  or  $L \lesssim 10^6 L_\odot$ , the median  $r_h$  for clusters of all metallicities remains largely independent of luminosity, whereas for the bright end  $M_I \lesssim -11$  the median GC size begins to increase steadily. For the extremely rare and very most luminous GCs at  $M_I \simeq -12.5$ , the scale sizes are almost twice as large as the median for the lower-luminosity range (Fig. 17).
- At any luminosity, and at any galactocentric distance, the metal-poor (blue) clusters are systematically larger than the metal-rich (red) ones by  $(17 \pm 2)$  percent (Figs. 17, 18, and 19).
- Lastly, there is a consistent correlation of GC scale size with projected galactocentric distance, at any metallicity, equal to  $r_{h,med} \sim R_{GC}^{0.1}$  (Figs. 18 and 19).

Given the limited material that was available from previous work, the fact that all three correlations are comparably weak explains why it has been difficult to separate them from one another, or indeed to decide whether or not each one is even present.

The systematic increase in scale radius with luminosity for the highest-mass clusters already has clear evidence in its favor from the Local Group galaxies (Barmby et al. 2007) and the brightest GCs and Ultra-Compact Dwarfs (UCDs) in the Virgo and Fornax galaxies (Hasegan et al. 2005; Evstigneeva et al. 2007, 2008). Spitler et al. (2006)

also found a significant increase in mean size with luminosity for the GCs in the Sombrero galaxy, with a noticeable “onset” point near  $M_V \simeq -9$  above which the effective radii begin to increase most strongly. These studies show repeatedly that these compact, massive stellar systems have  $\langle r_h \rangle \sim const$  for luminosities less than  $M_I \simeq -11 \equiv 10^6 L_\odot$ , and then gradually swing upward to a scaling  $\langle r_h \rangle \sim L_V^{0.7}$  which bridges them to other objects such as dE nuclei and eventually dwarf galaxies (see, e.g., Fig. 2 of Evstigneeva et al. (2008) for a useful and up-to-date composite diagram). Nevertheless, the current data show few luminous GCs that match the larger sizes associated with UCDs. The mean size/luminosity relation for UCDs, taken from Evstigneeva et al. (2008) and converted to  $M_I$  with  $(V - I) = 1.0$ , is plotted as the dashed lines in Fig. 17. Most of the GC data from these giant ellipticals lie well below the UCD curve even at the highest luminosities. In other words, most of the “classice” luminous GCs have compact structures that are smaller than UCDs. These GCs with  $M_I \lesssim -11.5$  instead more closely match the *lower envelope* of the data discussed by Evstigneeva et al. (2008). This lower envelope is populated mostly by a handful of dE,N nuclei. This comparison, perhaps, provides additional hints that the most luminous normal GCs may have had their origins as the nuclei of dwarfs that were later stripped as they were accreted by the giant elliptical.

It should be kept in mind, however, that in a normal GC luminosity distribution with turnover at  $M_I \simeq -8.3$  and dispersion  $\simeq 1.4$  mag, only  $\sim 1\%$  of the entire GC population lies above  $M_I < -11$ . For the lower-luminosity GCs that make up the vast majority, the assumption  $r_h \sim const$  continues to be a useful one.

The present study was not especially tuned to measuring the sizes of larger UCD-like objects, so a separate analysis of them in these fields will have to be conducted. Work of this kind has begun and will appear in a later paper.

In the model of Larsen & Brodie (2003), the mean size difference between metal-poor and metal-rich clusters is a geometric projection effect: if the intrinsic size distribution for all clusters is actually the same, and if they all follow the same  $r_h(r_{gc})$  trend, then the metal-rich ones will be smaller on average because their spatial distribution is more centrally concentrated to the galactic center. The later discussions of Spitler et al. (2006) and Gómez & Woodley (2007) supported this interpretation. By contrast, Jordán (2004) presents an alternative model whereby the metallicity-based size difference is the end result of many Gy of dynamical evolution and mass segregation within the GC combined with stellar-evolution timescales that depend on metallicity. Yet another possibility is that metallicity may have a more direct and much earlier effect on cluster size, in the sense that higher heavy-element abundance in the protocluster gas may encourage more rapid cooling and cloud contraction before the stars form, allowing a metal-rich cluster to have a smaller scale size from the start. Detailed models along that line have yet to be pursued.

Larsen & Brodie (2003) suggest that if the projection-effect model is correct, then the sizes of high- and low-metallicity clusters should become the same at large galactocentric distance well outside the galaxy core. Un-

der these assumptions, their quantitative models show that the red-vs.-blue size difference should be greatest within one or two  $R_{eff}$ . However, the data here (see especially Fig. 19) indicate that this is not the case: metal-rich GCs are systematically smaller than metal-poor ones by much the same factor at all locations, favoring the view that the metallicity-based difference is intrinsic. At the same time, both types of clusters follow a size/distance dependence  $r_h \sim R_{gc}^\alpha$  with a similar power-law scaling exponent  $\alpha$ , but just with different zero-points. This effect strongly suggests that metallicity is not the whole story. The scale sizes of the clusters are at least partly determined by the depth of the tidal field that they are formed in, ending up with more extended structures in environments of shallower external potential wells, such as in dwarf galaxies or the outer halos of large galaxies. Notably, in a recent survey of GCs in many nearby dwarf galaxies, Georgiev et al (2008, 2009) find a median  $r_h = (3.2 \pm 0.5)$  pc, and  $r_h \sim 5$  pc in the LMC. Sizes this large are reached in our gE sample only for the outer regions at several  $R_{eff}$ .

A final overview of this part of the discussion is that the scale sizes of globular clusters appear to be determined jointly and universally by their metallicity, spatial locations, and (at very high luminosity) their mass: all three of these effects are physically real and need to be included in their conditions of formation. Deeper modelling of the combined effects of formation, space distribution, and dynamical evolution is far beyond the scope of this paper, but the sum total of all available data now appears to provide enough evidence to motivate such models.

## 6. THE MASS/METALLICITY RELATION

The final magnitudes and colors of the globular cluster populations in our six gE galaxies, as shown in Figs. 12 and 13, are based on fully size-corrected magnitudes and can now be used to investigate the blue and red GC sequences in more detail. The important questions, beyond the first-order one of establishing the basic bimodality of the GC color distributions, are to ask whether either sequence shows a detectable mass/metallicity relation; and whether the slope or form of that relation might itself depend on cluster luminosity. Beyond that, we would like to test its behavior versus other external characteristics such as cluster size or galactocentric distance.

### 6.1. Bimodal Fitting to the GC Sequences

The approach to defining the MMR adopted here is to measure the mean color of each sequence independently at many points along the luminosity range (Harris et al. 2006; Mieske et al. 2006). In some other previous studies (Strader et al. 2006; Spitler et al. 2006; Cantiello et al. 2007; DeGraaff et al. 2007; Spitler et al. 2008), mean linear relations in color versus magnitude were fit to each sequence and the best-fit slopes were quoted. If the GC sequence has the form  $\Delta(\text{color})/\Delta(\text{magnitude}) = \text{const}$ , then this translates readily to a power-law form in heavy-element abundance versus GC luminosity,  $Z \sim L^p$ , as long as the color index varies linearly with  $[\text{Fe}/\text{H}]$ . However, the linear-fit approach imposes an uncomfortably strong assumption on the data. The raw data provide no *a priori* guarantee that the mean GC colors will vary linearly with magnitude, and a forced linear

fit will miss any nonlinear trend that might be present. Whether or not the MMR disappears below a certain mass range, for example, is important for key features of the self-enrichment model (Bailin & Harris 2009). Fewer assumptions are forced on the material by finding a bimodal fit to the distribution of GC colors in independent magnitude bins, and then inspecting the resulting mean points for any trends, linear or otherwise.

The tradeoff is that *if* the MMR actually has a linear or near-linear form *over the entire luminosity range*, then its slope can be determined by the linear-fit method with a smaller number of objects than is required for the bimodal fitting in independent bins. The approach I adopt here is that this linear-full-range assumption first needs to be tested independently on large, statistically unambiguous datasets before being carried over to smaller galaxies.

Another factor capable of biasing the deduced MMR is that of sample field contamination. In the present study, contamination by (mostly) faint background galaxies and a few foreground stars over a wide range of colors is nearly negligible over the brighter part of the GC population but grows to significant levels for  $I \gtrsim 24.5$  (see Fig. 12). The contamination on the blue side is typically larger and thus may leave the artificial impression of a too-steep MMR slope if a linear fit is imposed. A notable exception from previous literature is the database of Mieske et al. (2006) where the GCs in the Virgo galaxies were individually selected and the sample has low contamination. In general, however, bimodal fitting to the color distribution will be less affected by contamination than the linear-fit method since it is designed to pick out the peak color of each component regardless of the scatter of outlying points. The level of field contamination for the present data is very small for our main luminosity range of interest ( $M_I \lesssim -8.5$ , brighter than the GCLF turnover) but the issue will be discussed in greater detail in Section 6.2 below.

The RMIX multicomponent fitting code (MacDonald 2007) is used here to determine the bimodal fits. The code and its application for this problem are described in more detail in Wehner et al. (2008). In short, starting from either the individual datapoints or a previously defined histogram, RMIX finds the best-fit multimodal description of the color distribution. The user-specified input consists of the number of modes to be solved for; initial guesses at their means and standard deviations; and the basic fitting function to be used. The usual Gaussian model is most common, but half a dozen other well known functional forms are available within RMIX. The mean, standard deviation, and proportion of each component can either be fixed by the user or solved for in any combination.

The solutions for the six individual galaxies are summarized in Table 5 and shown in Figure 20. Here, magnitude bins  $\Delta I$  of at least 0.5 mag were used, but with the proviso that a minimum of roughly 100 objects fell into each bin. To keep the fewest possible external constraints on the solutions, RMIX was required only to assume a bimodal Gaussian distribution in  $(B - I)_0$  and then was left free to solve for the mean  $(B - I)$  colors  $\mu_1(\text{blue}), \mu_2(\text{red})$ , the standard deviations of each mode  $\sigma_1, \sigma_2$ , and their proportions of the total population  $p_1 + p_2 = 1$ . The input data included all objects

within the color range  $1.5 < (B - I) < 2.5$ , an interval chosen to reject the largest part of the outlying field contaminants while safely including both GC components. In a very few cases (individual bins here and there) it was necessary to constrain the fit in order to get convergence, usually by fixing the proportions of one or the other of the  $\sigma$ 's; these few cases are marked in Table 5 with internal uncertainties of zero. Overall, however, this solution technique differs very noticeably from most previous ones in the literature because the large GC populations allow these minimal constraints on the fits.

The maximum statistical weight can be obtained by combining all six systems into a single dataset, where everything is translated to the common scale of absolute magnitude and intrinsic color  $M_I, (B - I)_0$ . Bimodal RMIX fits for the combined data are listed in Table 6. These are also plotted in Figure 21, as are the mean points for the six individual systems.

Assuming that the photometry itself is systematically correct, the clear conclusions from these bimodal fitting results are that

- (a) A nonzero relation between luminosity and color exists along the blue-GC sequence particularly;
- (b) The trend is nonlinear in form; and
- (c) Along the red sequence, any such relation is gentler or absent.

I show in Figure 22 the CMDs for those objects with positive, nonzero size measurements from the ISHAPE fits (that is, objects with  $r_h > 0$ ), and then separately for all the rest of the objects that were either found to be starlike ( $r_h = 0$ ) or too faint for successful ISHAPE fitting. The vast majority of objects in the second category populate the area of the CMD fainter than  $M_I = -8.5$  and thus do not affect anything but the faintest bin of the RMIX bimodal sequence fits. Removing the starlike objects entirely (left panel of Fig. 22) does not change the best-fit red and blue GC sequences.

### 6.2. Background Field Contamination

Although the GCS populations clearly dominate the color-magnitude diagrams in the six galaxies studied here, it is useful to gauge the actual level of field contamination. The raw data in this HST/ACS program contain no true “control field” exposures pointed at adjacent blank fields. However, three of the galaxies imaged in the original program turned out to have small GC populations, and the outskirts of their fields can be used for an estimate of the field populations. These are NGC 5322, 5557, and 7049 (Harris et al. 2006). The advantages of using these fields are that they were taken with the same filter combinations and to the same absolute-magnitude limits, and the galaxies themselves have similar distances, foreground reddenings, and Galactic latitudes to the other six.

The fields of these other three target galaxies were all remeasured with the same procedures through daophot and ISHAPE as described above. Inspection of the color-magnitude diagrams showed that GC populations around them are definitely present in the inner regions, but die off with increasing radius until for  $R_{gc} \gtrsim 125''$  the GC numbers begin to fall below the general density of field objects that are widely distributed in color. Thus to generate a composite “control field” I have combined the regions beyond  $R_{gc} = 125''$ , which add up to a total area

11.2 arcmin<sup>2</sup>, conveniently equal to the area of a single ACS/WFC field.

The CMD for this synthetic control field is shown in Figure 23. Here the raw  $(I, B - I)$  data have been converted to  $(M_I, (B - I)_0)$  assuming  $(m - M)_I \simeq 33.1$  and  $E_{B-I} \simeq 0.05$ , which are the averages for NGC 5322, 5557, and 7049. The data for “starlike” objects ( $r_h = 0$ ) scatter uniformly across the CMD and should represent genuine field objects. By contrast, the data for the objects with  $r_h > 0$  should include some genuine GCs that belong to these three galaxies (at a distance of 40 Mpc,  $R_{gc} = 125''$  corresponds to a linear projected distance of only 25 kpc, which is still well within the bounds of typical gE halos), along with a variety of small background galaxies. Traces of the red and blue GC sequences can indeed be seen in the middle color range. In other words, the composite field data can represent only an approximate *upper limit* to the true level of field contamination in the six main target galaxies.

The distributions in color for the background data are shown in Figure 24. Here, the data are divided into three  $M_I$  luminosity intervals and compared with the data for the same ranges in the six main program galaxies that have the largest GC populations. In each case the “background” histograms have been multiplied up by a factor of 6 to match the total area coverage.

The presence of GCs in the field sample can be seen most noticeably in the upper two panels ( $M_I < -9.4$ ), where low peaks appear in the shaded histograms at  $(B - I)_0 \sim 1.6$  and 2.0, near the normal positions of the blue and red sequences. Otherwise, the field populations are consistent with a low and roughly flat, uniform distribution in color across our main color range of interest  $(B - I)_0 = 1.3 - 2.3$  where the GC population lies. Subtraction of a uniform pedestal of only a few percent amplitude does not change the identification of the GC sequence peak colors in the bimodal fits, and has the disadvantage of simply adding more noise to the data. The histograms have therefore not been explicitly corrected for this small and near-uniform background.

### 6.3. Characterizing the MMR

The next step in evaluating the color/metallicity distributions is to characterize their detailed structure. In Fig. 21, the *solid lines* come from the fits to the entire database and thus are weighted towards the galaxies with the biggest GC populations (in decreasing order of importance, they are NGC 4696, 7626, 3258, 3268, 1407, and 3348; the first two make up half the total and the last two only 17%). By comparison, the *individual points* in the figure give equal weight to all galaxies. Nevertheless, both approaches form a consistent pattern. The blue sequences in the galaxies show a trend to become redder at brighter magnitude *and* more strongly so along the upper half of their run. No equally strong trend appears along the red sequences.

Before attempting to parametrize either sequence, we first note that the most obvious transition region appears to be in the range  $-10 > M_I > -11$ , below which no significant MMR appears along either sequence, and above which the blue sequence is much closer to the red sequence:

- Along the blue sequence, the mean color for the

three brightest bins in Table 6 for  $M_I < -10.4$  is  $\langle B - I \rangle_0 = 1.689 \pm 0.035$ . For the five fainter bins  $M_I > -10.4$ , we have  $\langle B - I \rangle_0 = 1.573 \pm 0.009$ . The color difference between the brighter blue clusters and the fainter ones is thus  $\Delta(B - I) = 0.116 \pm 0.036$ , which is significant at the 3.2-sigma level. A standard Kolmogorov-Smirnov test between these two histograms shows that they are significantly different at much higher than the 99% confidence level. The largest deviation between the two cumulative distributions comes at  $(B - I)_0 = 1.6$ , precisely in the middle of the blue sequence.

- Along the red sequence,  $\langle B - I \rangle_0 = 1.946 \pm 0.026$  for the bright interval  $M_I < -10.4$ , while  $\langle B - I \rangle_0 = 1.985 \pm 0.009$  for  $M_I > -10.4$ . The difference  $\Delta(B - I) = -0.039 \pm 0.028$  is significant at only the 1.4-sigma level.

Another way to illustrate this luminosity-based trend is shown in Figure 25 and returns to the very first papers on the subject, by Ostrov et al. (1998) and Dirsch et al. (2003). These authors used GC photometry in the Fornax giant NGC 1399 to suggest that the brightest clusters made up a broad and perhaps unimodal color distribution, seemingly counter to the bimodality paradigm that had already become well established. In Figure 26, the color distributions over these two biggest magnitude intervals are shown for our six BCGs, along with the double-Gaussian deconvolutions for each one. The quantitative RMIX fits show that (a) for the brighter interval  $M_I < -10.4$  where the two modes are more strongly overlapped, a *unimodal* fit is nevertheless strongly rejected in favor of two components; (b) *only* two modes are necessary for an excellent fit to any part of the magnitude range; that is, the GC population in these galaxies is bimodal rather than multimodal.

As a demonstration that these fits are not dependent on the particular magnitude being used, Figure 27 shows the same comparison where now the sample is sorted by absolute  $B$  magnitude instead of  $I$ . The redder component is less prominent here and less certainly fit because the red-sequence GCs are much fainter in  $B$  than in  $I$ , but the same two modes are present with very much the same color difference as in the  $M_I$ -based fits. For the bright interval  $M_B < -9.0$ , we have  $\mu_1 = 1.650 \pm 0.022$ ,  $\mu_2 = 1.886 \pm 0.030$ , while for the faint interval  $M_B > -9.0$ , we have  $\mu_1 = 1.556 \pm 0.004$ ,  $\mu_2 = 1.971 \pm 0.006$ . The fits in  $M_I$  are to be preferred, first because the  $I$ -band is much more representative of the true bolometric luminosities of the clusters (Mieske et al. 2006), and second because (in the current dataset) the  $I$ -band photometry is slightly deeper and of higher precision.

Perhaps the cleanest version of the current GC data is presented in Figure 28. Here, the 7831 datapoints from all six galaxies, for the objects that have  $r_h > 1.5$  pc, are shown for the purpose of selecting a “best” dataset that minimizes field contamination, as discussed above. The MMR along each of the two components is gradual enough that it can be conveniently represented by simple polynomial fits. Useful interpolation equations in

$(M_I, B - I)$  are

$$(B - I)_0 = (2.543 \pm 0.513) + (0.237 \pm 0.103)M_I + (0.0143 \pm 0.0051)M_I^2, \quad (5)$$

for the blue sequence, and

$$(B - I)_0 = (2.142 \pm 0.089) + (0.017 \pm 0.009)M_I. \quad (6)$$

for the red sequence. These are derived from the mean points in Table 6 and are shown in Fig. 28 as the solid blue lines. The colors can be converted to metallicity through the standard transformation from the Milky Way clusters (Harris et al. 2006),

$$(B - I)_0 = 2.158 + 0.375 [\text{Fe}/\text{H}]. \quad (7)$$

However, these curves should not be used to extrapolate to fainter levels  $M_I > -8$ .

The red sequence has a barely significant slope, and is scarcely distinguishable from a vertical line at constant color at  $\langle B - I \rangle_0 = 1.97$ . In fact, the brightest two points along the red sequence are the least well determined in the whole dataset because of their relatively low population. Very minor differences in the adopted RMIX constraints (or lack of them) can shift the mean colors of these two bins by a few hundredths of a magnitude.<sup>3</sup>

An alternate form of the interpolation equations can be estimated more crudely by direct polynomial fits to the individual datapoints, bypassing the RMIX bimodal solutions entirely. To do this, I define the blue GCs to be the 4110 objects that fall within the color range  $1.3 < (B - I)_0 \leq 1.8$ , and the red GCs the 3625 objects that fall within  $1.8 < (B - I)_0 < 2.4$ . Then the polynomial fits become

$$(B - I)_0 = 2.186 + 0.152M_I + 0.0094M_I^2 \quad (8)$$

for the blue sequence, and

$$(B - I)_0 = 2.183 + 0.018M_I \quad (9)$$

for the red sequence. These are shown as the dotted lines in Fig. 28. The uncertainties on the fitted coefficients are the same as for the previous pair of equations. This second pair of interpolation equations generally agrees well with the first pair, but differs most noticeably at the highest-luminosity part of the diagram where the data are sparsest. The key potential problem with the second approach is that it ignores the effects of mutual contamination of the two sequences on each other: that is, some points belonging to the red sequence scatter blueward of the dividing line at  $(B - I)_0 = 1.8$ , and conversely some blue-sequence points fall redward of the same line. If the relative numbers of objects and the intrinsic widths of each sequence are not equal (which is certainly the case here), then the amounts of mutual contamination will not be the same and may bias the solutions for the equations. For this reason, I recommend that the first pair of equations (5,6) (the ones starting from the mean RMIX points) should be preferred because they more accurately pick out the centers of each sequence.

<sup>3</sup> See also Mieske et al. (2006), who demonstrate that the bimodal-Gaussian fitting procedure can end up producing a slight artificially positive slope to the red sequence if the two sequences are partially overlapped and not equally populated; see their section 3.2. The fitted slope deduced here is consistent with their results.

#### 6.4. Discussion and Comparisons

To summarize this part of the analysis, the very most basic conclusion is that the mean color of the blue-sequence clusters begins to change, with high statistical significance, at around the luminosity level  $M_I \sim -10.5$ . For a typical mass-to-light ratio  $(M/L)_I = 2$  (McLaughlin 2000), this level translates to a GC mass  $M \simeq 10^6 M_\odot$ . Below this level, the present data give no compelling evidence that there is a significant correlation between luminosity and color. Above this level, the blue GCs become significantly redder in the mean, causing the blue and red modes to overlap more strongly.

At the same time, this transition point does not seem to be abrupt. Figs. 20 and 21 suggest that the blue sequence makes a gradual changeover from a near-vertical sequence at fainter magnitudes, to a sloped one at brighter levels. The polynomial fits stated above reflect this changeover. For the range  $M_I < -9.5$  crossing the transition region, if we simply approximate the trend by a linear fit, the mean slope is  $\Delta(B - I)/\Delta(M_I) = -0.072 \pm 0.018$ . Since  $\Delta(B - I)/\Delta([\text{Fe}/\text{H}]) = 0.375$  (Harris et al. 2006), this translates to a heavy-element abundance scaling  $Z \sim L_{GC}^{0.48 \pm 0.12}$ . Extrapolating upward to the very most massive GCs known, this correlation suggests that the blue-sequence GCs at  $10^7 M_\odot$  should have an average  $\langle \text{Fe}/\text{H} \rangle \simeq -1.0$  instead of the “normal” mean  $[\text{Fe}/\text{H}] \simeq -1.5$  which the vast majority of the lower-mass ones have.

An “anomalous” feature in the bright-end distribution appears in the  $M_I$  range around  $-10.5$  to  $-11$ , where in Fig. 21, three of the red-sequence points stand noticeably off the main distribution. These three points are at  $(B - I)_0 \simeq 1.8$  and are all from the two galaxies NGC 3258 and 3268 (see Fig. 20). Referring back to the raw CMDs (Figs. 12 and 13) we see that this is the magnitude range where the overlap and blurring between the blue and red sequences becomes quite noticeable. The heavier overlap decreases the stability of the bimodal fitting and increases the internal uncertainties in all of the fitted parameters  $(\mu_{1,2}, \sigma_{1,2}, p_1/p_2)$ . My provisional interpretation is therefore that these anomalous points are primarily the result of small-sample statistics; the fact that these intermediate-color points do not show up in the bimodal fits to the combined sample of all six galaxies with its higher statistical weight (Table 6) provides some support for that conclusion. Nevertheless, the possibility should be kept in mind that our basic assumption of a two-sequence model – the assumption that is built in to almost every previous discussion of GC metallicity distributions – may not capture the entire nature of the color/metallicity distribution for these extremely high-mass clusters.

Because the photometry of the program objects is specifically corrected for their individual effective radii, any concerns that the basic existence of the MMR is merely an artifact of the measurement process are removed. This study, and the one by Mieske et al. (2006) for the Virgo galaxies, now provide the major HST-based datasets in which the GC photometry is accurately size-corrected.

Extensive comparisons of the different forms of MMR published in earlier papers are beyond the aims of the present work, though more such intercomparisons are

done by Cockcroft et al. (2009). They combine the results from most of these previous studies by converting the several different photometric color systems that have been used for different galaxies into a homogeneous metallicity scale, and correlate the results for the MMR slopes with galaxy luminosity and GCS specific frequency.

A still newer study by Waters et al. (2009) of the single galaxy M87 is of particular interest for the unusual photometric characteristics of the data. They use extremely deep HST/ACS imaging in  $V$  and  $I$  covering the inner 10 kpc ( $1.5R_{eff}$ ) of M87 to construct aperture-corrected photometry of about 2000 GCs, deep enough to cover almost the entire GCLF. Of these,  $\sim 1000$  are brighter than the GCLF turnover point (compared with more than 8000 from the six galaxies in this paper) and about 130 are brighter than  $M_I = -10.5$  (compared with over 750 from the present study). They find the normal, first-order bimodality of the MDF although with a large internal spread in the  $(V - I)$  colors, but also claim that that the blue GC sequence has no significant MMR slope. This conclusion relies on a forced linear-fit model over the whole magnitude range in  $(I, V - I)$  and is thus dominated by the 94% of the sample that is fainter than the actual MMR “turn-on” point at  $M_I \simeq -10.5$ . In fact, their data do not rule out the type of MMR that has been found here: that is, a near-vertical blue sequence on the fainter part of the magnitude range, moving upward to a stronger slope towards higher metallicity with a transition region above a million Solar masses. The data in the present study draw from a statistical sample more than 6 times larger, and in addition, use a photometric index  $(B - I)$  that is twice as sensitive to GC metallicity as is  $(V - I)$ .

Of the previous studies, the most closely comparable one is probably Mieske et al. (2006), who analyze GC samples from 79 Virgo ellipticals and perform bimodal-Gaussian fits to the GC color distributions with techniques very similar to the ones used here. Their database has similar size (a total of a few thousand GCs brighter than the GCLF turnover luminosity), uses a color index  $(g' - z')$  with similar metallicity sensitivity, and has a low level of field contamination. They divide the galaxies into four different luminosity groups (divided roughly speaking into supergiants, giants, normal ellipticals, dwarfs) and then discuss the trends of mean GC color versus magnitude in each group. The most important differences between their analysis and the present one are that (a) the Virgo data extend about 1.5 mag fainter in GC luminosity, below the GCLF turnover; and (b) they apply the forced linear-fit assumption to the mean points from the bimodal fits, which I have argued against above. The blue GC sequence is found to have a significant slope (MMR) for the three bins containing the large ellipticals, but no significant slope is found for the GCs in the dwarf ellipticals. In all cases the red GC sequence is indistinguishable from vertical. Referring particularly to their Figure 2 where the mean points are plotted, I note that the significance of the blue MMR slope will be very much reduced if the brightest two points ( $M_z < -10$ , close to the  $10^6 M_\odot$  level) are excluded and only the fainter bins are used. The strongest case in their data for a nonzero MMR slope is from the combined GC sample

for the three brightest giants, M87, M49, and M60 (their Fig. 2a), though even there the blue sequence becomes essentially vertical for  $M_z > -9$ .

Additional tests for any biases and internal uncertainties in the fitting procedures can be carried out through simulated CMDs (see, e.g. Mieske et al. 2006; Waters et al. 2009, for recent examples). Figure 29 shows one illustration of a model CMD tuned to the present ( $B - I$ ) data, in which the total numbers of GCs and contaminating field objects are closely similar to the real data for the six BCGs combined. Here, the simulated blue sequence is purely vertical with a mean color  $\langle B - I \rangle = 1.56$  and Gaussian standard deviation  $\sigma_{B-I} = 0.09$ , and follows a Gaussian luminosity function with  $\langle M_I \rangle = -8.3$ ,  $\sigma_I = 1.45$ . The red sequence is purely vertical with  $\langle B - I \rangle = 2.00$ ,  $\sigma_{B-I} = 0.15$ , and its LF follows  $\langle M_I \rangle = -8.3$ ,  $\sigma_I = 1.25$ . Field stars are added following a uniform distribution in color and a power-law increase in magnitude. All the artificial data are broadened in color by measurement scatter that increases with magnitude, and lastly have photometric completeness functions in  $B$  and  $I$  applied to them that mimic the real data. The simulated CMD in Fig.29 includes 17500 GCs, 55% of which are on the red sequence and 45% on the blue sequence. Lastly, the histograms above each CMD show that the intrinsic distributions in ( $B - I$ ) for the luminosity range below the onset of the MMR are similar. The simulated CMD clearly fails to reproduce the structure at the high-luminosity end ( $M_I \lesssim -10$ ) that we see in the real data. The most noticeable effect is that the real data do not have the very metal-poor and very luminous GCs that would lie on the direct upward extension of a vertical blue sequence. If these were actually present in the real galaxies, they would be more easily found than GCs anywhere else in the color-magnitude diagram. RMIX bimodal fits to the simulated data show no significant trend for a spurious MMR to appear, or for significant biases in the deduced sequence colors.

### 6.5. Implications for Theoretical Models

The currently published analyses that draw from large, deep, and metallicity-sensitive photometry point to an emerging consensus around the view that the MMR has a nonlinear form: the blue sequence is nearly vertical at low GC luminosities, but continuously changes to a stronger increase of metallicity with cluster mass as we go upward along the sequence. On the red sequence, however, the current data are consistent with the interpretation that it stays nearly vertical (metallicity is uncorrelated with luminosity).

These observations, if correct, already have implications for the different theoretical models based on the central concept of self-enrichment. Strader & Smith (2008) construct a model built on the assumption of a continuous linear form of the MMR, which as noted above corresponds to a scaling  $Z \sim M^p$  over the entire GC mass range. In their model this form turns out to require that the *star formation efficiency*  $f_*$  within the protocluster cloud also scales continuously with cluster mass in the same way. This particular form of a self-enrichment model is therefore ruled out by the observations, which show that the blue sequence is nearly vertical (metallicity is uncorrelated with mass) for  $M \lesssim 10^6 M_\odot$ , and that more generally the MMR is nonlinear.

In contrast, Bailin & Harris (2009) assume  $f_* = \text{const}$  with GC mass (specifically  $f_* = 0.3$ , though the precise value is not important). The important quantity that changes with cluster mass is instead the fraction of SNe-ejected gas held back in the protocluster, i.e. the heavy-element *retention efficiency*  $f_Z$  which drives the enrichment of the lower-mass stars in the protocluster. The retention  $f_Z$  is a strong nonlinear function of  $M$  (that is, the depth of the protocluster potential well). This approach leads to the prediction that the blue GC sequence should show a fairly distinct visible ‘‘onset’’ of the MMR at around one million Solar masses. The same sort of self-enrichment onset should also appear on the red GC sequence, though it would only become obvious at still higher mass because the mean pre-enrichment of the red GCs (that is, their baseline mean metallicity) is an order of magnitude higher. This theoretical form of the MMR is more in agreement with the observations.

Both these model approaches are admittedly idealized, and a synthesis of their ideas might lead to an improved match to the data. The Bailin/Harris model predicts a MMR onset that is probably too abrupt (a rapid changeover to a sloped MMR appears just at the point where the amount of internal self-enrichment becomes larger than the baseline pre-enrichment metallicity). The data here (see particularly Fig. 21) favor a smoother and more gradual change in slope over a wide mass range. Clearly the enriched-gas retention efficiency  $f_Z$  should increase with protocluster mass, but the star formation efficiency may also change systematically with increasing mass. These models also treat the protocluster in isolation. If it is placed within a surrounding lower-density gaseous region (giant molecular cloud or dwarf galaxy), then the addition of some external pressure confinement could increase the effective  $f_Z$  and extend the visible onset of the MMR more smoothly to lower masses (see the model papers for additional discussion).

### 6.6. The MMR and Cluster Size

A final stage of the MMR discussion in this paper is to ask whether the details of the mass/metallicity correlation might depend on other external factors. Two factors that can be investigated here are the *characteristic size* of the GC and its *location in the galaxy*, both of which may affect the efficiency of self-enrichment.

If the MMR itself is a *second-order* feature of the GC metallicity distribution, requiring  $\sim 10^3$  clusters to clearly reveal it, then any correlations of the MMR with other parameters are still more subtle *third-order* features that we might expect to require samples of  $\sim 10^4$  clusters or more. The database in the present paper is therefore just barely large enough to begin this kind of search. Indeed, the results to be described below are suggestive of certain trends but in the end must be considered as no more than tantalizing hints.

The slope of the MMR should in principle depend on the depth of the cluster potential well, and its effective radius helps determine that depth. That is, for a given cluster mass we might expect the self-enrichment process to be less effective for more extended GCs, which would have lower escape energies and thus be less able to hold back their early SNe ejecta. If this idea is correct, then along the blue GC sequence the clusters with the biggest radii should be systematically bluer (more metal-poor)

than those with small radii.

A first look for any such effect is shown in Figure 30, where the total sample is subdivided by  $r_h$ . The only pre-selection applied here is to restrict the list to those objects with ISHAPE  $S/N > 20$  to ensure some minimal quality in the cluster size estimate.

- As discussed above, the subsample with  $r_h < 2$  pc is likely to have the highest proportion of field contaminants of various kinds. Nevertheless, many of the objects in this range are likely to be GCs: the bimodal sequences remain well defined and their locations track the mean loci defined from the whole sample (dashed lines in the Figure).
- The objects in the range  $2 < r_h < 4$  pc make up the classic, “normal” globular clusters whose sizes fall comfortably into the baseline pattern set by the Milky Way. This part of the sample is likely to be relatively free from contamination, and defines clear bimodal sequences. They accurately follow the mean lines for the entire sample as well. Interestingly, there are relatively more *high*-luminosity clusters ( $M_I < -11$ ) in this group than in the previous one, but this is largely due to the radius/luminosity correlation discussed earlier (Fig. 17).
- The biggest objects are in the third panel of the figure. These fall in the size range  $4 < r_h < 10$  pc and would include the most extended known GCs with luminosities higher than the GCLF turnover point, except for a few still bigger UCD-like objects. One feature to note is that, at all luminosities, there are relatively fewer red-sequence clusters in this size range than at the lower sizes; this is the result of the size/metallicity correlation discussed earlier (Fig. 18). The details of the blue GC sequence are potentially more interesting, because if the predictions of the self-enrichment model are correct, we might expect to begin seeing its effects here. Indeed, these large clusters fall steadily about 0.1 mag to the blue of the mean line for the whole sample, corresponding to  $\Delta[\text{Fe}/\text{H}] \simeq -0.25$  dex in metallicity. The self-enrichment model is likely not to be the only possible explanation of this offset, but it is a tantalizing piece of evidence that at very least is consistent with the model.

A Kolmogorov-Smirnov test was used to compare the color distributions for the three groups of clusters shown in Fig. 30, restricted to the upper luminosity range  $M_I < -10.0$  where the differences appear to be most noticeable. The third group ( $r_h > 4$  pc) is systematically bluer than the first group ( $r_h < 2$  pc) with very high significance,  $> 99\%$ . The middle group ( $r_h = 2-4$  pc) is different from either of the other two at the  $\gtrsim 90\%$  level, suggestive but not conclusive.

In the third panel of Fig. 30(c), the very high luminosity range  $-11.2 > M_I > -11.8$  also shows a dozen objects that fall between the two main sequences. Two are from the NGC 3268 field, seven from NGC 7626, and three from NGC 4696, all have  $S/N > 200$ , and all have  $r_h$  values from 4 to 7 pc. Careful visual inspection on the original images shows that one of these has a comparably

bright neighbor  $0.45''$  away, not close enough to invalidate the profile fits. All the others are isolated objects with small, GC-like ellipticities and no morphological peculiarities. There is no reason to reject them from the GC sample.

### 6.7. Trends versus Galactocentric Distance

Mieske et al. (2006), in their study of the Virgo galaxy GCs, suggested that the MMR may become less noticeable at larger galactocentric distance. Such a trend might be the mark of different enrichment or formation histories at different locations in the parent galaxy’s halo. However, their data were restricted to the inner radial region  $R_{gc} \lesssim 1.5R_{eff}$  (for the bigger galaxies). The present sample covers a much bigger range in  $R_{gc}$  and thus should be able to provide a more sensitive test of any such trend. Figure 31 shows the color-magnitude diagrams in three successive radial zones divided by galactocentric distance: the inner region  $R_{gc} < R_{eff}$ , a middle zone  $R_{eff} < R_{gc} < 2R_{eff}$ , and the broad outer region  $2R_{eff} < R_{gc} \lesssim 5R_{eff}$ . These radial subdivisions leave about the same numbers of objects in each zone, so the mean red and blue sequence lines that were defined previously (the heavy dashed lines in the figure) represent essentially a straight average over all radial zones.

The correlation of MMR with  $R_{gc}$  also provides an implicit secondary test that the GC photometry is not systematically affected by the background light gradient of the galaxy. For  $R_{gc} \gtrsim R_{eff}$ , the gradient becomes low and any residual effects on the measurements will be small.

To search for clues that the MMR slope might depend on location, the RMIX bimodal fits described above were repeated separately for each zone. The results are shown in Figure 32. Here, because the sample sizes in each luminosity bin are smaller, it was not possible to obtain fully unconstrained fits to the same level of confidence for all five parameters ( $\mu_1, \mu_2, \sigma_1, \sigma_2, p_1/p_2$ ) in the high-luminosity, sparsely populated bins that are the key to the MMR slope. However, because we are looking especially for differences in the mean colors of the *blue* sequence from one zone to the next, the RMIX fits were deliberately constrained so that the mean color and standard deviation of the *red* sequence were fixed, since it is nearly vertical to begin with. The standard deviation is fixed at  $\sigma_2(\text{red}) = 0.18$  (see Table 6), and the mean color fixed at  $\mu_2(\text{red}) = 1.994$  for the inner zone, 1.979 for the middle zone, and 1.949 for the outer zone. These values were adopted to account for the shallow radial metallicity gradient in the system (discussed in the next section). In addition, to smooth the mean sequences numerically, the RMIX fits were done in  $\simeq 0.5$ -mag wide luminosity bins but stepped by  $\Delta M_I = 0.25$  mag between bins.

In Fig. 32, from bottom to top the same gradual changeover as noted previously is apparent, from a nearly vertical sequence at  $M_I \lesssim -10$  to a progressively steeper MMR at higher luminosities. The internal errorbars on each mean point also grow dramatically at higher luminosity as the sample size in each bin decreases; and for  $M_I \lesssim -11$ , the bimodal fits become rather unstable as the blue sequence overlaps more and more heavily with the red sequence and even the proportions ( $p_1, p_2$ ) in each component become quite uncertain. There is no convincing difference between the mean lines for the inner (solid

line) and middle (dashed line) zones. A more noticeable difference appears for the outer zone, which stays offset to the blue by  $\sim 0.1$  mag relative to the inner zones. Taken at face value, this means that the MMR decreases in amplitude further out in the halo.

Another test that avoids some of the problems of binning the data, is to look directly at the color distribution in  $(B - I)_0$  for the blue-sequence GCs brighter than  $M_I = -10.5$ . The fiducial dividing line between the red and blue sequences is  $(B - I)_0 = 1.8$ : the inner zone has 97 objects bluer than that boundary, the middle zone 139, and the outer zone 129. Figure 33 shows the cumulative color distributions for these bright, blue GCs. The existence of a global, weak radial gradient in mean metallicity (see next section) first requires adding  $\Delta(B - I) = 0.02$  mag to the middle zone and 0.03 mag to the outer zone before comparison with the inner zone. The color distributions becomes steadily more weighted to the bluer side at larger  $R/R_{eff}$ , particularly in the color range  $(B - I)_0 \simeq 1.6 - 1.7$  that is crucial for determining the MMR. However, a normal Kolmogorov-Smirnov two-sample test shows that none of the zones are different from any of the others at higher than 70% significance. This is not sufficient to demonstrate any radial change in the MMR convincingly and is left only as another tantalizing hint.

A tentative conclusion from these tests is that (a) the MMR exists at all the galactocentric distance zones that the present data are capable of exploring; but that (b) there is *very weak* evidence that the MMR becomes gradually less noticeable at larger galactocentric distance. The direction of this effect is the same as found by Mieske et al. (2006) (see their Table 2 and section 4.2 discussion). Bigger samples of high-luminosity clusters from other galaxies will be needed to probe this effect conclusively.

Bailin & Harris (2009) suggest two effects that might end up producing a radial gradient in the MMR. One of these would be relevant in large galaxies that hosted active galactic nuclei (AGN's) at an early stage in their evolution: the AGN would dramatically increase the external ultraviolet radiation field and, possibly, inhibit the self-enrichment process within a protoglobular cluster of a given mass. Taken at face value, this model would predict that the MMR should be stronger at larger galactocentric distance farther from the AGN, which is opposite to what we observe. However, there is no guarantee that the timing of GC formation would automatically overlap with the appearance of the central AGN. The UV radiation field might even produce the opposite gradient if, for example, the inner GCs had already finished forming by the time the AGN reached its peak luminosity but the outer GCs had not.

The second possible effect is related to the difference between the *initial* masses of the GCs (which determine their degree of self-enrichment) and their *present-day* masses, which are smaller because of mass loss due to early SNe ejecta, stellar winds, and the slower processes of tidal stripping and evaporation of stars over  $10^{10}$  y. The inner GCs should have been subjected to a higher degree of dynamical mass loss due to tidal stripping than the outer GCs over their lifetimes, so an inner-halo GC that has the same mass *now* as an outer-halo one would have started out at higher mass and thus have been able

to self-enrich more. Testing this idea more quantitatively and finding out specifically how it affects the final MMR will require knowing, at a minimum, the average amount of GC mass loss from the protocluster stage onward, as a function of both  $M_{GC}(init)$  and  $R_{gc}$ . This direction may prove to be a rich area for detailed modelling.

Another GC phenomenon that may be linked to these arguments is the long-standing puzzle that the GC luminosity (or mass) function is nearly independent of galactocentric distance  $r$ . If the initial GCMF were nearly the same throughout the early galactic halo, then the strong dependence of dynamical evolution time on  $r$  should build in a present-day GCMF whose low-mass end and “turnover point” depend on  $r$ . A recent discussion by McLaughlin & Fall (2008) shows that the observed shape of the GCMF can be explained if its initial shape depends appropriately on the characteristic cluster density  $\rho_h$ , because the mass loss rates increase with  $\rho$ . The fact that the outer clusters have lower average densities would also go along with less self-enrichment and a weaker MMR at larger distances from the galactic center.

## 7. METALLICITY GRADIENTS

Careful inspection of the mean positions of the near-vertical sections of both blue and red sequence lines shows that at larger radius, the mean color of each sequence shifts slightly to the blue compared with the loci at smaller radii. That is, both types of GCs appear to show a metallicity gradient. It has long been realized that the GCS in a normal large galaxy taken *as a whole* (that is, combining all types of clusters) shows a negative metallicity gradient, but the majority of the effect is created simply by the decreasing ratio of red versus blue GCs with increasing galactocentric distance (Geisler et al. 1996; Harris et al. 1998; Dirsch et al. 2003; Rhode & Zepf 2004; Harris et al. 2006). That is, the steeper spatial distribution of the red, metal-rich clusters produces a *population* gradient, which has the byproduct of an overall metallicity gradient. In Harris et al. (2006) we discussed the population gradients in the BCGs studied here. By contrast, much less published material exists that is directed at finding any true metallicity gradient *within* each of the two types of clusters, and indeed any such gradients are subtle.

A large body of literature exists for abundance gradients in the integrated light of large galaxies, measured from line-strength indices. These studies are usually based on data from the high-surface-brightness region within  $1R_{eff}$  of the galaxy center (see Fisher et al. 1995; Kobayashi & Arimoto 1999; Mehlert et al. 2003; Sanchez-Blanquez et al. 2006, for a sampling of such studies, along with extensive guides to the literature). The analyses typically show that heavy-element abundance within this bulge light scales with projected galactocentric distance as anywhere from  $Z \sim R^{-0.15}$  to  $R^{-0.4}$ , favoring interpretations in which the central regions of these galaxies formed by a combination of dissipative collapse (favoring steep gradients) and subsequent mergers (favoring flatter gradients). The results are rather strongly model-dependent in the sense that each line index must be transformed to some tracer of heavy-element abundance.

Globular clusters can provide valuable extensions to these integrated-light measurements. GCs are easy to



measure at radii well beyond  $R_{eff}$ , and transformation of their colors to metallicities is based directly on calibration from the Milky Way clusters. These transformations need only the reasonable assumption that the GCs are “old” ( $\gtrsim 10$  Gyr) and thus in the regime where the colors are quite insensitive to minor age differences. The only practical issue is that a large statistical sample of GCs, over a large radial range, is needed to measure the metallicity gradient accurately. A large radial range, and large sample size, are precisely the advantages of the database in the present study.

Figure 34 shows the intrinsic colors  $(B-I)_0$  of the GCs in all six galaxies plotted directly against galactocentric distance, again normalized to  $R_{eff}$  for each one. For this purpose the sample is restricted to the brighter objects ( $M_I < -9$ ) with positive size measurements ( $r_h > 0$ ), to minimize the effects of field contamination. As above, the dividing line between blue and red GCs is defined as  $(B-I)_0 = 1.80$  and we then solve directly for the best-fitting relation for mean color versus radius within each group, in the conventional form  $\langle B-I \rangle_0 = a + b \log(R/R_{eff})$ .

Table 7 lists the solutions for the individual galaxies, along with the solutions for the combined sample. The slopes  $b$  in all cases are shallow, and essentially equal for both the red and blue components. In addition, they are not significantly different between individual galaxies, so to gain statistical weight, we can combine all of them into a single solution. The combined sample yields a nonzero signal for the slopes at the  $> 4.5 - \sigma$  level for both types of clusters, and therefore the existence of a metallicity gradient appears to be convincingly real. Given the conversion ratio  $\Delta(B-I) = 0.375 \Delta[\text{Fe}/\text{H}]$  (see above), both of the gradients convert to a heavy-element abundance scaling  $Z_{GC} \sim R^{-0.10 \pm 0.022}$ .

The slope  $\Delta \log Z / \Delta \log R = -0.10$  is shallower than is conventionally found in the integrated-light studies (see the references cited above), but it is also dominated by more distant regions of the halo,  $R > R_{eff}$ . Few other GCS studies exist for which direct comparisons can be made. Geisler et al. (1996), in their wide-field study of the GCS around the Virgo giant NGC 4472, found slopes of  $Z \sim R^{-0.15 \pm 0.03}$  for the blue GCs and  $Z \sim R^{-0.12 \pm 0.06}$  for the red GCs, out to a limiting radius of  $\sim 5R_{eff}$ . These are clearly similar to the results here. Geisler et al. also point out that the gradient for the red GCs closely matches the color gradient for the integrated halo *light* of the host galaxy; and direct evidence from halo-star studies in giant ellipticals (e.g. Harris & Harris 2002; Rejkuba et al. 2005) shows that the field-star population is dominated by the metal-richer stars whose MDF matches that of the red GCs (see also Forte et al. 2005, 2007). Forte et al. (2001) determined the gradient for the blue GCs in two Fornax ellipticals, NGC 1399 and 1427, finding  $Z(\text{blue}) \sim R^{-0.2}$  for both systems. Their data extended to  $12R_{eff}$  for NGC 1399 and  $10R_{eff}$  for NGC 1427. Recently, Lee et al. (2008) have found shallow but significant  $(C-T_1)$  color gradients in both the blue and red GCs in the Virgo giant M60 that are quite similar to those for M49. Lastly, in M31, Perrett et al. (2002) and Fan et al. (2008) find that the metal-poor GCs exhibit a metallicity gradient out to 20 kpc (or about  $4R_{eff}$ ) but suggest that the metal-rich GCs show no gradient.

Perhaps the earliest modern investigation of this ques-

tion is by Zinn (1985) for the Milky Way itself. He found that the inner, metal-poor GCs were significantly more enriched than the outer-halo ones. Using contemporary metallicity data for 105 metal-poor clusters with  $[\text{Fe}/\text{H}] < -0.95$  (with data taken from the 2003 edition of Harris 1996), I find a best-fit solution  $\langle \text{Fe}/\text{H} \rangle = (-1.446 \pm 0.063) - (0.165 \pm 0.062) \log r_{gc}$  where  $r_{gc}$  is the true three-dimensional distance from the Galactic center. This GC sample extends out to more than 100 kpc from the Galactic center. A solution in which the same data are artificially projected onto two dimensions (making them directly comparable with the other galaxies above) gives  $\langle \text{Fe}/\text{H} \rangle = (-1.490 \pm 0.047) - (0.146 \pm 0.051) \log R_{gc}$ . In this case the 3D slope is already so shallow that projection into two dimensions does not decrease it much.

The available data sketch out a consistent pattern whereby both the metal-poor and metal-rich globular cluster subsystems have shallow but real radial metallicity gradients, in the range  $Z \sim R^{-(0.1-0.2)}$ . Particularly in the large spiral galaxies, the gradients for the metal-rich clusters are harder to determine because they are less numerous and spatially more centrally concentrated, but for the metal-poor clusters the Milky Way scaling of  $Z \sim R^{-0.15 \pm 0.05}$  is typical of the mean for all the galaxies. The most internally precise value for any of the systems is the one determined here ( $b = -0.10 \pm 0.022$ ) for the six BCGs.

Interpretation of these metallicity gradients in terms of the past history of the parent galaxy is an intriguing and incompletely explored area. Major mergers can produce extensive spatial mixing and reduce any pre-existing steep metallicity gradient that was the result of dissipative early star formation in the progenitors. Gas-rich mergers will produce a new population of stars and clusters especially in the inner regions and may thus help rebuild the gradient, at least for the *metal-rich* component. However, two intriguing features of the observational evidence so far are that (a) the gradient slope  $b \simeq -(0.1 - 0.2)$  appears to be very much the same for both giant elliptical and spiral galaxies, and (b) it is also the same for the metal-rich and metal-poor clusters, even though they may have experienced very different histories as well as formation times. More extensive N-body simulations of mergers specially tuned to trace metallicity gradients well outward into the halo will be needed to constrain the range of possibilities and help decide how much of the gradients we observe now are relics of the primordial conditions of formation.

## 8. SUMMARY

In this study the globular cluster populations in six giant elliptical galaxies have been investigated through their distributions in size, metallicity, and luminosity. A total of about 15000 objects, of which about  $\sim 8000$  are high-probability globular clusters belonging to these six galaxies, have been measured down to a luminosity  $M_I \simeq -8$ , slightly fainter than the turnover point of the standard GC luminosity function. Particular emphasis is given to characterizing the relation between GC mass and metallicity (the MMR) that becomes most noticeable for the blue, metal-poor cluster population at high luminosity. A summary of the findings in this study can be made as follows:

1. The target galaxies in this study are at typical distances  $d \sim 40$  Mpc and at these distances, their globular clusters can be barely resolved as non-stellar with our HST/ACS imaging data. Analytic King-model fits convolved with the stellar point-spread function have been used successfully to determine total magnitudes, colors, and effective (half-light) radii for each detectable object.
2. The new photometry of the clusters based on individually size-corrected total magnitudes is more accurate than the previous data based either on PSF-fitting or fixed-aperture photometry (Harris et al. 2006), but it does not lead to substantial changes in the color-magnitude distribution. The GCs accurately define the classic bimodal red and blue components at all luminosities, with the blue component at  $\langle B - I \rangle_0 = 1.6$  and the red component at  $\langle B - I \rangle_0 = 2.0$ .
3. The distribution in intrinsic GC scale size in these giant ellipticals accurately matches that of the Milky Way clusters, with a peak frequency near  $r_h \simeq 2$  pc and an extended tail of larger objects. Field contamination of the total sample consists mostly of very faint or starlike objects that can be objectively culled out of the GC data.
4. The range of intrinsic  $r_h$  sizes is large for all types of clusters, metal-poor and metal-rich alike. However, the blue, lower-metallicity GCs are systematically larger on average than the red, higher-metallicity ones by about 17%. This difference is statistically highly significant, and holds up at all GC luminosities and all galactocentric distances. These results suggest that the correlation between cluster scale size and metallicity is intrinsic to the clusters, a result of their formation or later internal dynamical evolution, rather than reaction to the external tidal field.
5. The median cluster sizes, of both types, also scale with projected galactocentric distance as  $r_h \sim R_{gc}^{0.11}$ . The data extend outward to approximately  $5R_{eff}$  into the halos of the galaxies, and thus probe more extended regions of the halos than do most previous studies. These results fit in well with data from other galaxies indicating that clusters forming in shallower, less extreme tidal fields end up with larger characteristic sizes.
6. The median scale size of the clusters also depends weakly and nonlinearly on cluster luminosity, in the sense that GCs more luminous than  $M_I \lesssim -11$  become progressively bigger. The effective radii of the very most luminous clusters known are almost twice as large as the bulk of the clusters at  $M_I > -11$ . Most of these luminous GCs, however, are smaller than UCDs of the same luminosity.
7. The blue GC sequence exhibits a clear mass/metallicity relation (MMR), but it is not linear in color versus magnitude. Its shape is rather that of a gradual changeover from nearly vertical (for the lower-luminosity range  $M_I \gtrsim -9.5$ ) to a steeper slope at higher luminosity. The uppermost luminosity range corresponds to a heavy-element scaling with cluster mass of  $Z \sim M^{0.5}$ .
8. The red GC sequence is nearly vertical at all luminosities.
9. The shape of the MMR for both the blue and red sequences is consistent with the basic interpretation that it is due to cluster self-enrichment during their formation epoch. Though theoretical models of this type are still in early stages, the data rule out models in which the star formation efficiency  $f_*$  within a protocluster scales strongly with cluster mass. Instead, models in which  $f_* \sim const$  and the heavy-element retention efficiency  $f_Z$  increases with cluster mass produce a more realistic match to the observations.
10. The slope of the MMR along the blue sequence does not depend strongly on cluster size  $r_h$ . The data contain a hint that the biggest GCs ( $r_h > 4$  pc) follow a slightly bluer sequence at the high-luminosity end. If so, it would be consistent with the idea that self-enrichment was less effective (for a given GC mass) in more extended clusters with shallower potential wells.
11. The data from these giant elliptical galaxies also show that the MMR depends weakly, if at all, on projected galactocentric distance. If a trend exists, it is in the sense that the MMR has lower amplitude at larger  $R_{gc}$ ; this may indicate that the inner GCs have lost more mass than the outer ones due to tidal stripping and dynamical evolution, so that they have a larger contrast between their initial masses (which determine the amount of self-enrichment) and their present-day masses (which we directly observe).
12. Both the red and blue GC subsystems exhibit shallow metallicity gradients: they become systematically more metal-poor at larger galactocentric distance. The gradients in both cases scale as  $Z \sim R_{gc}^{-0.10 \pm 0.022}$  and, though small, are clearly measurable in this large dataset. These results agree well with the limited data available for other elliptical and spiral galaxies, and are likely to point to a combination of the amount of initial enrichment plus later merging histories.

## 9. FINAL CAVEATS

Phenomena such as the MMR, the GC size distributions, and the metallicity gradients within the components of the globular cluster systems, have the potential to provide rich grounds for modelling and interpretation, but are still imperfectly understood. All the attempts to date to describe what is happening at the high-mass end of the globular cluster distribution continue to be data-limited. Even in the present study, only a few hundred GCs brighter than  $M_I = -10.5$  ( $10^6 M_\odot$ ) are available to work with, and these are spread over several individual galaxies within which the conditions of formation could have differed. Breaking down that part of the sample

further by metallicity, luminosity, or galactocentric distance then leads us quickly into a shadowy zone where conclusions are tentative.

On strictly observational grounds, the correlation between GC color and luminosity called the MMR continues to be a difficult effect to measure, and should still be considered as incompletely established. Even the data discussed here are not yet enough to address important questions such as whether or not the MMR may differ in amplitude from galaxy to galaxy, or if it is genuinely absent in some galaxies. Careful attempts have been made here to reduce or eliminate several worries in previous studies, including small sample size; systematic errors in PSF-fitting or fixed-aperture photometry due to differing cluster sizes; low signal-to-noise; and background light gradients. If the present data still hide systematic errors, they must be due to some subtle and ill-understood features of the image preprocessing or measurement algorithms that would preferentially affect the photometry of the brightest objects instead of the faintest ones, and the blue GCs rather than the only-slightly-redder ones. In the longer term, probably the best security against such systematics will be to carry out more GCS studies with different telescopes and cameras, still larger samples, and especially metallicity-sensitive color indices. Some comparative work of this type is already in the literature, but there are still only a few large galaxies in which the MMR can be described as plainly visible.

On theoretical grounds, the central concept of self-enrichment is an attractive one, but its most important assumption is that it requires the main star for-

mation period in a proto-GC to last long enough for the most massive stars to form, evolve, and eject their enriched material before most of the low-mass stars have finished forming themselves. The often-used arbitrary assumption of an “instantaneous starburst” cannot be correct in real star-forming regions, but for this model to work, the star formation period needs to stretch over at least 10 Myr and perhaps as long as 20 – 30 Myr (see Bailin & Harris 2009). Contemporary observations of dense, massive star-forming regions point encouragingly in that direction, but are not yet definitive. If the average formation time in the most massive GCs is as short as  $\sim 5$  Myr, for example, then the self-enrichment model would be in serious trouble.

Many other giant and supergiant ellipticals whose globular cluster systems have not yet been studied are well within reach of the HST and large ground-based telescopes. These hold out obvious prospects for increasing the GCS sample sizes further by large factors. Major strides can be made towards understanding this intriguing correlation further.

This work was supported by the Natural Sciences and Engineering Research Council of Canada through research grants to WEH, and by the Killam Foundation of the Canada Council through a research fellowship. Many thanks to Søren Larsen, who provided advice about the ISHAPE code and implemented several detailed improvements to the code that helped this work. I am grateful to Gretchen Harris for a close reading of the manuscript.

## REFERENCES

- Aarseth, S.J., & Heggie, D.C. 1998, MNRAS, 297, 794  
 Bailin, J., & Harris, W.E. 2009, ApJ, in press (arXiv:0901:2302)  
 Barmby, P., McLaughlin, D.E., Harris, W.E., Harris, G.L.H., & Forbes, D.A. 2007, AJ, 133, 2764  
 Baumgardt, H., Hut, P., & Heggie, D.C. 2002, MNRAS, 336, 1069  
 Bertin, E., & Arnouts, S. 1996, A&AS, 117, 393  
 Blakeslee, J.P. 1999, AJ, 118, 1506  
 Cantiello, M., Blakeslee, J.P., & Raimondo, G. 2007, ApJ, 668, 209  
 Cockcroft, R., Harris, W.E., Wehner, E.M.H., Whitmore, B.C., & Rothberg, B. 2009, AJ, paper submitted  
 DeGraaff, R.B., Blakeslee, J.P., Meurer, G.R., & Putman, M. 2007, ApJ, 671, 1624  
 Dirsch, B., Richtler, R., Geisler, D., Forte, J.C., Bassino, L.P., & Gieren, W.P. 2003, AJ, 125, 1908  
 Evstigneeva, E.A., Drinkwater, M.J., Peng, C.Y., Hilker, M., DePropriis, R., Jones, J.B., Phillips, S., Gregg, M.D., & Karick, A.M. 2007, AJ, 136, 461  
 Evstigneeva, E.A., Gregg, M.D., Drinkwater, M.J., & Hilker, M. 2007, AJ, 133, 1722  
 Fan, Z., Ma, J., de Grijs, R., & Zhou, X. 2008, MNRAS, 385, 1973  
 Fisher, D., Franx, M., & Illingworth, G. 1995, ApJ, 448, 119  
 Forte, J.C., Faifer, F., & Geisler, D. 2005, MNRAS, 357, 56  
 Forte, J.C., Faifer, F., & Geisler, D. 2007, MNRAS, 382, 1947  
 Forte, J.C., Geisler, D., Ostrov, P.G., Piatti, A.E., & Gieren, W. 2001, AJ, 121, 1992  
 Geisler, D., Lee, M.G., & Kim, E. 1996, AJ, 111, 1529  
 Georgiev, I.Y., Goudfrooij, P., Puzia, T.H., & Hilker, M. 2008, AJ, 135, 1858  
 Georgiev, I.Y., Puzia, T.H., Hilker, M., & Goudfrooij, P. 2009, MNRAS, 392, 879  
 Gómez, M., & Woodley, L.A. 2007, ApJ, 670, L105  
 Harris, W.E. 1996, AJ, 112, 1487  
 Harris, W.E. 2001, in *Star Clusters*, Saas-Fee Advanced Course 28 (New York: Springer), ed. L. Labhardt & B. Binggeli  
 Harris, W.E. & Harris, G.L.H. 2002, AJ, 123, 3108  
 Harris, W.E., Harris, G.L.H., Holland, S.T., & McLaughlin, D.E. 2002, AJ, 124, 1435  
 Harris, W.E., Harris, G.L.H., & McLaughlin, D.E. 1998, AJ, 115, 1801  
 Harris, W.E., Pritchett, C.J., & McClure, R.D. 1995, ApJ, 441, 120  
 Harris, W.E., Whitmore, B.C., Karakla, D., Okon, W., Baum, W.A., Hanes, D.A., & Kavelaars, J.J. 2006, ApJ, 636, 90  
 Harris, W.E., Kavelaars, J.J., Hanes, D.A., Pritchett, C.J., & Baum, W.A. 2009, AJ, 137, 3314  
 Hasegan, M. et al. 2005, ApJ, 627, 203  
 Jordán, A. 2004, ApJ, 613, L117  
 Jordán, A. et al. 2005, ApJ, 634, 1002  
 King, I. 1962, AJ, 67, 471  
 Kobayashi, C., & Arimoto, N. 1999, ApJ, 527, 573  
 Kundu, A. 2008, AJ, 136, 1013  
 Kundu, A., & Whitmore, B.C. 1998, AJ, 116, 2841  
 Kundu, A., Whitmore, B.C., Sparks, W.B., Macchetto, F.D., Zepf, S.E., & Ashman, K.M. 1999, ApJ, 513, 733  
 Kundu, A., & Zepf, S.E. 2007, ApJ, 660, L109  
 Larsen, S.S. 1999, A&AS, 139, 393  
 Larsen, S.S., & Brodie, J.P. 2003, ApJ, 593, 340  
 Larsen, S.S., Brodie, J.P., Huchra, J.P., Forbes, D.A., & Grillmair, C.J. 2001, AJ, 121, 2974  
 Lee, M.G., Kim, E., Hwang, H.S., Kim, S.C., & Geisler, D. 2008, ApJ, 682, 135  
 MacDonald, P.D.M. 2007, documentation and code at <http://www.math.mcmaster.ca/peter/mix/mix.html>, Department of Mathematics and Statistics, McMaster University  
 McLaughlin, D.E. 2000, ApJ, 539, 618  
 McLaughlin, D.E., Barmby, P., Harris, W.E., Forbes, D.A., & Harris, G.L.H. 2008, MNRAS, 384, 563  
 McLaughlin, D.E., & Fall, S.M. 2008, ApJ, 679, 1272  
 Mehlert, D., Thomas, D., Saglia, R.P., Bender, R., & Wegner, G. 2003, A&A, 407, 423  
 Mieske, S. et al. 2006, ApJ, 653, 193 A&A, 410, 445  
 Ostrov, P.G., Forte, J.C., & Geisler, D. 1998, AJ, 116, 2854  
 Peng, E.W. et al., 2006, ApJ, 639, 95  
 Peng, E.W. et al., 2008, ApJ, 681, 197  
 Perrett, K.M., Bridges, T.J., Hanes, D.A., Irwin, M.J., Brodie, J.P., Carter, D., Huchra, J.P., & Watson, F.G. 2002, AJ, 123, 2490  
 Rejkuba, M., Greggio, L., Harris, W.E., Harris, G.L.H., & Peng, E.W. 2005, ApJ, 631, 262  
 Rhode, K.L., & Zepf, S.E. 2004, AJ, 127, 302  
 Sanchez-Blanchuez, P., Gorgas, J., & Cardiel, N. 2006, A&A, 457, 823

- Spitler, L.R., Forbes, D.A., & Beasley, M.A. 2008, MNRAS, 389, 1150
- Spitler, L.R., Larsen, S.S., Strader, J., Brodie, J.P., Forbes, D.A., & Beasley, M.A. 2006, AJ, 132, 1593
- Spitzer, L., & Thuan, T.X. 1972, ApJ, 175, 31
- Stetson, P.B. 1987, PASP, 99, 191
- Strader, J., Brodie, J.P., Spitler, L., & Beasley, M.A. 2006, AJ, 132, 2333
- Strader, J., & Smith, G.H. 2008, AJ, 136, 1828
- Strader, J., Beasley, M.A., & Brodie, J.P. 2007, AJ, 133, 2015
- Trenti, M., Heggie, D.C., & Hut, P. 2007, MNRAS, 374, 344
- van den Bergh, S., Morbey, C., & Pazder, J. 1991, ApJ, 375, 594
- Waters, C.Z., Zepf, S.E., Lauer, T.R., & Baltz, E.A. 2009, ApJ, 693, 463
- Wehner, E.M.H., Harris, W.E., Whitmore, B.C., Rothberg, B., & Woodley, K.A. 2008, ApJ, 681, 1233
- Zepf, S.E., & Ashman, K.M. 1993, MNRAS, 264, 611
- Zinn, R. 1985, ApJ, 293, 424

TABLE 1  
 BRIGHTEST CLUSTER GALAXIES IMAGED WITH THE ACS

Galaxy	Cluster or Group	Redshift (km s <sup>-1</sup> )	$M_V^T$	$E(B-I)$	$(m-M)_I$ ( $M_I < -8.4$ )	$R_{eff}$ (arcmin)	$B, I$ Exposures (sec)
NGC 1407	Eridanus	1627	-22.35	0.16	31.96	1.17'	2 × 750, 2 × 340
NGC 3348	CfA 69	2837	-22.13	0.17	33.18	0.44'	6 × 1200, 4 × 530
NGC 3258	Antlia	3129	-21.87	0.20	33.23	0.50'	4 × 1340, 4 × 570
NGC 3268	Antlia	3084	-21.96	0.24	33.27	0.60'	4 × 1340, 4 × 570
NGC 4696	Cen30	2926	-23.31	0.23	33.29	0.74'	4 × 1360, 4 × 580
NGC 7626	Pegasus I	3405	-22.35	0.17	33.57	0.64'	6 × 1310, 2 × 1300

 TABLE 2  
 CHARACTERISTICS OF THE POINT-SPREAD FUNCTIONS

Galaxy	FWHM( $B$ )	$N_*(B)$	FWHM( $I$ )	$N_*(I)$
NGC 1407	0.091''	10	0.090''	5
NGC 3348	0.081''	8	0.089''	10
NGC 3258	0.098''	6	0.091''	18
NGC 3268	0.096''	8	0.084''	15
NGC 4696	0.102''	25	0.095''	52
NGC 7626	0.102''	6	0.096''	11
Mean	0.095'' ±0.0033''	10	0.091'' ±0.0018''	19

 TABLE 3  
 MEDIAN SIZES OF GLOBULAR CLUSTERS VERSUS LUMINOSITY

$M_I$ Range	$n(blue)$	$\langle r_h \rangle(blue)$ (pc)	$n(red)$	$\langle r_h \rangle(red)$ (pc)
(-12.0, -12.7)	10	4.63	15	3.86
(-11.5, -12.0)	17	2.21	32	2.85
(-11.0, -11.5)	105	3.10	81	2.63
(-10.5, -11.0)	186	2.80	150	2.36
(-10.0, -10.5)	301	2.65	263	2.21
(-9.5, -10.0)	419	2.51	313	2.21
(-9.0, -9.5)	289	2.80	139	2.65
Milky Way	48	3.06	18	2.40

 TABLE 4  
 MEDIAN SIZES OF GLOBULAR CLUSTERS VERSUS  $R_{GC}$ 

$R_{GC}/R_{eff}$	$n(blue)$	$\langle r_h \rangle(blue)$ (pc)	$n(red)$	$\langle r_h \rangle(red)$ (pc)
(0.0 - 0.5)	50	2.28	56	1.95
(0.5 - 1.0)	193	2.51	185	2.06
(1.0 - 1.5)	232	2.50	175	2.06
(1.5 - 2.0)	227	2.36	161	2.18
(2.0 - 2.5)	221	2.63	141	2.36
(2.5 - 3.0)	159	2.95	127	2.33
(3.0 - 3.5)	119	2.95	55	2.36
(3.5 - 4.0)	56	2.95	32	2.58
(4.0 - 5.0)	37	3.15	31	2.77

TABLE 5  
RMIX BIMODAL FITS TO THE INDIVIDUAL GALAXIES

$I$ range	$N(\text{bin})$	$\mu_1$	$\sigma_1$	$\mu_2$	$\sigma_2$	$p_1$
NGC 1407						
21.0 – 22.0	113	$1.885 \pm 0.058$	$0.102 \pm 0.033$	$2.201 \pm 0.055$	$0.120 \pm 0.033$	0.413
22.0 – 23.0	287	$1.789 \pm 0.023$	$0.123 \pm 0.017$	$2.225 \pm 0.015$	$0.121 \pm 0.011$	0.367
23.0 – 23.5	219	$1.743 \pm 0.018$	$0.078 \pm 0.016$	$2.177 \pm 0.020$	$0.159 \pm 0.016$	0.298
23.5 – 24.0	216	$1.733 \pm 0.109$	$0.109 \pm 0.018$	$2.191 \pm 0.016$	$0.158 \pm 0.015$	0.331
NGC 3348						
21.0 – 23.0	96	$1.864 \pm 0.061$	$0.142 \pm 0.035$	$2.157 \pm 0.060$	$0.104 \pm 0.031$	0.663
23.0 – 24.0	214	$1.640 \pm 0.012$	$0.074 \pm 0.011$	$2.085 \pm 0.015$	$0.148 \pm 0.012$	0.318
24.0 – 25.0	348	$1.642 \pm 0.011$	$0.078 \pm 0.010$	$2.085 \pm 0.015$	$0.165 \pm 0.012$	0.313
NGC 3258						
21.0 – 22.5	91	$1.836 \pm 0.032$	$0.097 \pm 0.021$	$2.130 \pm 0.059$	$0.112 \pm 0.035$	0.614
22.5 – 23.0	113	$1.738 \pm 0.024$	$0.063 \pm 0.022$	$1.997 \pm 0.039$	$0.176 \pm 0.020$	0.267
23.0 – 23.5	197	$1.778 \pm 0.025$	$0.090 \pm 0.017$	$1.133 \pm 0.037$	$0.134 \pm 0.025$	0.483
23.5 – 24.0	279	$1.753 \pm 0.013$	$0.085 \pm 0.009$	$2.132 \pm 0.025$	$0.137 \pm 0.019$	0.534
24.0 – 24.5	370	$1.740 \pm 0.009$	$0.090 \pm 0.007$	$2.168 \pm 0.020$	$0.137 \pm 0.013$	0.550
24.5 – 25.0	402	$1.740 \pm 0.010$	$0.097 \pm 0.008$	$2.146 \pm 0.015$	$0.131 \pm 0.012$	0.513
NGC 3268						
21.0 – 22.5	84	$1.815 \pm 0.017$	$0.026 \pm 0.018$	$2.050 \pm 0.023$	$0.154 \pm 0.015$	0.128
22.5 – 23.0	101	$1.799 \pm 0.019$	$0.030 \pm 0.066$	$2.050 \pm 0.046$	$0.170 \pm 0.028$	0.107
23.0 – 23.5	162	$1.759 \pm 0.014$	$0.045 \pm 0.013$	$2.097 \pm 0.022$	$0.198 \pm 0.015$	0.156
23.5 – 24.0	249	$1.768 \pm 0.010$	$0.081 \pm 0.008$	$2.187 \pm 0.019$	$0.152 \pm 0.015$	0.471
24.0 – 24.5	334	$1.878 \pm 0.014$	$0.096 \pm 0.010$	$2.183 \pm 0.024$	$0.165 \pm 0.018$	0.449
24.5 – 25.0	377	$1.768 \pm 0.015$	$0.108 \pm 0.011$	$2.197 \pm 0.024$	$0.163 \pm 0.017$	0.477
NGC 4696						
21.0 – 22.5	127	$1.907 \pm 0.018$	$0.100 \pm 0.000$	$2.223 \pm 0.030$	$0.150 \pm 0.000$	0.517
22.5 – 23.0	192	$1.901 \pm 0.046$	$0.084 \pm 0.027$	$2.170 \pm 0.065$	$0.141 \pm 0.031$	0.378
23.0 – 23.5	297	$1.846 \pm 0.010$	$0.074 \pm 0.008$	$2.220 \pm 0.018$	$0.152 \pm 0.014$	0.389
23.5 – 24.0	374	$1.814 \pm 0.009$	$0.081 \pm 0.007$	$2.234 \pm 0.015$	$0.153 \pm 0.012$	0.441
24.0 – 24.5	636	$1.812 \pm 0.010$	$0.091 \pm 0.007$	$2.213 \pm 0.019$	$0.174 \pm 0.013$	0.445
24.5 – 25.0	658	$1.847 \pm 0.012$	$0.123 \pm 0.008$	$2.278 \pm 0.023$	$0.156 \pm 0.016$	0.589
25.0 – 25.5	516	$1.801 \pm 0.026$	$0.122 \pm 0.022$	$2.149 \pm 0.053$	$0.234 \pm 0.026$	0.319
NGC 7626						
21.0 – 22.5	76	$1.832 \pm 0.049$	$0.100 \pm 0.000$	$2.116 \pm 0.030$	$0.150 \pm 0.000$	0.194
22.5 – 23.5	218	$1.808 \pm 0.018$	$0.106 \pm 0.012$	$2.203 \pm 0.020$	$0.137 \pm 0.015$	0.437
23.5 – 24.0	228	$1.801 \pm 0.023$	$0.120 \pm 0.017$	$2.219 \pm 0.025$	$0.132 \pm 0.017$	0.494
24.0 – 24.5	323	$1.728 \pm 0.010$	$0.074 \pm 0.007$	$2.158 \pm 0.015$	$0.160 \pm 0.012$	0.344
24.5 – 25.0	385	$1.752 \pm 0.020$	$0.112 \pm 0.014$	$2.184 \pm 0.028$	$0.173 \pm 0.019$	0.426
25.0 – 25.5	375	$1.741 \pm 0.024$	$0.115 \pm 0.017$	$2.182 \pm 0.037$	$0.180 \pm 0.024$	0.464

TABLE 6  
 RMIX BIMODAL FITS TO THE COMBINED SAMPLE

$M_I$ range	$N(\text{bin})$	$\mu_1$	$\sigma_1$	$\mu_2$	$\sigma_2$	$p_1$
(-12.7, -11.5)	285	$1.757 \pm 0.038$	$0.102 \pm 0.032$	$1.944 \pm 0.029$	$0.209 \pm 0.013$	$0.181 \pm 0.109$
(-11.5, -11.0)	359	$1.642 \pm 0.017$	$0.100 \pm 0.000$	$1.902 \pm 0.019$	$0.180 \pm 0.000$	$0.286 \pm 0.057$
(-11.0, -10.5)	627	$1.669 \pm 0.031$	$0.121 \pm 0.016$	$1.991 \pm 0.043$	$0.140 \pm 0.020$	$0.531 \pm 0.114$
(-10.5, -10.0)	1039	$1.595 \pm 0.014$	$0.098 \pm 0.009$	$1.956 \pm 0.020$	$0.176 \pm 0.012$	$0.345 \pm 0.048$
(-10.0, -9.5)	1448	$1.590 \pm 0.008$	$0.107 \pm 0.005$	$2.012 \pm 0.009$	$0.146 \pm 0.006$	$0.439 \pm 0.021$
(-9.5, -9.0)	2022	$1.555 \pm 0.005$	$0.091 \pm 0.004$	$1.985 \pm 0.008$	$0.164 \pm 0.006$	$0.414 \pm 0.017$
(-9.0, -8.5)	2526	$1.570 \pm 0.006$	$0.108 \pm 0.005$	$1.993 \pm 0.010$	$0.165 \pm 0.006$	$0.438 \pm 0.020$
(-8.5, -8.0)	2333	$1.554 \pm 0.009$	$0.113 \pm 0.006$	$1.981 \pm 0.013$	$0.170 \pm 0.008$	$0.445 \pm 0.027$
(-12.4, -10.4)	848	$1.672 \pm 0.008$	$0.119 \pm 0.006$	$1.970 \pm 0.008$	$0.184 \pm 0.007$	$0.400 \pm 0.011$
(-10.4, -8.4)	4111	$1.563 \pm 0.003$	$0.099 \pm 0.002$	$1.990 \pm 0.005$	$0.179 \pm 0.004$	$0.397 \pm 0.011$

 TABLE 7  
 RADIAL METALLICITY GRADIENTS

Galaxy	$N(\text{blue})$	$a$	$b$	$N(\text{red})$	$a$	$b$
NGC1407	115	$1.630 \pm 0.010$	$-0.033 \pm 0.035$	225	$2.036 \pm 0.009$	$-0.027 \pm 0.028$
NGC3268	450	$1.597 \pm 0.007$	$-0.042 \pm 0.019$	292	$1.980 \pm 0.009$	$+0.002 \pm 0.025$
NGC3258	386	$1.604 \pm 0.008$	$-0.033 \pm 0.025$	306	$1.970 \pm 0.007$	$-0.030 \pm 0.024$
NGC3348	141	$1.581 \pm 0.012$	$-0.017 \pm 0.035$	148	$1.989 \pm 0.011$	$-0.036 \pm 0.038$
NGC4696	590	$1.628 \pm 0.004$	$-0.038 \pm 0.014$	576	$2.010 \pm 0.006$	$-0.011 \pm 0.018$
NGC7626	310	$1.615 \pm 0.007$	$-0.060 \pm 0.023$	326	$2.035 \pm 0.007$	$-0.068 \pm 0.026$
All 6	1992	$1.615 \pm 0.003$	$-0.0379 \pm 0.0068$	1873	$2.008 \pm 0.003$	$-0.0371 \pm 0.0079$

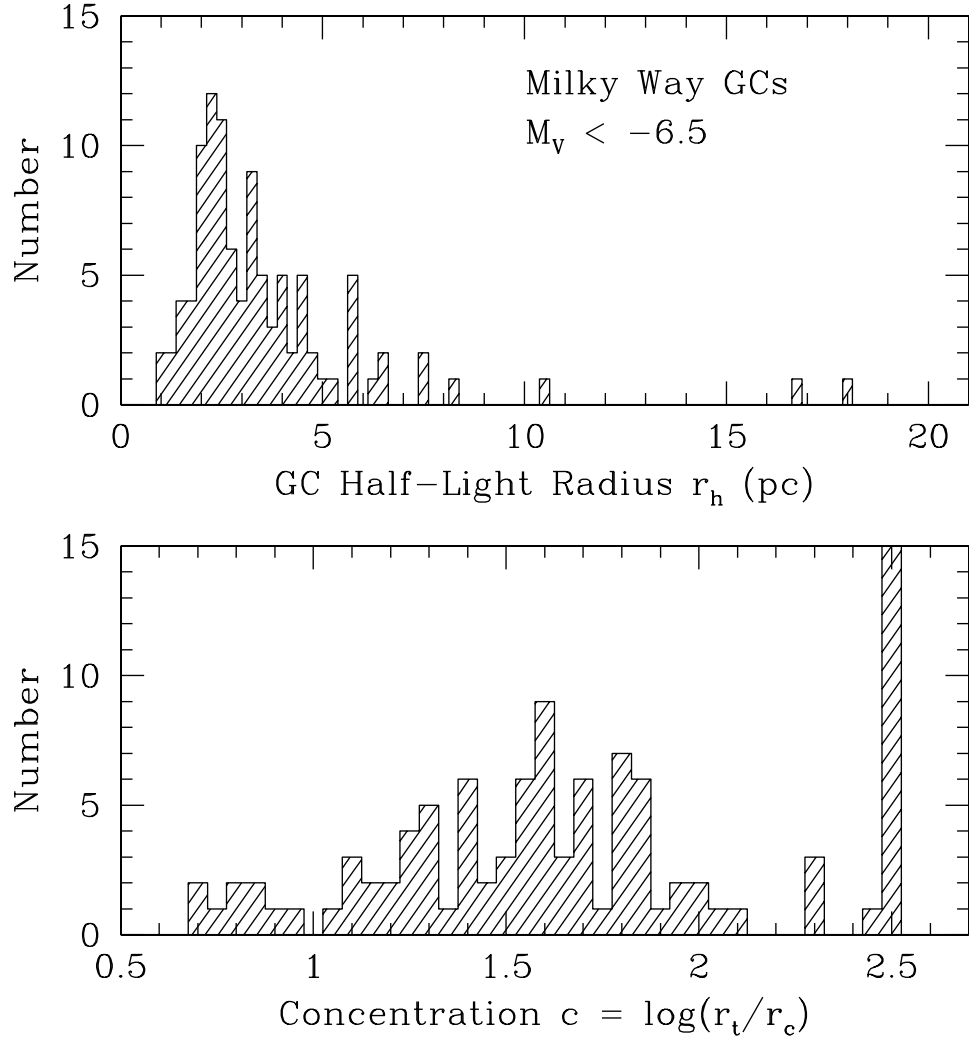


FIG. 1.— *Upper panel:* Distribution of half-light radii for Milky Way globular clusters. All 102 such clusters with luminosities brighter than  $M_V = -6.5$  are included here, to roughly match the luminosity range of the GCs observed in the six target galaxies of this study. Ninety percent of them have  $r_h < 6$  parsecs. Data are from Harris (1996). *Lower panel:* Distribution of King-model central concentration  $c = \log(r_t/r_c)$  for the same sample of Milky Way clusters above. The bin at  $c = 2.5$  is populated by the core-collapsed GCs, for which  $c = 2.5$  is arbitrarily assigned.



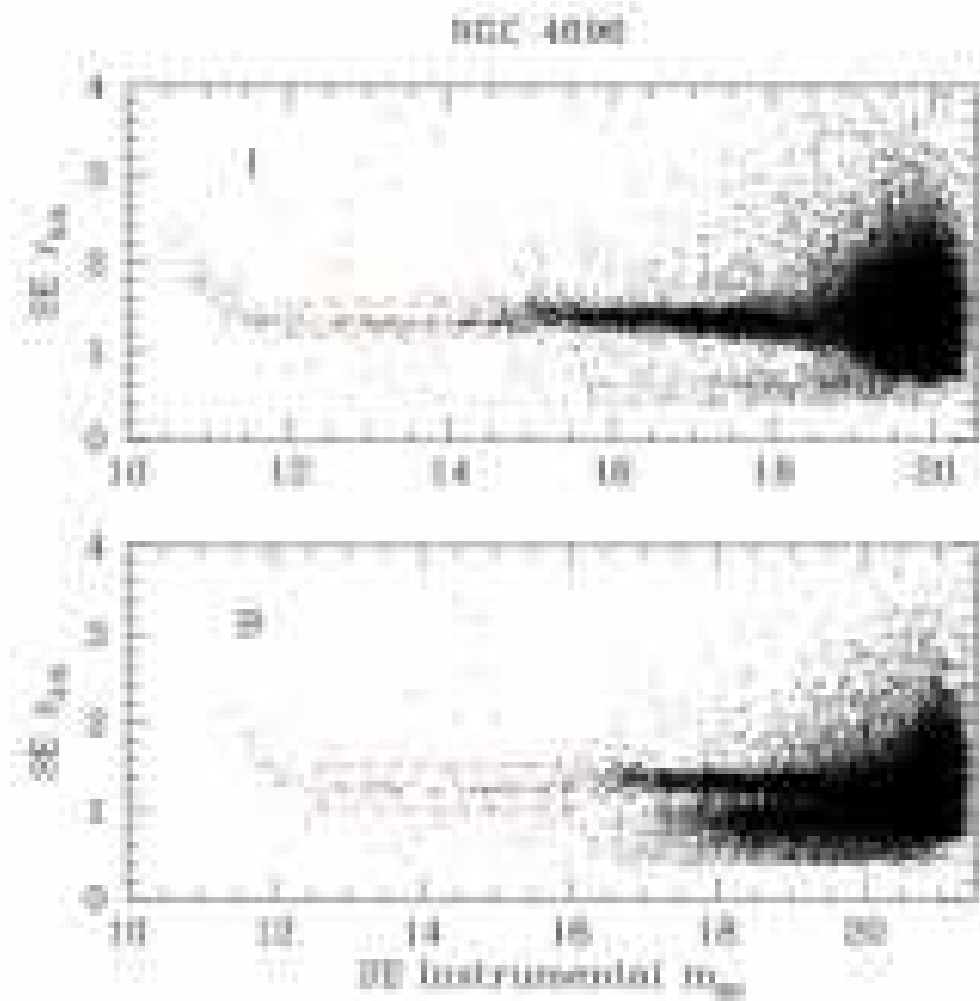


FIG. 2.— Selection of candidate stars for defining the stellar point spread function. The data shown here are SExtractor measurements of the half-light radius  $r_{0.5}$  versus an aperture magnitude, for all detected objects in the NGC 4696 galaxy field. No attempt has been made to cull out nonstellar objects or detections due bad pixels, clumps of noise, or other artifacts. The magnitude scales have arbitrary zeropoints and do not represent the true  $B, I$  magnitudes. Note in each panel the narrow sequence of “starlike” sources; at the very bright end ( $m_I < 12, m_B < 12.5$ ) these become saturated and the sequences curve upward. The dashed boxes mark out the objects that were chosen as candidate PSF stars for further investigation (see text).

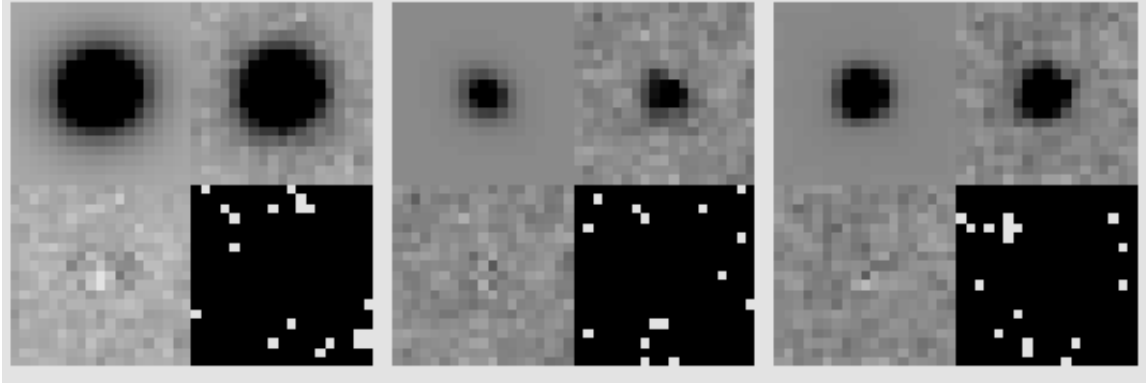


FIG. 3.— Three sample illustrations of the *ISHAPE* profile fits to objects in the NGC 4696 field. In each panel the upper right quadrant is the real object, the upper left quadrant shows the best-fitting model (that is, the King30 profile convolved with the PSF), and the lower left quadrant shows the residuals (real  $-$  model). The lower right quadrant shows the pixel weight map. (a) *Left panel*: A bright nonstellar object: the best-fit solution is for FWHM  $a = 1.3$  px, ellipticity  $b/a = 0.91$ , and  $S/N = 440$ . In this case the intrinsic size of the object is nearly as large as the PSF width of  $\simeq 1.8$  px. (b) *Middle panel*: A faint nonstellar object, for which  $a = 0.82$  px,  $b/a = 0.50$ , and  $S/N = 24$ . Note that the object looks much rounder than its intrinsic shape ( $b/a = 0.5$ ) because it has been convolved with the circularly symmetric PSF, whose FWHM is more than twice as wide. (c) A starlike object, for which  $a = 0$ ,  $b/a = 1$ , and  $S/N = 108$ .

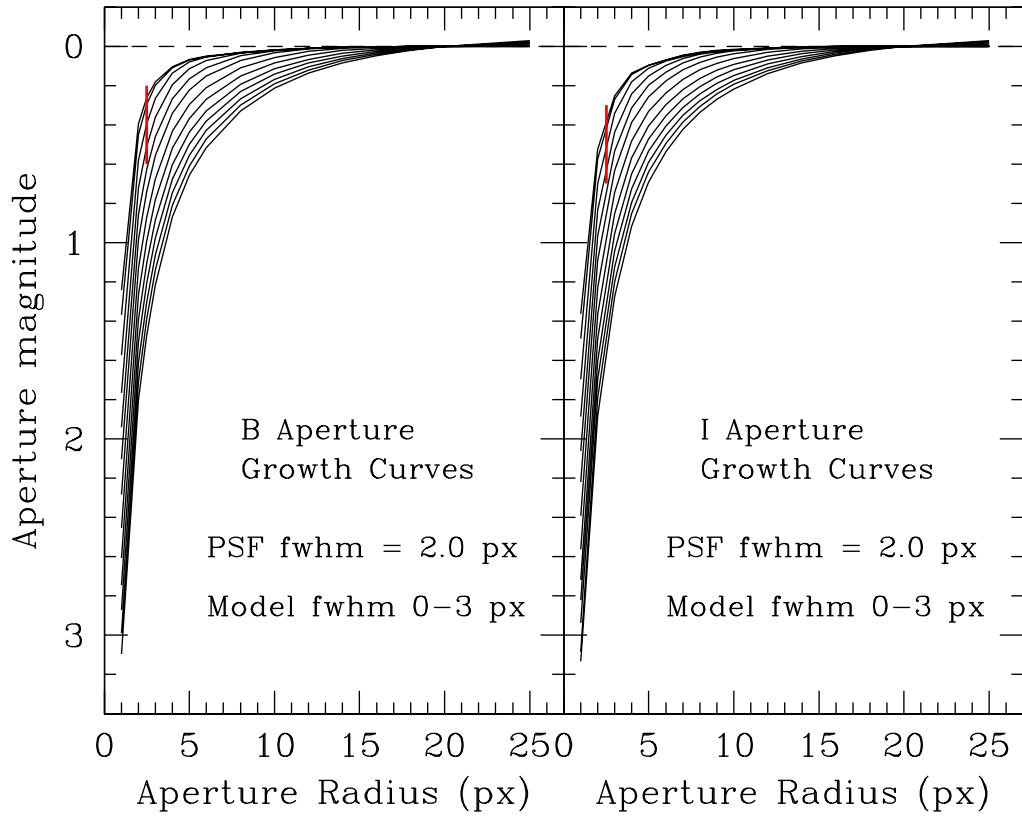


FIG. 4.— Curves of growth for simulated globular clusters. For each of the two graphs, the uppermost curve shows the magnitude enclosed within an aperture of radius  $r$  for a *starlike* object. All the other curves in each set show the curve of growth for simulated GCs of various sizes, convolved with the same stellar PSF profile. All the curves are plotted to converge at  $r = 20$  px (1 arcsecond). The more extended the GC profile is, the more gradually the curve of magnitude versus  $r$  increases: from top to bottom, the assumed GC profile FWHM values are (0.0, 0.2, 0.4, 0.6, 0.8, 1.0, 1.25, 1.50, 1.75, 2.0, 2.25, 2.50, 2.75, 3.0). The *vertical bar* plotted at  $r = 2.5$  px is the adopted radius for our fixed-aperture photometry, and it covers the typical range of GC profile widths for the GCs in our data.

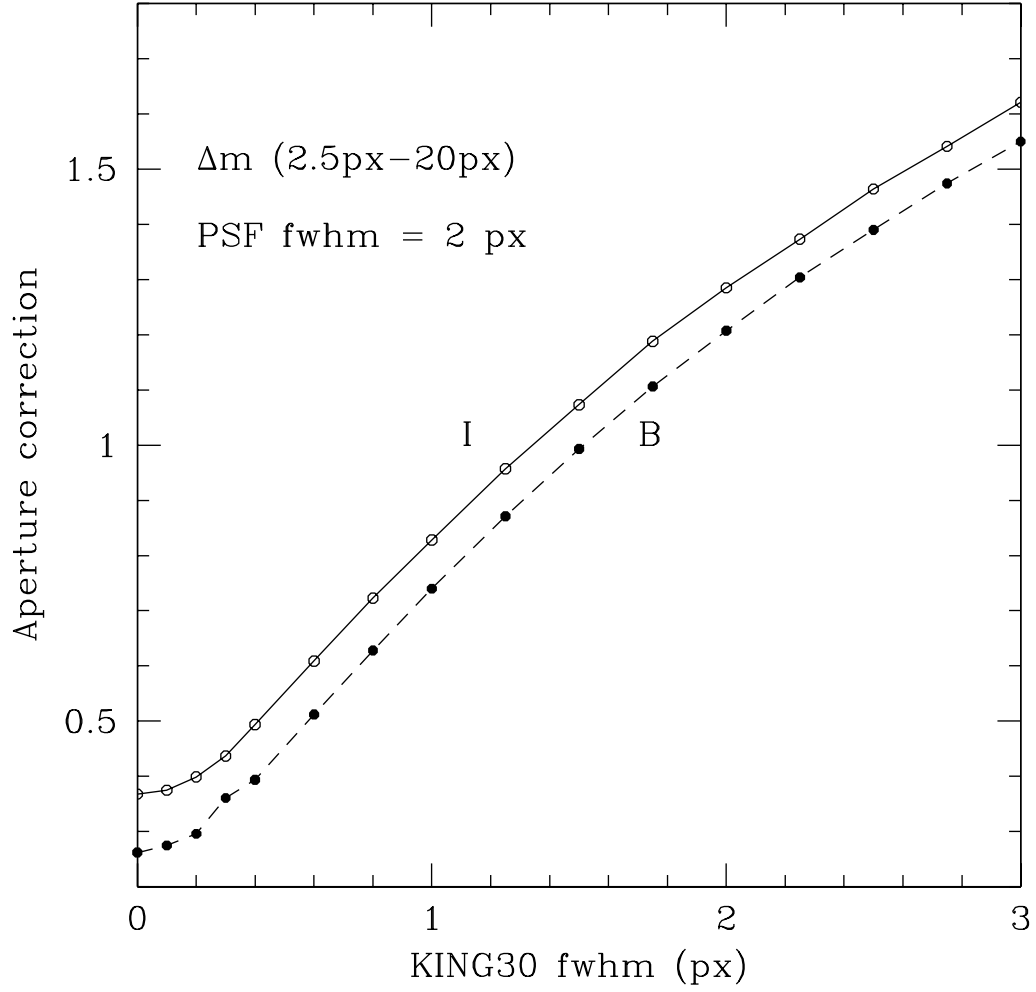


FIG. 5.— Aperture corrections plotted as a function of intrinsic size of the individual globular cluster. These are generated from the family of curves plotted in the previous figure, where the magnitude enclosed within  $r = 20$  px is defined as the “total” magnitude of the object. To obtain this total magnitude, the magnitude within a 2.5-px aperture is measured and then the aperture correction from this graph is subtracted. The data for our actual GCs fall in the regime FWHM  $\lesssim 0.6$  px, i.e. the lower left part of the curves.

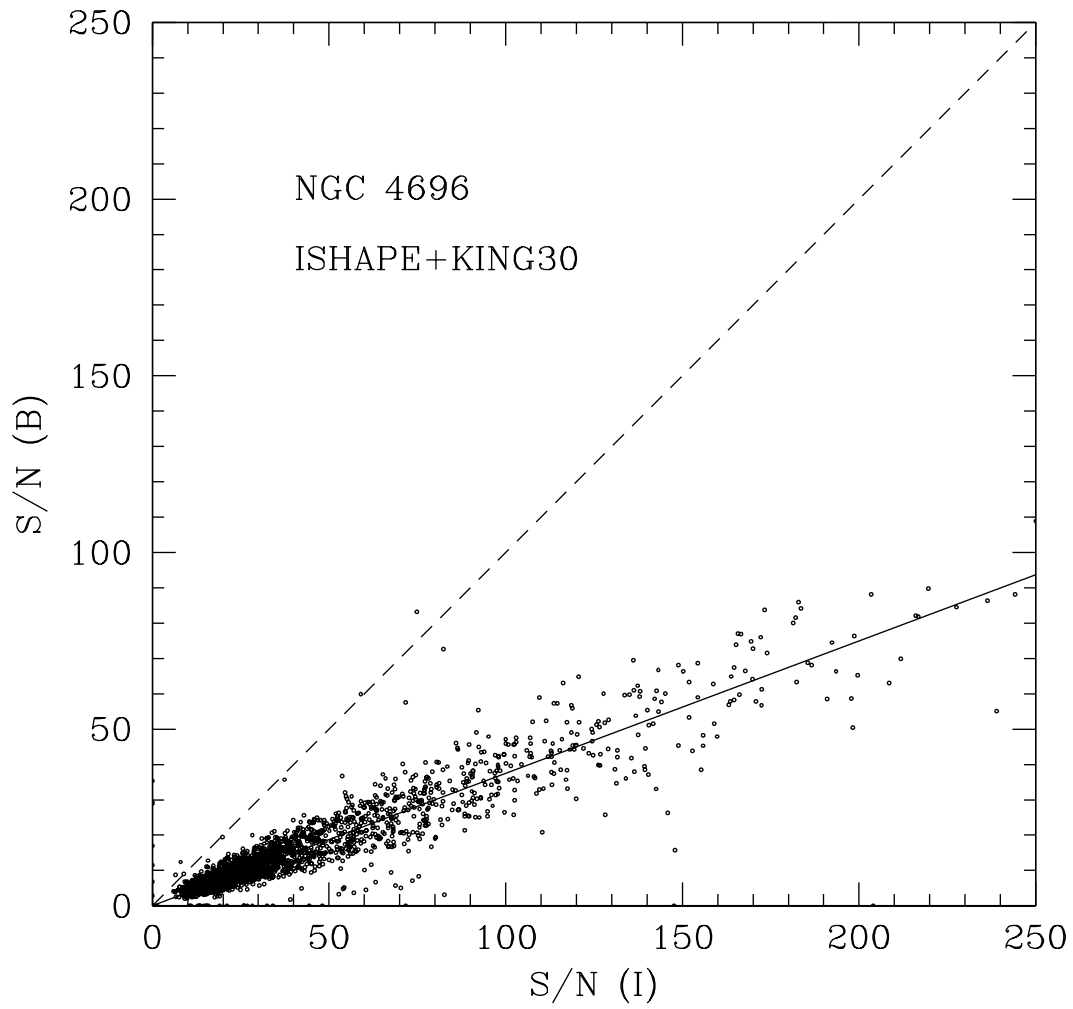


FIG. 6.— Scatter plot of the measured *ISHAPE* signal-to-noise in *B* versus the S/N for the same objects in *I*. Ideal 1:1 agreement would fall along the dashed line, while the solid line shows the actual correlation where  $S/N(B) \simeq 0.4 S/N(I)$ . Although the data for only the NGC 4696 field are shown, these results are typical of all six of the galaxy fields.

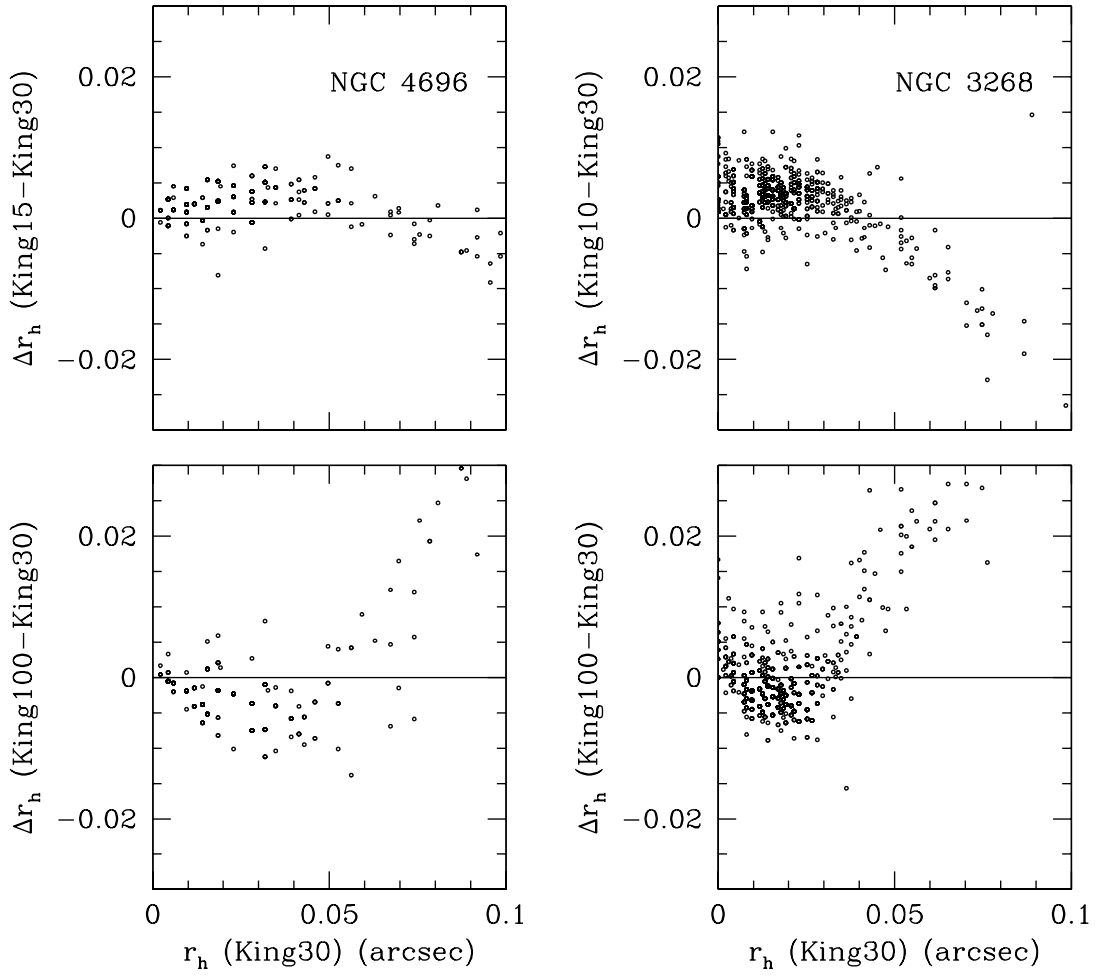


FIG. 7.— Tests of the sensitivity of our GC size measurement to the assumed central concentration  $c$  of the King model. The panels on the left show tests in the NGC 4696 field of the differences in measured  $r_h$  relative to the baseline King30 model, for (King15-King30) and (King100-King30). On the right, similar results are shown from the NGC 3268 field for the comparison (King10-King30) and (King100-King30). The units of both axes are in arcseconds.

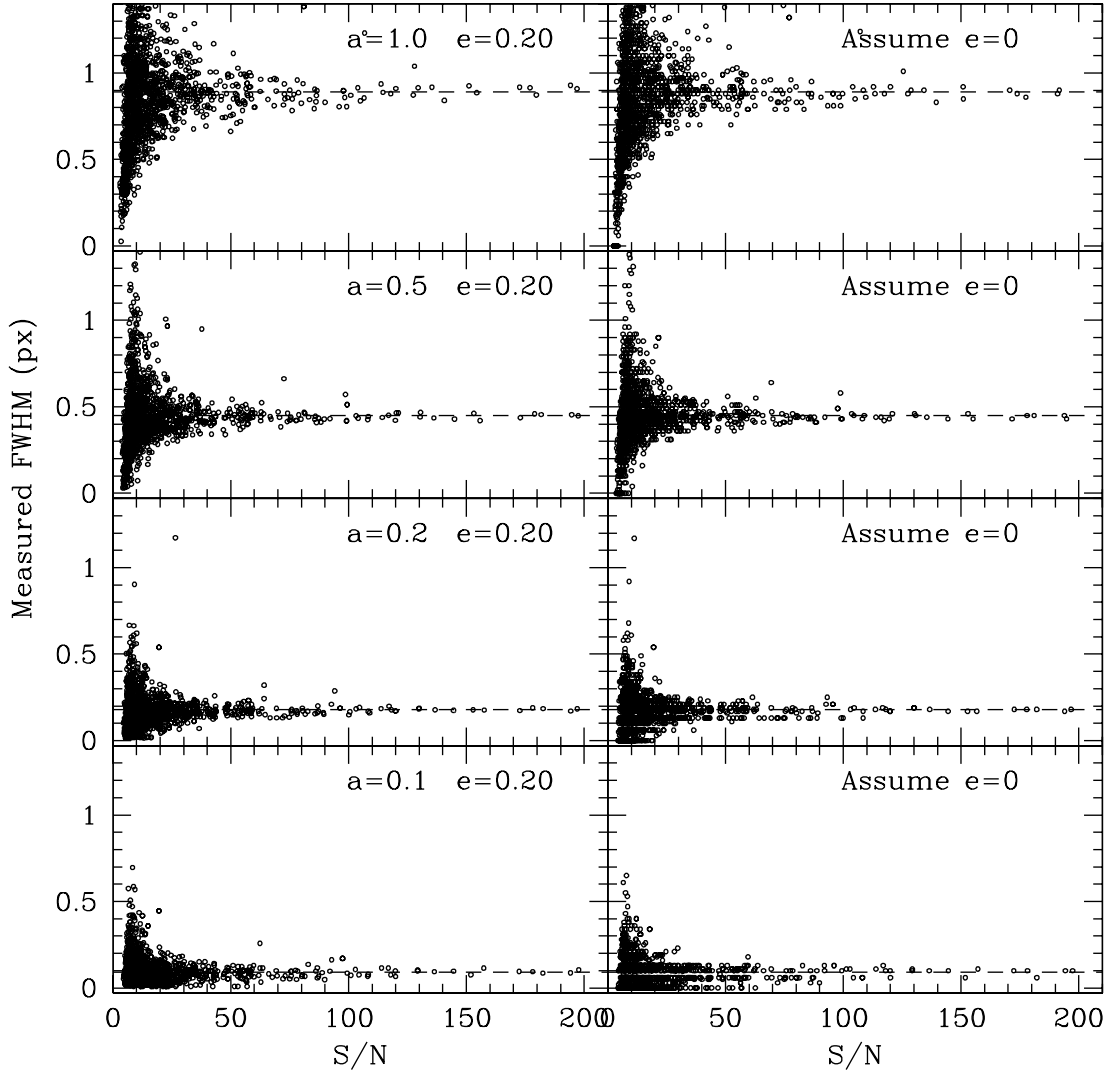


FIG. 8.— Tests of the sensitivity of our solutions for GC size to the assumed ellipticity  $e$ . The simulated clusters have an assumed King30 profile with  $\text{FWHM}=a$ , convolved with a model PSF with  $\text{FWHM}=2.0$  pixels. In each graph the correct (input) value of the intrinsic FWHM of the clusters is shown as the horizontal dashed line. In the left-hand set of graphs, ISHAPE was allowed to solve for both the FWHM and the ellipticity, while in the right-hand set, it was forced to assume  $e=0$  and solve only for the FWHM.

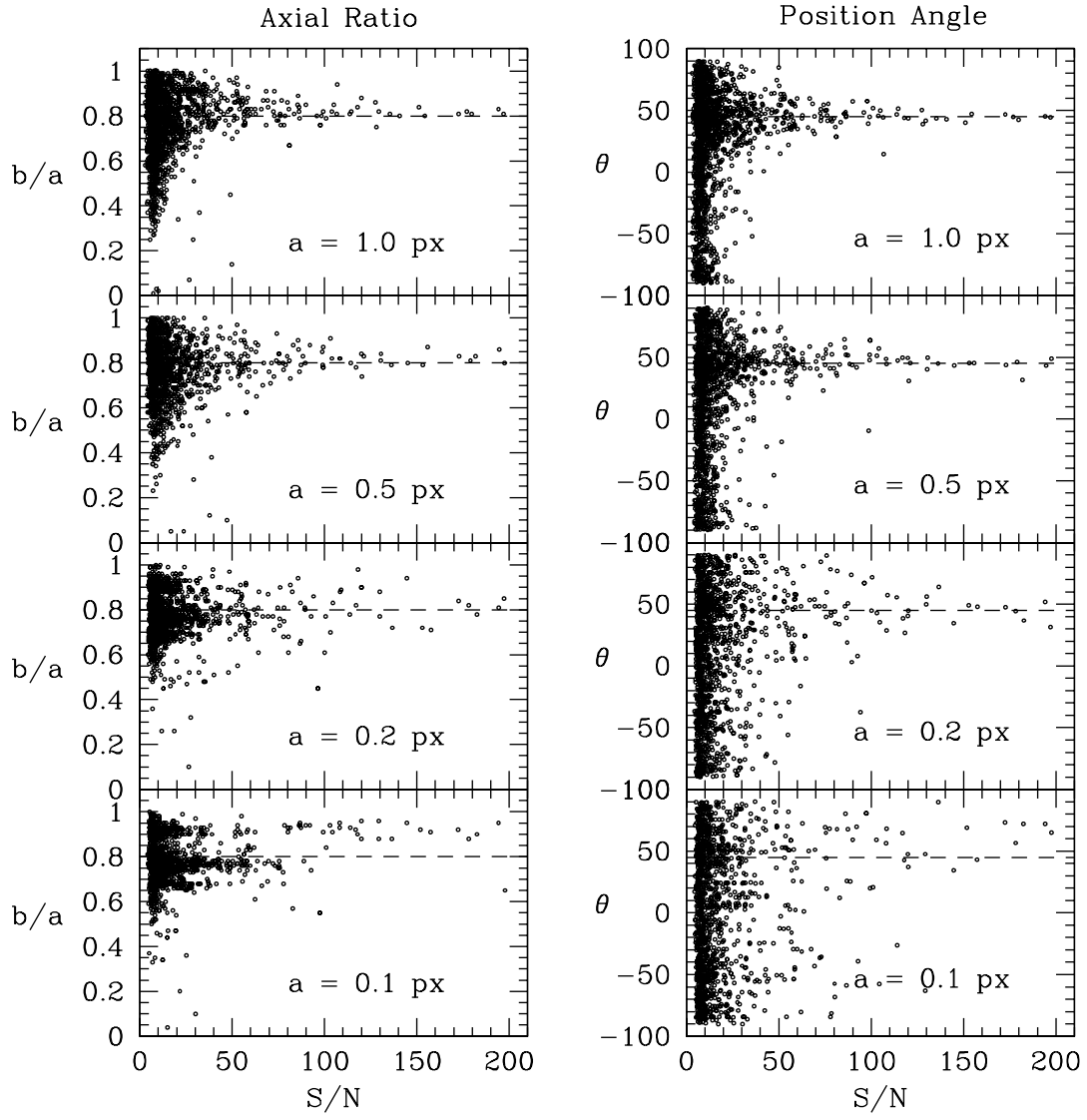


FIG. 9.— Tests of ISHAPE solutions on simulated clusters for the object shape  $(b/a) = (1 - e)$  and orientation angle  $\theta$  as functions of object brightness and size. The correct (input) values are  $(b/a) = 0.8$  and  $\theta = 45^\circ$ , as shown by the horizontal dashed lines.



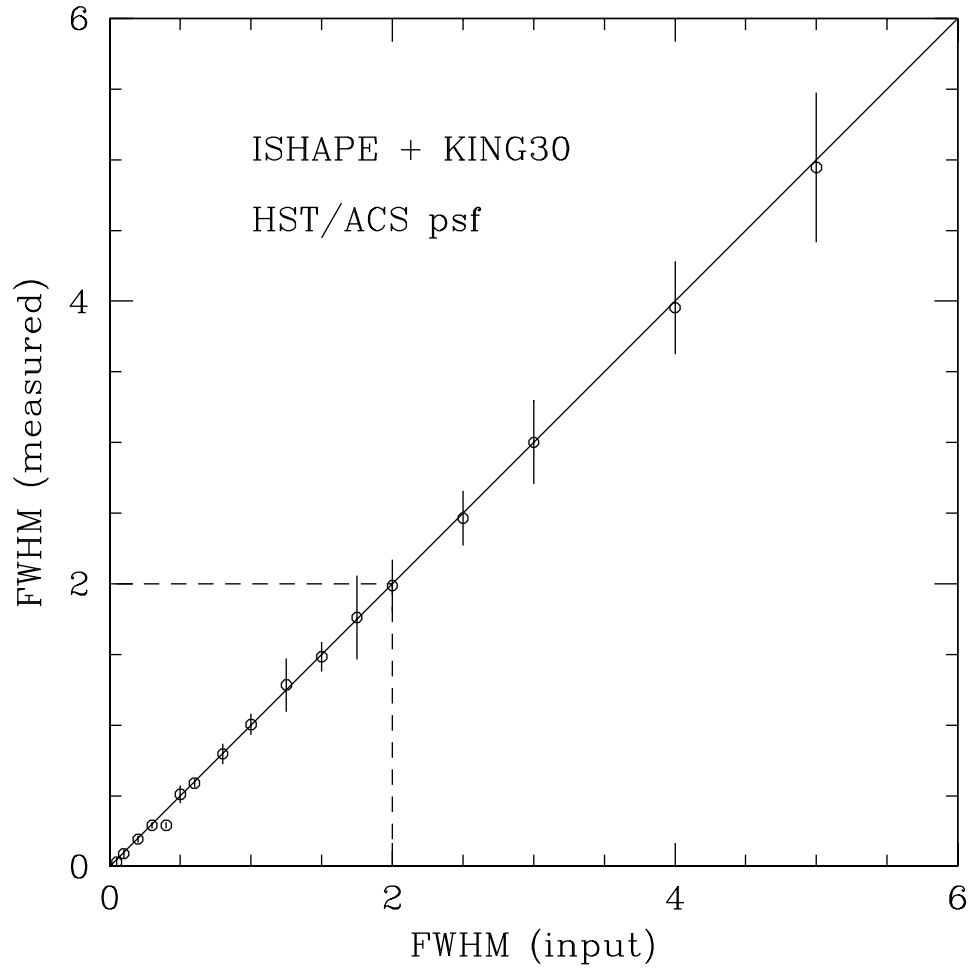


FIG. 10.— Tests of the *ishape* measurements for simulated globular clusters of various intrinsic sizes. KING30 model GCs of an assumed input FWHM (measured in pixel units, where  $1 \text{ px} = 0.05''$ ) and a range of luminosities are convolved with the stellar point-spread function and inserted into the image on top of realistic background noise. These simulated objects are then measured with *ISHAPE* and the measured FWHM is plotted against the input value. The dashed lines show the FWHM of the assumed stellar PSF at 2.0 px. These tests show that accurate values of the GC sizes can be recovered down to  $\text{FWHM} \simeq 0.2 \text{ px}$ , or 10% of the stellar FWHM.

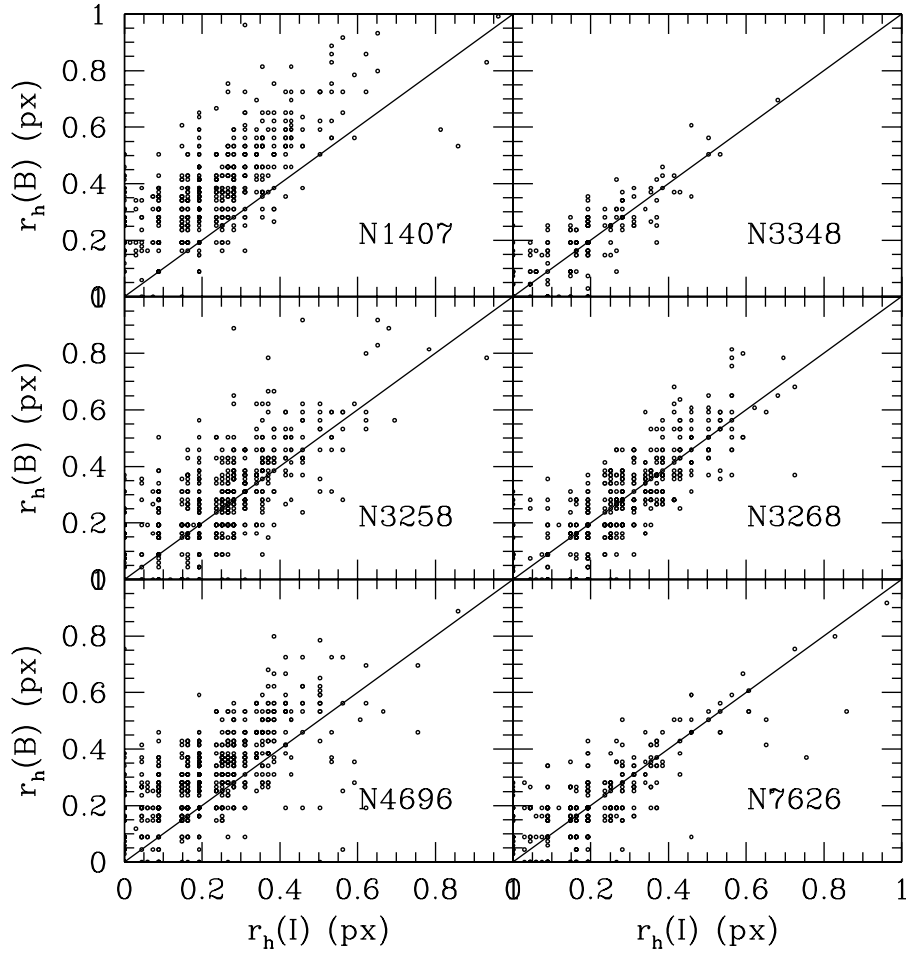


FIG. 11.— Comparisons of the *ishape* measurements of object size for the real objects in each of the six galaxy fields. Here the best-fit half-light radius  $r_h = 1.48 \text{ fwhm}$  from ISHAPE is shown in  $B$  versus  $I$  for all objects with ISHAPE total  $S/N > 50$ . Ideal one-to-one agreement is shown by the solid lines.

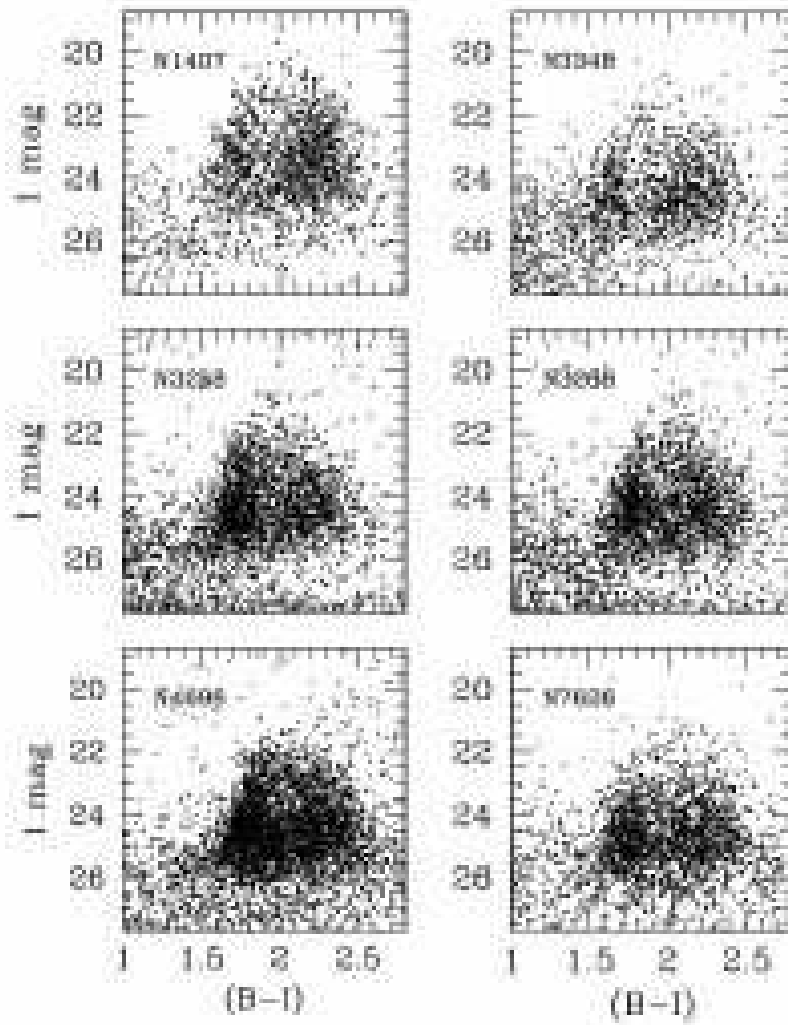


FIG. 12.— The color-magnitude data for the measured objects in each of six target galaxy fields. Each individual object is plotted with its fully size-corrected ( $B, I$ ) magnitudes as described in the text. The majority of the objects in each field are the globular cluster populations. The main source of field contamination is predominantly from small, faint background galaxies.

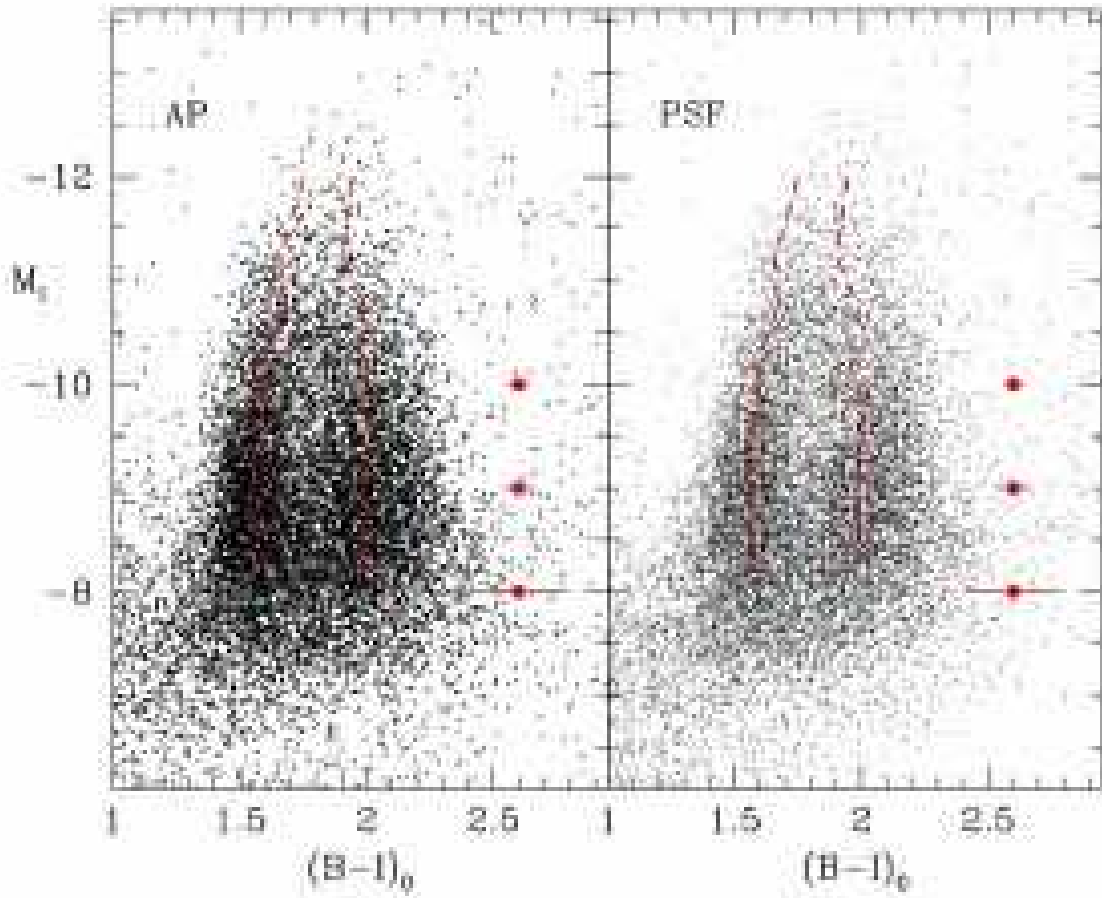


FIG. 13.— The color-magnitude data for all six galaxies, now converted to luminosity and intrinsic color ( $M_I, (B - I)_0$ ) and with all fields combined. The *left panel* shows the size-corrected aperture photometry from the current discussion, while the *right panel* shows the data for the same fields based solely on PSF fitting as published earlier in Harris et al. (2006). The mean lines through the blue and red globular cluster sequences for the newer data at left are shown by the heavy dashed lines. The *same lines* are repeated in the right panel to indicate the small offsets between the two datasets. Sample errorbars showing the measurement uncertainties of the photometry are shown for  $M_I = -8, -9, -10$ .

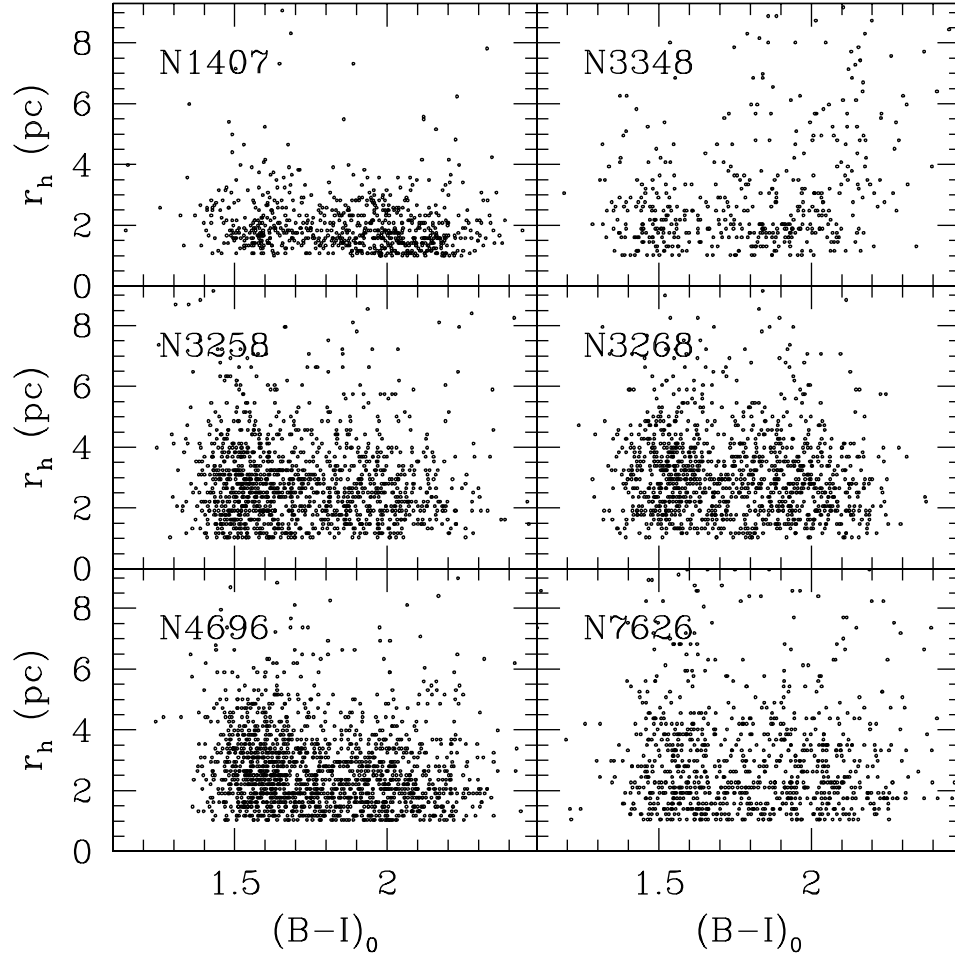


FIG. 14.— Measured half-light radii for the individual globular cluster candidates in the six galaxy fields. Only the objects with  $r_h > 1$  pc are plotted, though they have not been selected by  $(S/N)$ . The two metallicity groups (blue and red clusters) can be seen in each sample. Over all six fields, the total is 6476 objects.

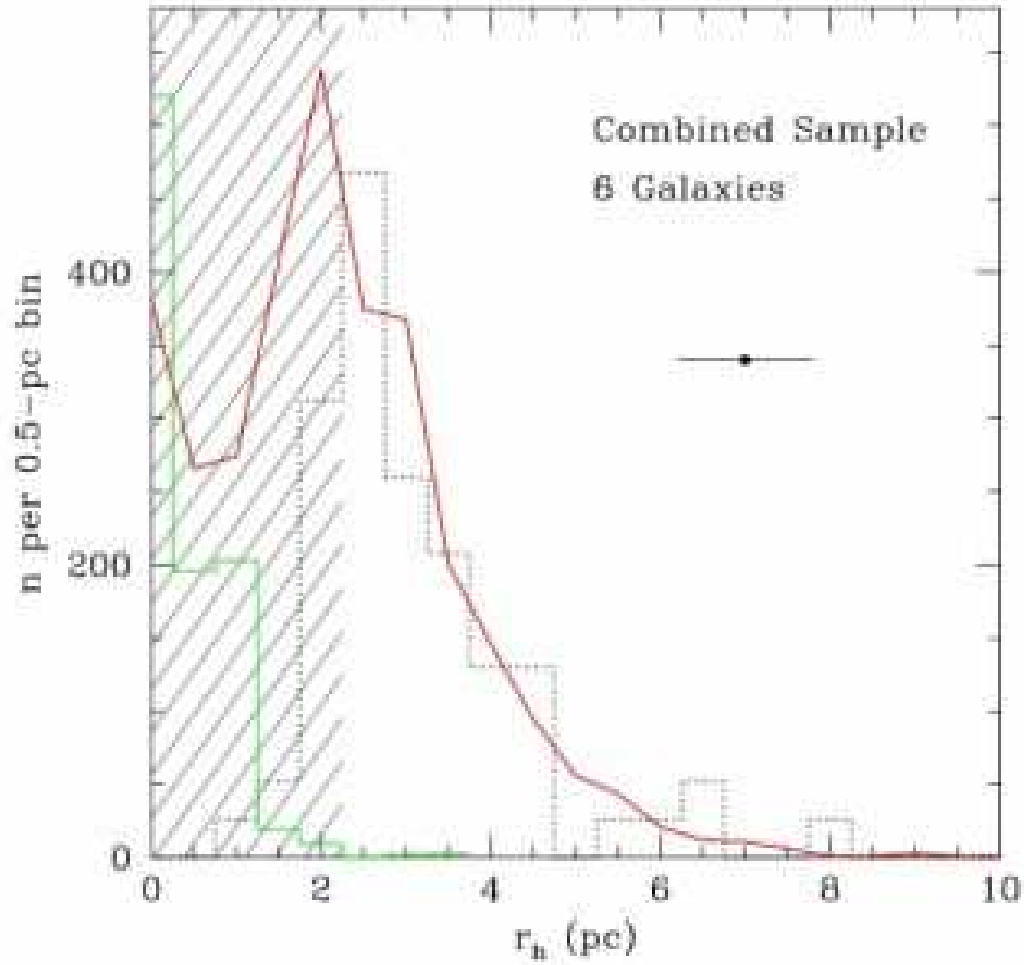


FIG. 15.— Histogram (solid broken curve) of the best-quality size measurements ( $S/N > 50$ ) for 3330 objects as determined by ISHAPE, over all six galaxy fields combined. All measurements of the object size are converted to half-light radius in parsecs. The shaded area covering  $r_h \lesssim 2$  pc indicates the approximate size range within which ISHAPE cannot easily distinguish starlike from nonstellar objects. For comparison, the block histogram on the left side of the graph peaking at  $r_h = 0$  shows the distribution of measured radii that ISHAPE returned for 5300 simulated *starlike* objects at an assumed distance of 40 Mpc; all of these by definition have true radii  $r_h = 0$ . Finally, the dotted histogram shows the size distribution for the 66 globular clusters in the Milky Way that are more luminous than the GC luminosity function turnover point and no further than 20 kpc from the Galactic center (see text).

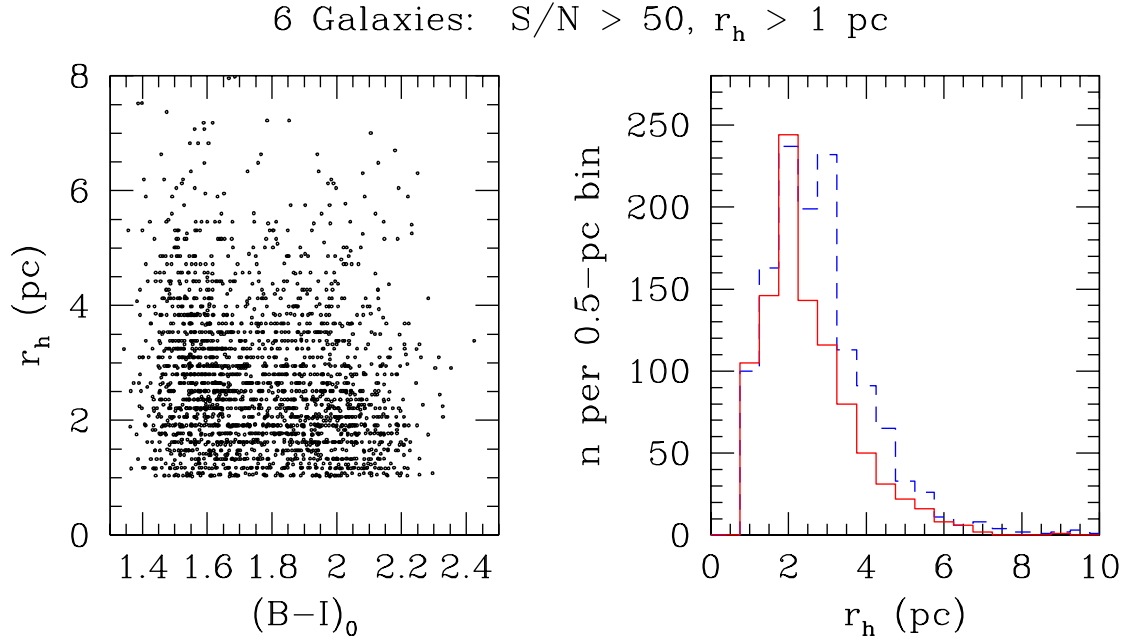


FIG. 16.— *Left panel:* Measured half-light radii for the combined globular cluster populations in all six galaxies. The best-quality 2495 objects with sizes larger than  $r_h = 1$  pc and with  $(S/N) > 50$  are shown. *Right panel:* Histograms of the  $r_h$  values for the metal-poor GC population ( $1.3 < (B-I)_0 < 1.8$ , solid line) and the metal-rich population ( $1.8 < (B-I)_0 < 2.4$  dashed line).

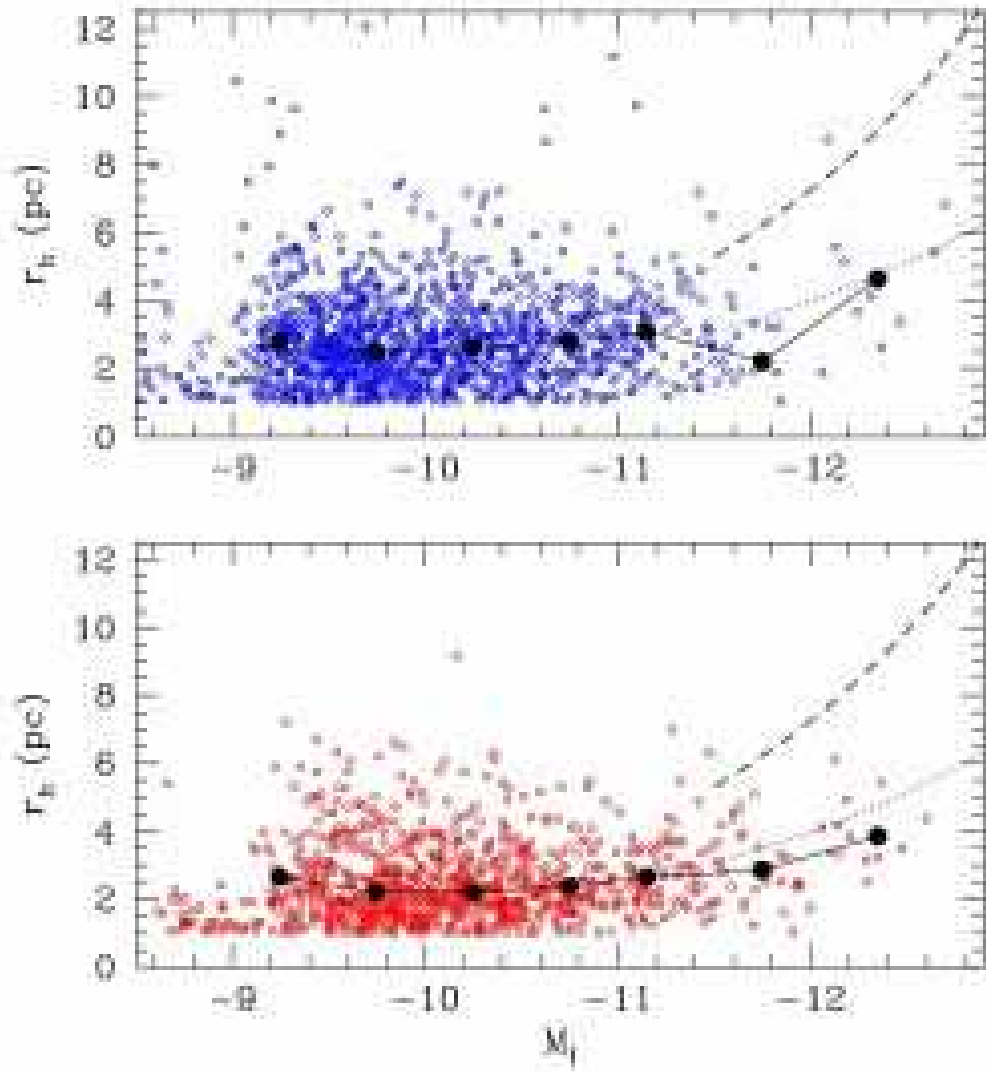


FIG. 17.— *Upper panel:* Half-light radii for the metal-poor globular clusters, plotted versus cluster luminosity  $M_I$ . Data are the same as in the previous figure. Median values of  $r_h$  from Table 3 in half-magnitude intervals are shown as the large dots. *Lower panel:* The same data for the metal-rich globular clusters. On average the metal-poor clusters have median sizes about 15% larger than do the metal-rich ones, at any luminosity. The heavy dashed lines at the right in each panel show the mean size/luminosity relation for UCDs and dE nuclei, from Evstigneeva et al. (2008). The dotted lines show the *lower envelope* of the same UCD/dE,N relation.



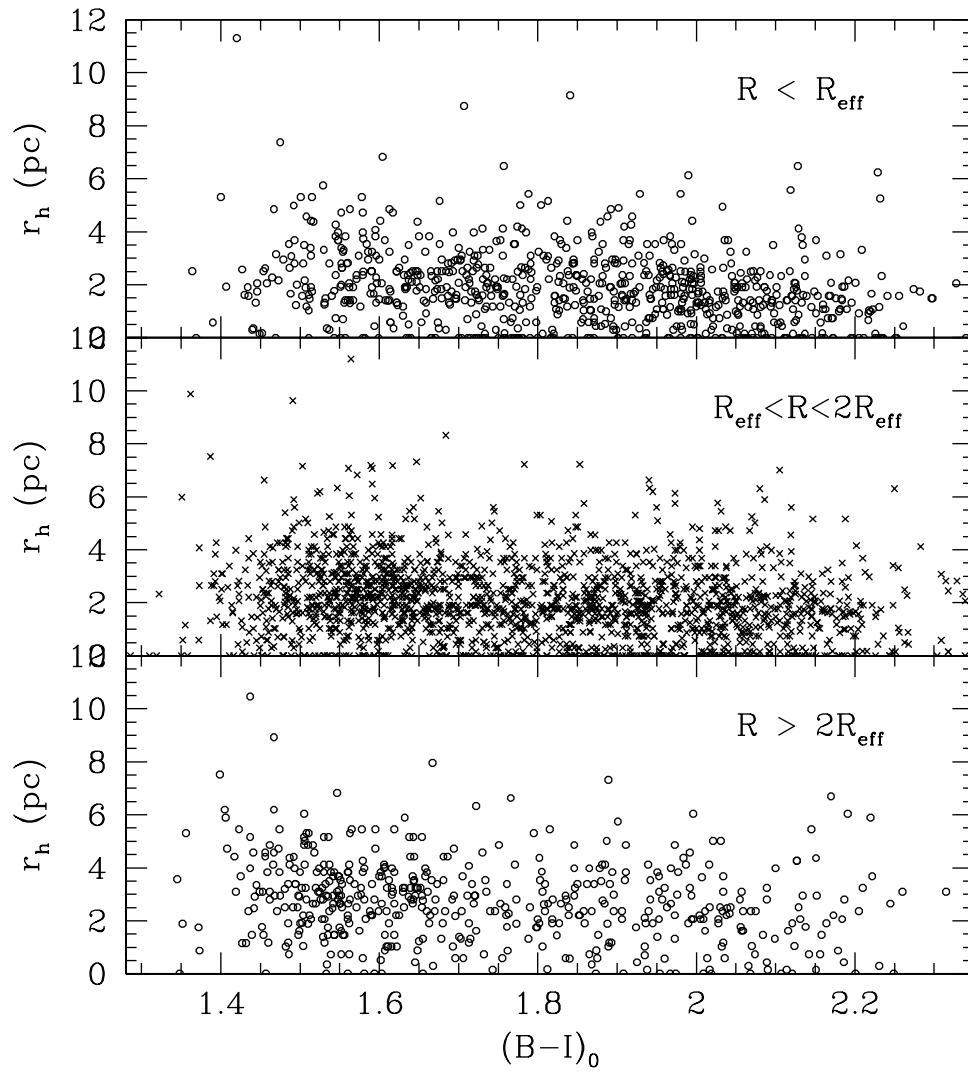


FIG. 18.— The half-light radii for globular clusters plotted as a function of color (metallicity), for three radial zones of galactocentric distance.

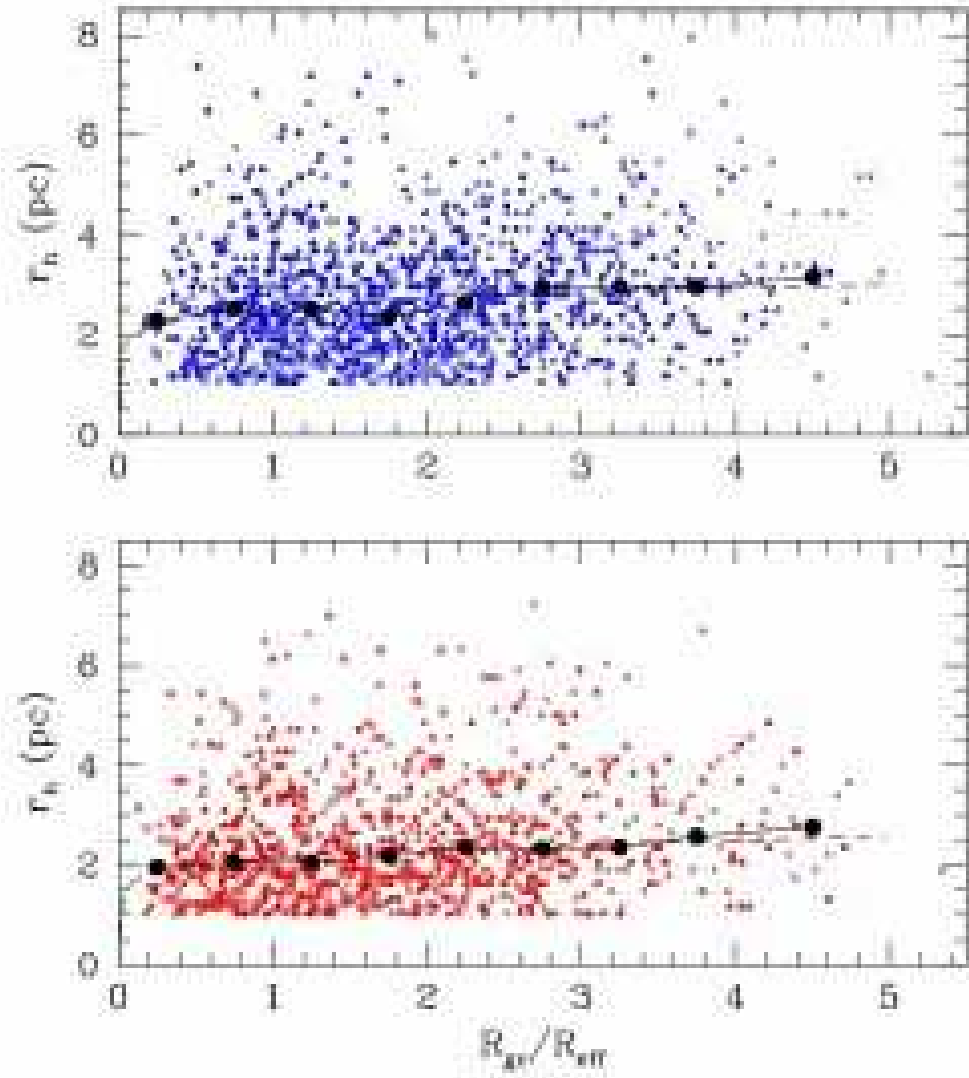


FIG. 19.— The half-light radii for globular clusters plotted as a function of galactocentric distance. *Upper panel:* Blue, metal-poor GCs defined as in the previous figures; *Lower panel:* Red, metal-rich GCs. The large connected dots show the empirical trend of the median  $r_h$  value. The *dashed lines* give the power-law fits to the median points, with equations as given in the text.

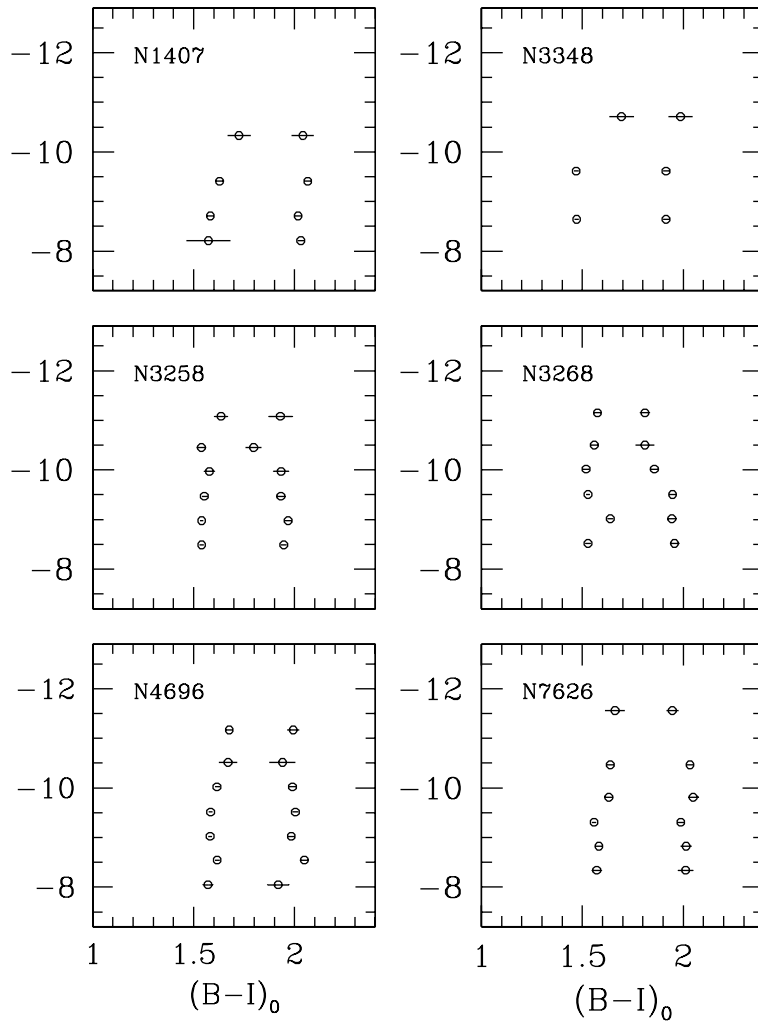


FIG. 20.— Deconvolution of the  $(B - I)$  color distributions for the GC populations in the six individual galaxies. The fitting code RMIX (see text) has been used to isolate the best-fit mean colors of the blue and red sequences, as listed in Table 5.

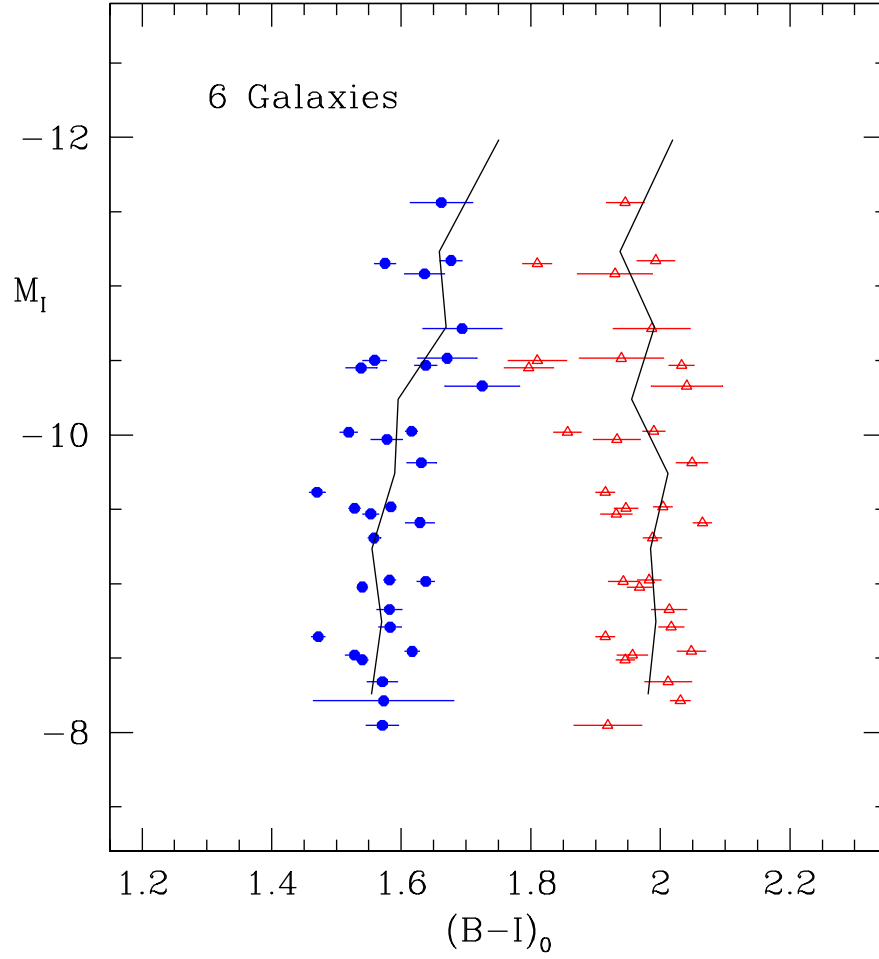


FIG. 21.— Mean points in  $(M_I, (B - I)_0)$  for all six galaxies, as determined from the bimodal Gaussian fits listed in Table 5. *Solid dots* are the fiducial points for the blue sequence, *open triangles* for the red sequence. The *solid lines* through each sequence connect the mean points as determined from the combined dataset in Table 6.

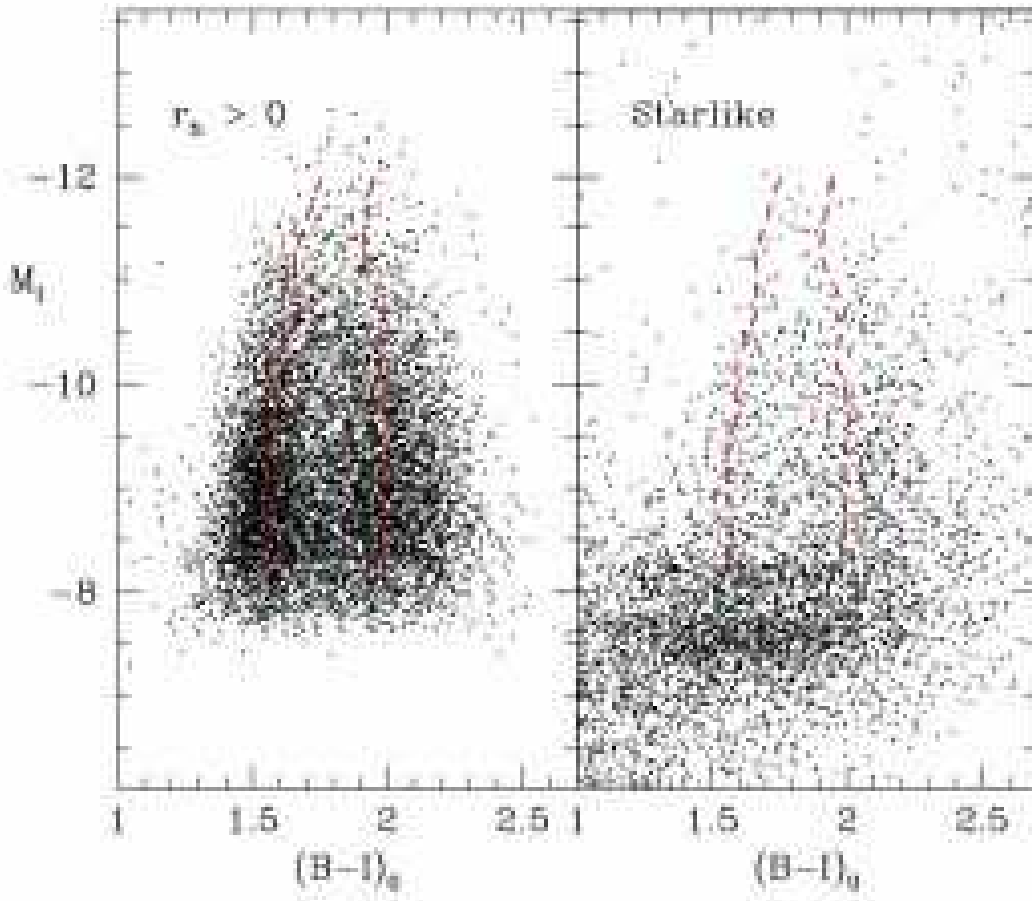


FIG. 22.— *Left panel:* CMD for all objects with positive measurements of effective radius  $r_h$ . *Right panel:* CMD for all objects with either “starlike” size measurements ( $r_h = 0$ ) or those too faint for successful ISHAPE fits. The heavy dashed lines showing the red and blue GC sequences are the same as in previous figures.

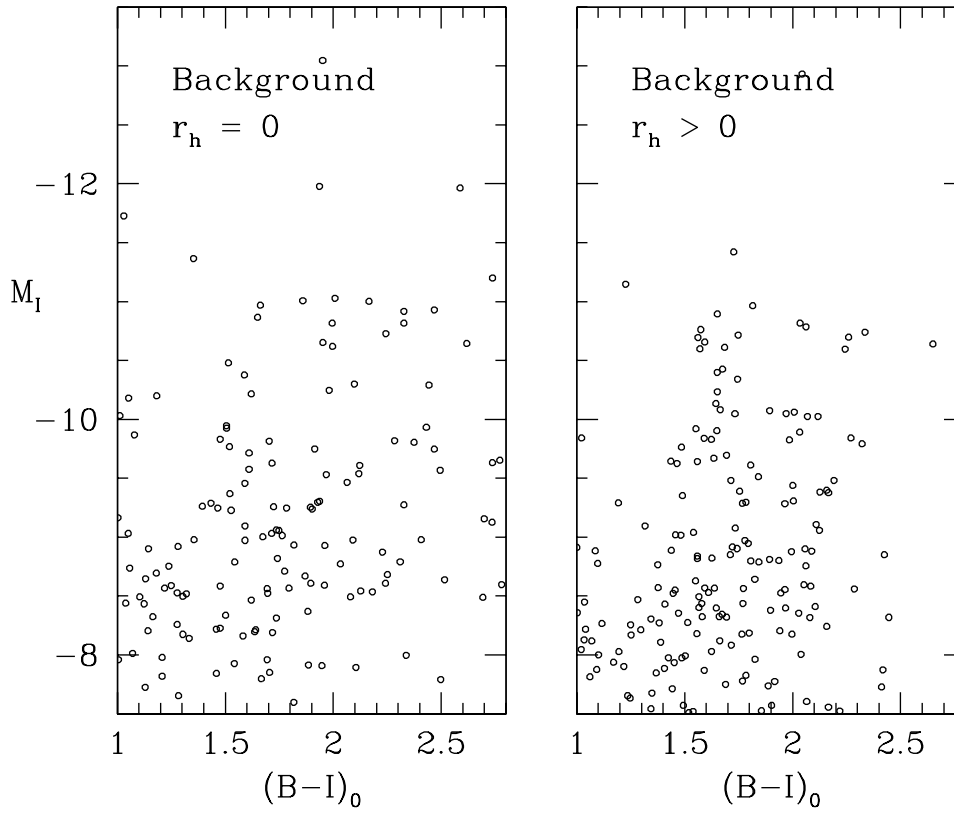


FIG. 23.— *Left panel:* CMD for all starlike objects in the outer regions of the three “control field” galaxies, NGC 5322, 5557, and 7049. The data have been measured and converted to absolute magnitude and color as described in the text. *Right panel:* CMD for all control-field objects with positive size measurements. Note the presence of globular clusters along the normal blue and red sequences in the outskirts of these three galaxies.

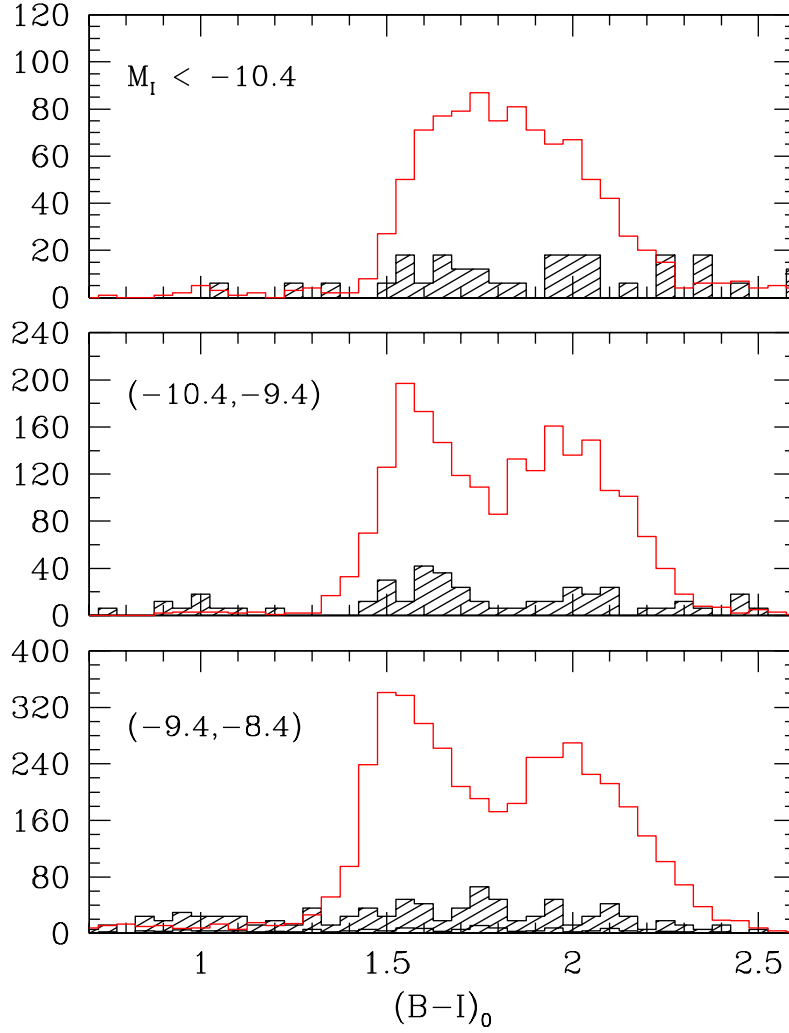


FIG. 24.— Histograms in  $(B - I)_0$  for the measured objects in all the galaxy fields combined, subdivided by GC luminosity  $M_I$ . The *unshaded* histograms show the numbers of objects per 0.05-mag color interval in the six program galaxies. The *shaded* histograms show the numbers in the composite “control field” (see text), multiplied by a factor of 6 to match the total areas. The control field data represent only an upper limit to the true background contamination level.

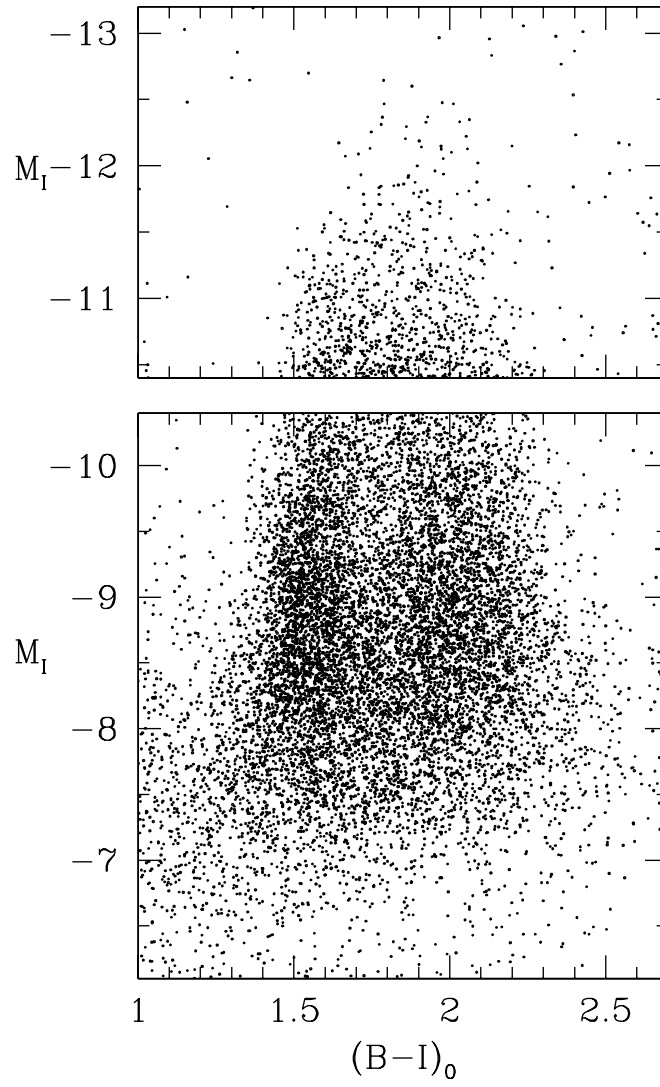


FIG. 25.— *Upper panel:* color-magnitude distribution for the GCs in all six galaxies, in the luminosity interval  $M_I < -10.4$ . *Lower panel:* color-magnitude distribution for the fainter objects,  $M_I > -10.4$ . The reader is invited to block off each panel in turn to view the other one independently.



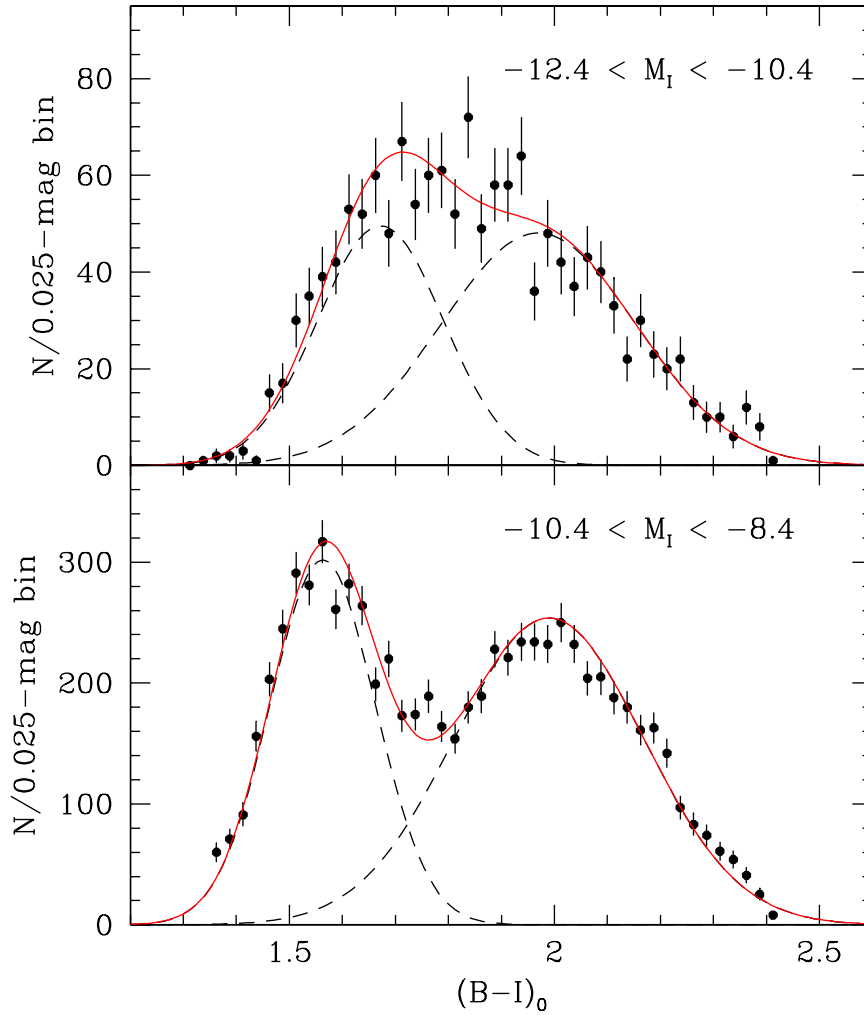


FIG. 26.— Deconvolution of the  $(B - I)$  color distributions for the GC populations in the combined data sample. The upper panel shows the histogram and the RMIX two-gaussian fit for the brightest clusters, in the luminosity range  $M_I = (-12.4, -10.4)$ . The lower panel shows the same data for the less luminous clusters in the range  $M_I = (-10.4, -8.4)$ . Note that the faint limit  $M_I = -8.4$  is approximately the level of the GCLF turnover point (see text).

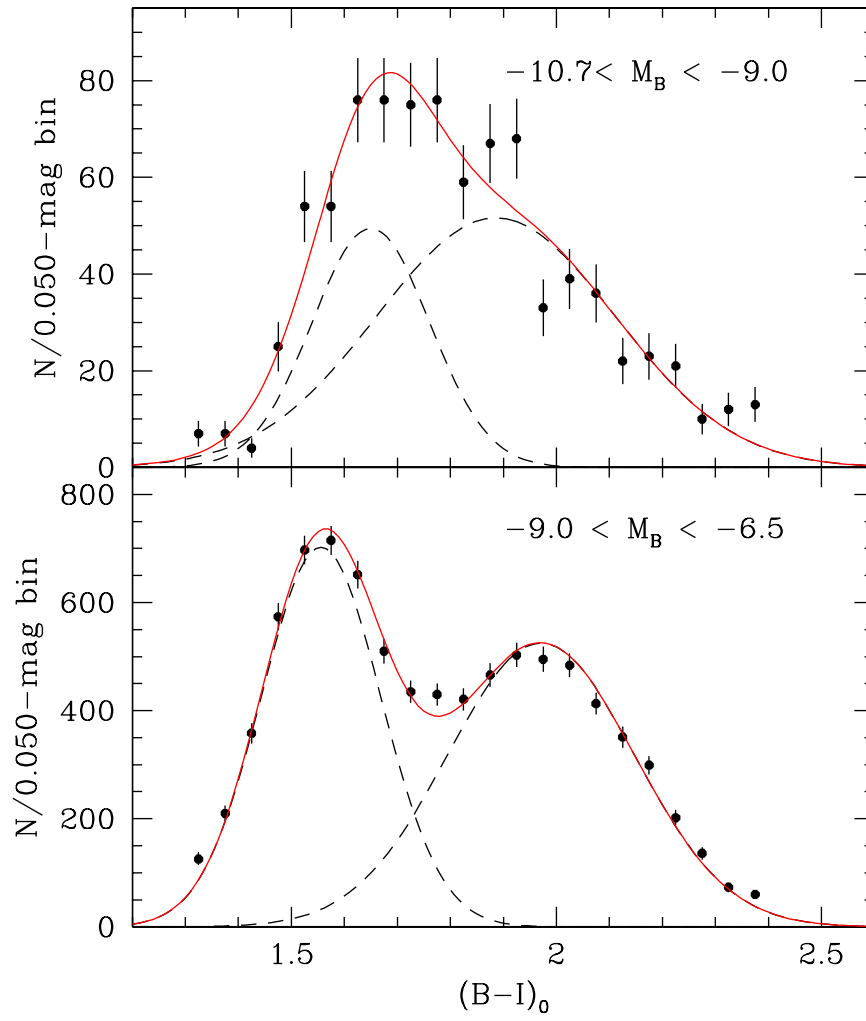


FIG. 27.— Deconvolution of the  $(B-I)$  color distributions for the GC populations in the combined data sample, as in the previous figure but now plotted in intervals of absolute  $M_B$  magnitude.

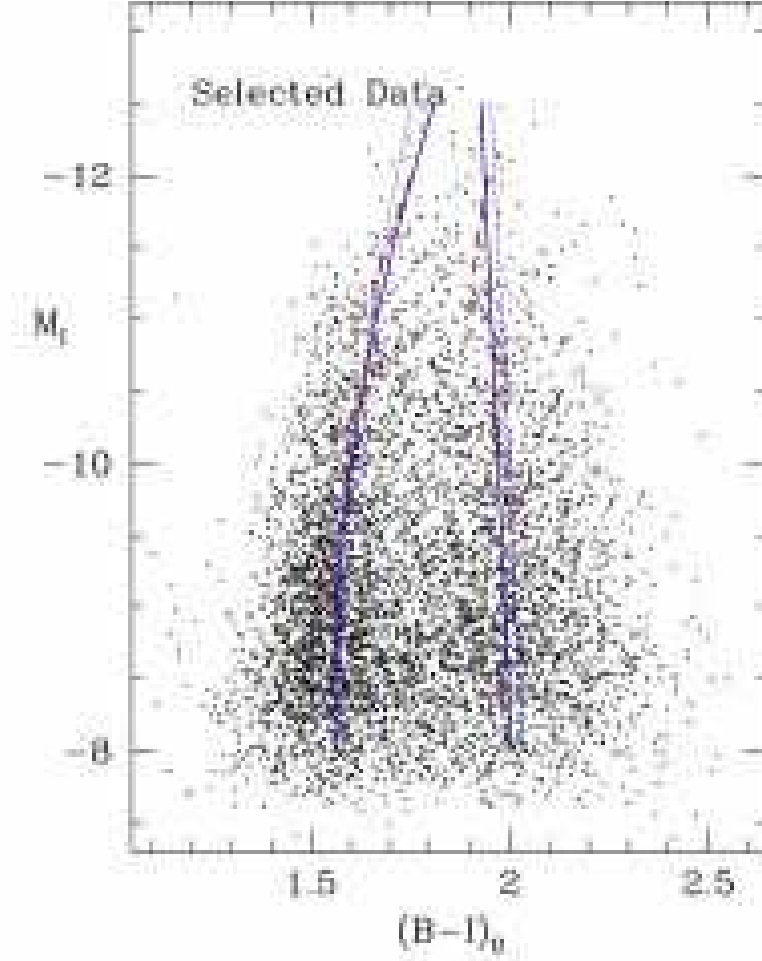


FIG. 28.— CMD for the 7831 measured objects with size measurements  $r_h > 1.5$  pc, drawn from the previous Fig. 22. This sample minimizes field contamination and provides the best visual representation of the blue and red GC sequences. The heavy *dashed lines* show the mean points along the two sequences, as listed in Table 6. The *solid lines* shows the polynomial fits to these mean points as given in equations (5,6), and the *dotted lines* show the same polynomial fits determined directly from the individual cluster data divided at  $(B - I)_0 = 1.8$  (see text).

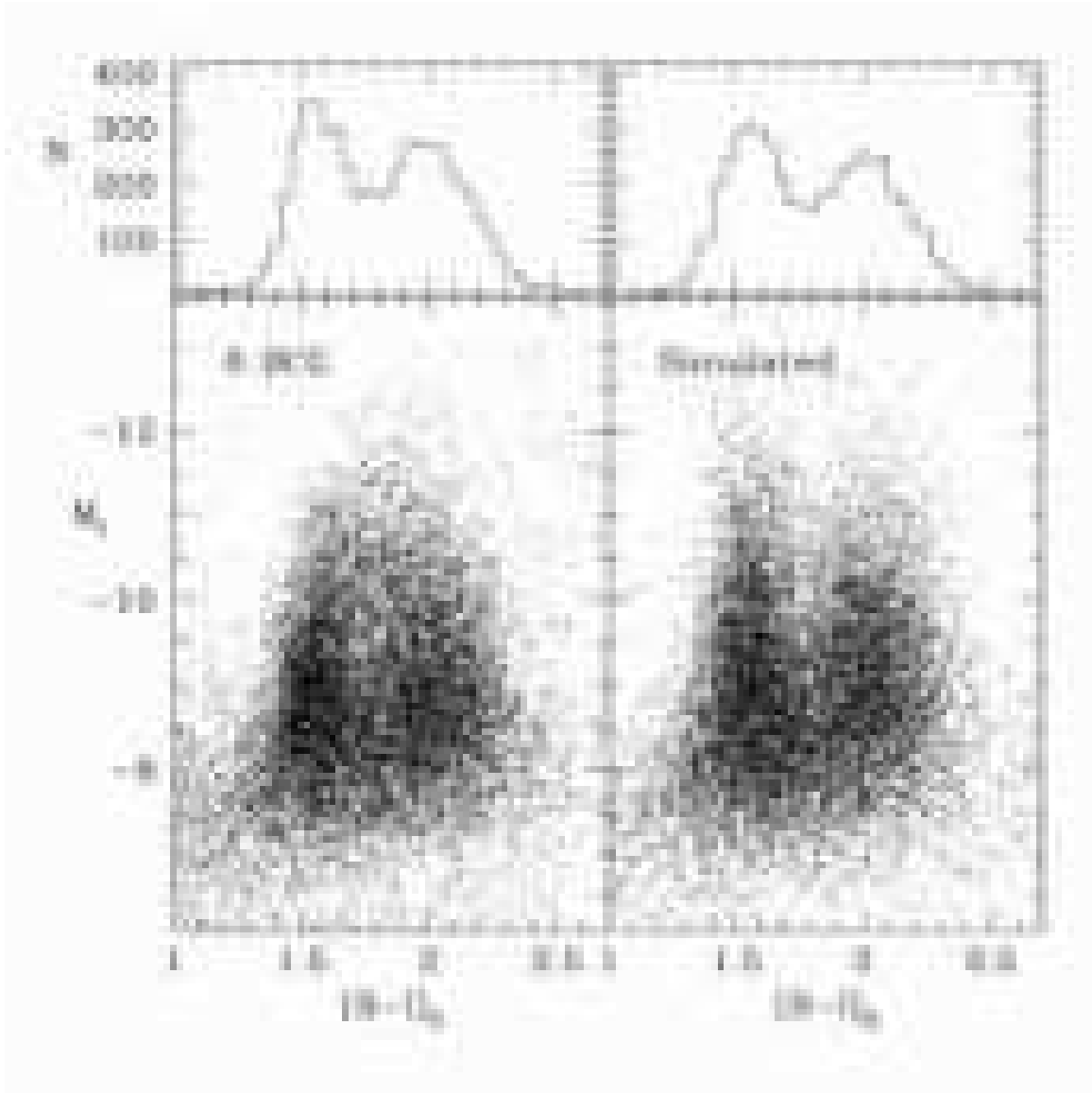


FIG. 29.— *Left panel:* Combined color-magnitude data for the six BCGs, from Fig. 13a. The histogram at top shows the distribution in  $(B-I)_0$  for the luminosity range  $-10.0 < M_I < -8.5$ , a range fainter than the main region of the MMR but brighter than the region where the colors are broadened significantly by observational measurement scatter. *Right panel:* Simulated data for a bimodal GC population with parameters as described in the text. Both the red and blue sequences are purely vertical (no MMR), with mean colors  $(B-I)_0 = 1.56$  and  $2.00$ . The histogram above shows the color distribution for the same luminosity region ( $-10.0, -8.5$ ).

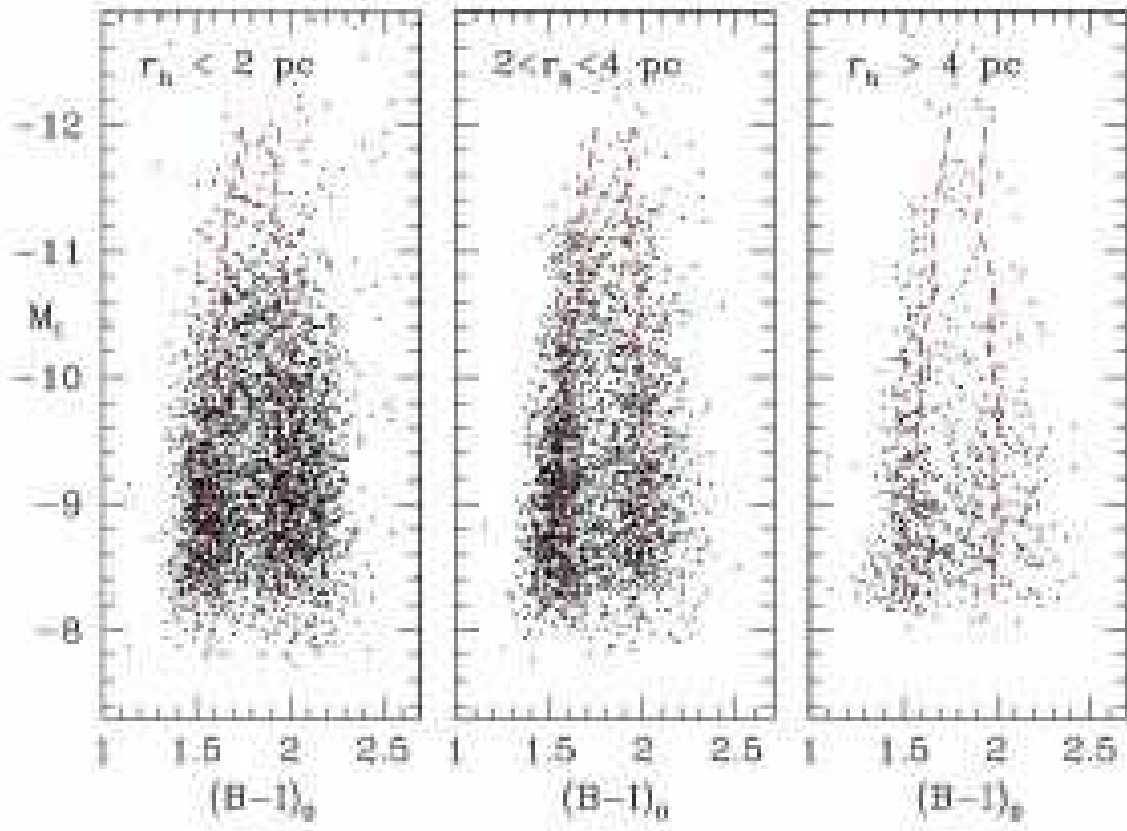


FIG. 30.— *Left panel:* Color-magnitude distribution for the GCs with  $S/N > 20$  and measured half-light radii smaller than 2 pc. *Middle panel:* The same data for objects between 2 and 4 pc. *Right panel:* The same data for the biggest objects,  $r_h > 4$  pc. In all three panels, the dashed lines show the mean GC sequences derived from the entire data sample (see Fig. 13 and accompanying text).

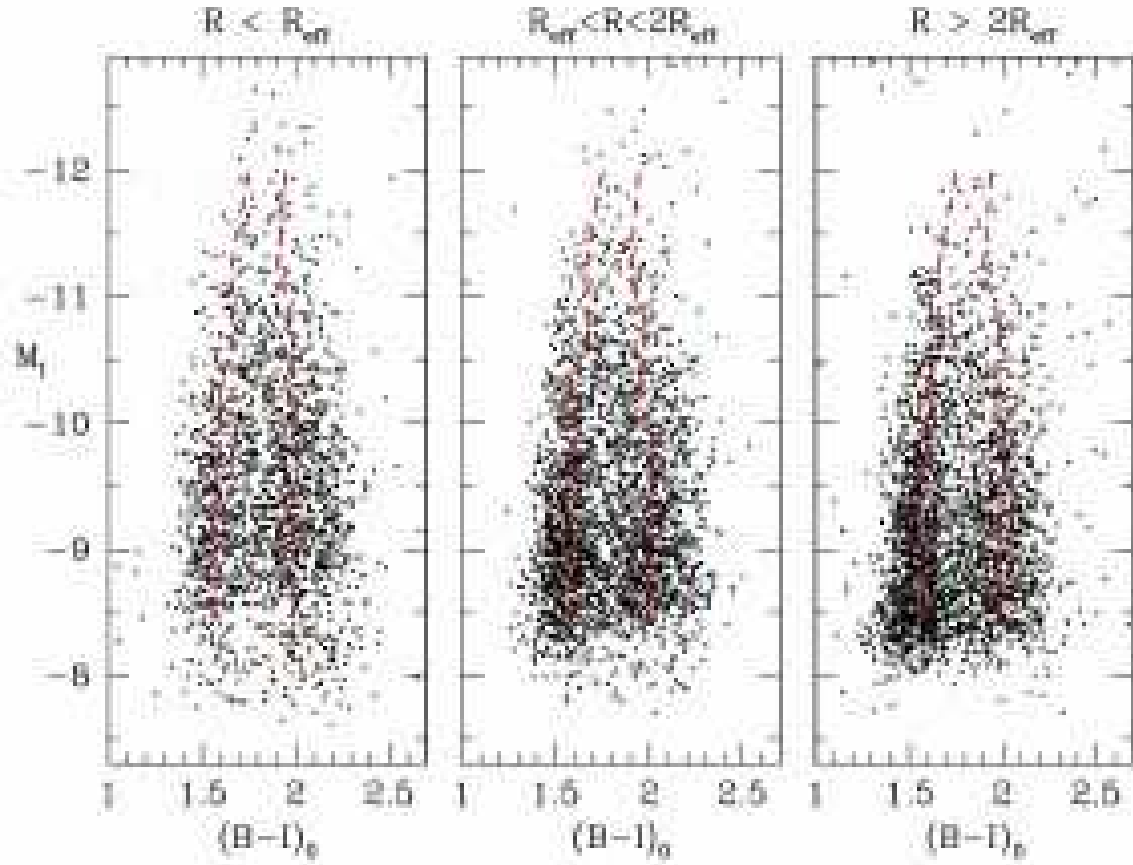


FIG. 31.— Color-magnitude distribution for the globular clusters with  $S/N > 20$  in all six galaxies, subdivided by radial zone. The projected galactocentric distance of each object is expressed in units of the effective radius  $R_{eff}$  of the galaxy's spheroid light. In each panel, the dashed lines show the mean GC sequences derived from the entire data sample. The most remote measured objects are at radii  $\simeq 5R_{eff}$  (see text).

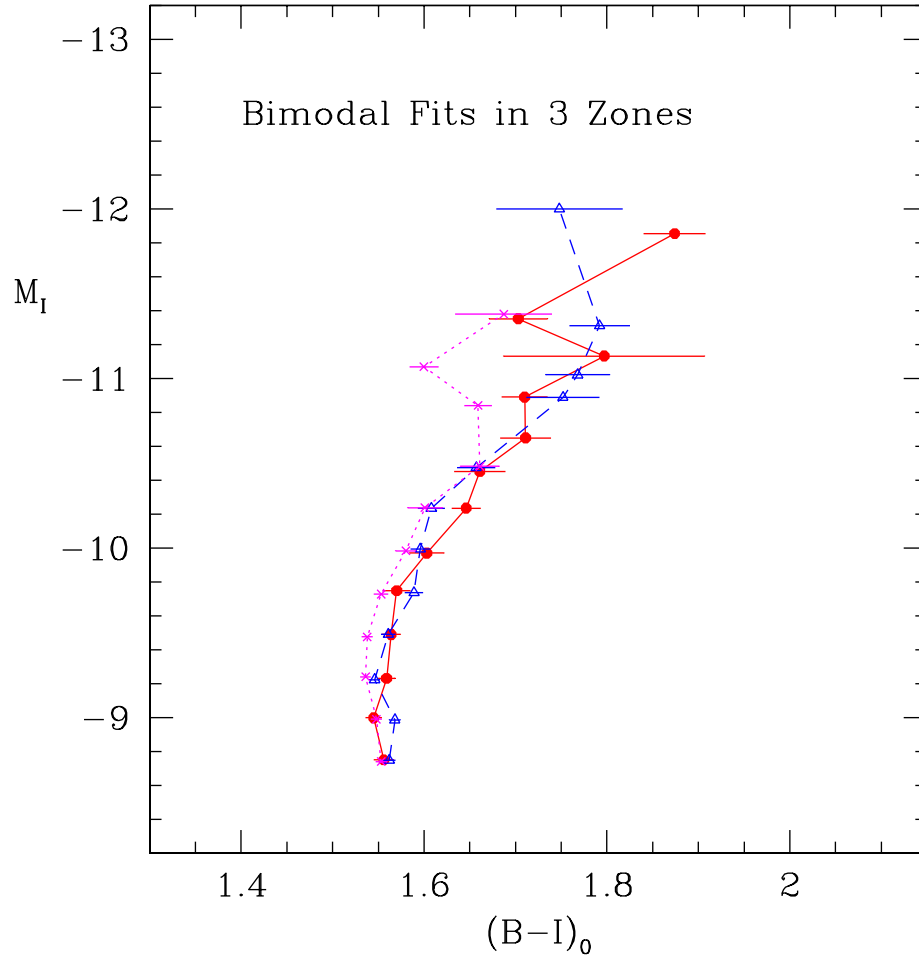


FIG. 32.— Mean points determined from the RMIX bimodal-Gaussian fits for the blue cluster sequence in three radial zones as defined in the previous figure. Solid dots and line are for the inner zone, the triangles and dashed line for the middle zone, and the crosses and dotted line for the outer zone.

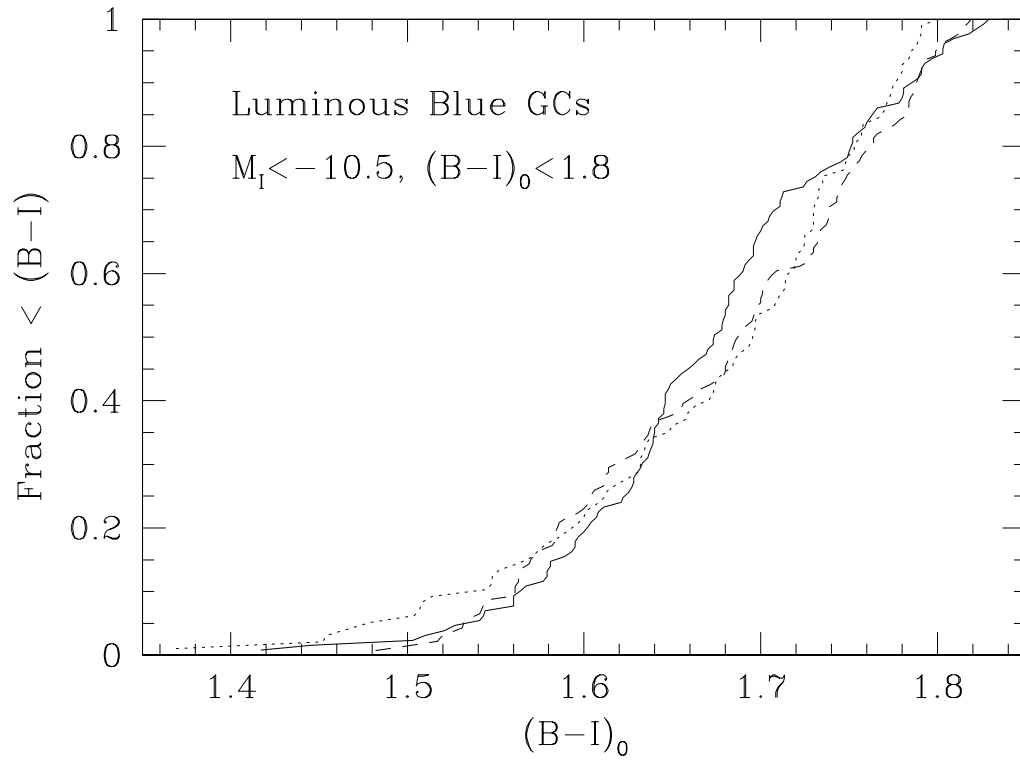


FIG. 33.— Fraction of luminous, blue-sequence globular clusters bluer than  $(B-I)_0 = 1.8$ , plotted against color. *Dotted line* is for the inner-zone clusters ( $R < R_{eff}$ ), *dashed line* is for the mid-zone ( $R_{eff} < R < 2R_{eff}$ ), and *solid line* is for the outer zone ( $R > 2R_{eff}$ ).



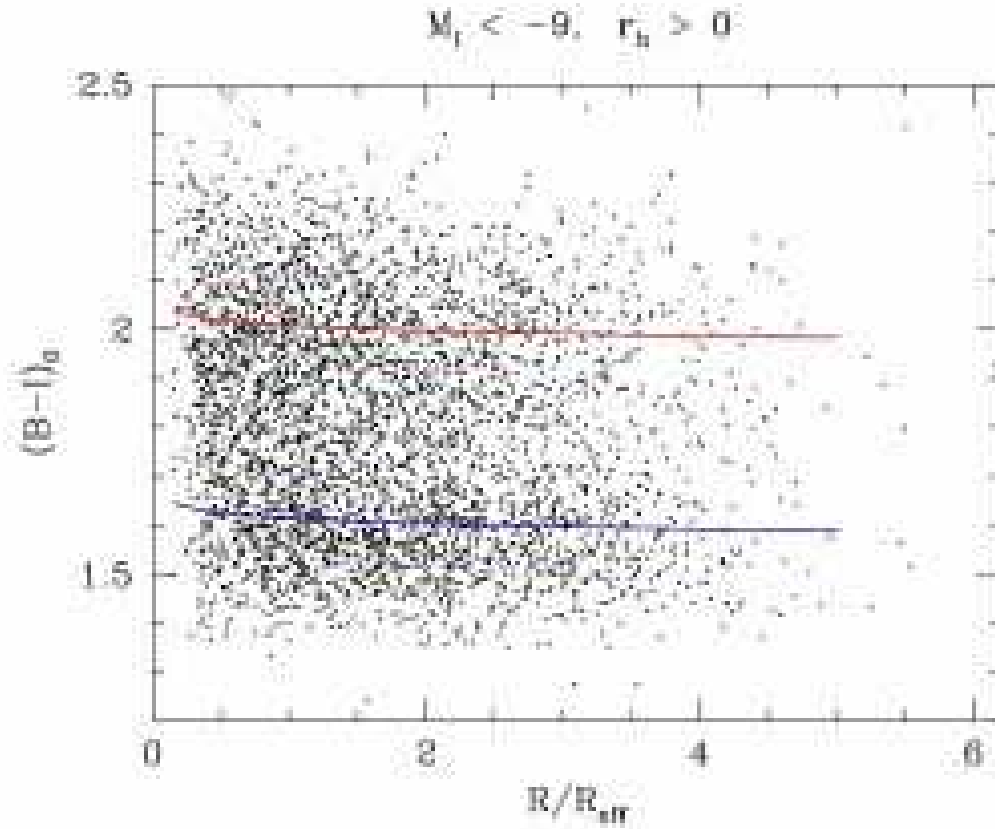


FIG. 34.— Colors of the bright ( $M_I < -9$ ) objects with positive size measurements ( $r_h > 0$ ), plotted against galactocentric distance. Data from all six galaxies are combined. The individual distances  $R$  are normalized to the effective radius  $R_{\text{eff}}$  of the spheroid light. The solid lines show the best-fit power-law solutions for the metallicity gradients, as listed in the last line of Table 7.